CONTROLLING AND CHARACTERIZING MOLECULAR ORDERING OF NONCOVALENTLY FUNCTIONALIZED GRAPHENE VIA PM-IRRAS: TOWARD TEMPLATED CRYSTALLIZATION OF COMPLEX ORGANIC MOLECULES

A Dissertation

Submitted to the Faculty

of

Purdue University

by

Shane R. Russell

In Partial Fulfillment of the

Requirements for the Degree

of

Doctor of Philosophy

December 2018

Purdue University

West Lafayette, Indiana

THE PURDUE UNIVERSITY GRADUATE SCHOOL
STATEMENT OF DISSERTATION APPROVAL

Dr. Shelley Claridge, Chair

Department of Chemistry

Dr. Peter Kissinger

Department of Chemistry

Dr. Jean Chmielewski

Department of Chemistry

Dr. Alexander Wei

Department of Chemistry

Approved by:

Dr. Christine Hrycyna

Head of the School Graduate Program

TABLE OF CONTENTS

Page

LIST OF FIGURES

Figure Page

Figure Page

ABSTRACT

Russell, Shane R. Ph.D., Purdue University, December 2018. Controlling and Characterizing Molecular Ordering of Noncovalently Functionalized Graphene via PM-IRRAS: Toward Templated Crystallization of Complex Organic Molecules. Major Professor: Shelley A. Claridge.

The fabrication and functionalization of layered materials is a key feature in the development of high performance, next generation devices [1–11]. Device applications, such as nanoscale electronics, biosensing, energy conversion, drug delivery and study of proteopathic diseases require interfacial structures that express chemically orthogonal patterns at sub-10-nm scales. For instance, in many semiconducting polymer materials for organic photovoltaics (OPVs), the exciton diffusion length is approximately 5-10 nm [12], meaning that poor pattern resolution between n-type and p-type semiconductors in a bulk heterojunction can substantially reduce charge transfer. Conversely, n-type and p-type domains assembled with a high resolution, sub-10-nm periodicity would produce relatively greater charge transfer. Therefore, the ability to generate alternating patterns at the sub-10-nm scale with high fidelity is crucial in optimizing device performance, and scalability requires that the process be low-cost, highly reproducible and easily screened.

Many techniques have been developed to generate high resolution patterns at the nanoscale. Photolithography [13–15] is a commonly employed process for fabricating conductive/nonconductive semiconductor patterns at the nanoscale, but experiences poor cost effectiveness for sub-10-nm nodes. Soft lithography [16, 17], such as microcontact printing with PDMS stamps, and mechanical lithography, such as dip-pen nanolithography] [18], are more cost effective than photolithography at small scales,

and can apply high fidelity patterns at the sub-μm scale, but often must compromise between high resolution patterns and scalability. Bottom-up assembly strategies, such as block copolymers [19, 20], have been employed as highly modifiable building blocks for generating chemically distinct regions, though often lack the spatial control and pattern resolution required for next generation devices. In other studies, self-assembled monolayers (SAMs) of alkanethiols on Au(111) have been employed as a facile, low-cost way to control interfacial assembly of diverse structures including mineral crystals as well as soft matter at the sub μm scale [21, 22]. However, expressing sub-10-nm pattern resolution of chemical functionality at the fidelity and scale required for next generation nanoelectronic and OPV devices remains challenging.

Graphene has been studied extensively as a 2D material template for device fabrication [2, 3, 8, 9, 23]. This is primarily due to graphene's technologically attractive properties, such as its high surface area, tensile strength [24], exceptional electronic conductivity [25] and biocompatibility [26]. Graphene can also be readily functionalized both covalently and noncovalently to dramatically modulate its physical and chemical properties [1–3, 6]. Modified graphene has been explored as a drug delivery platform for aromatic anti-tumor agents [27], highly selective sensors [28] and as a model platform for interfacial self-assembly of peptide nanostructures [6, 29–31]. The noncovalent modifications to graphene are especially useful, as they preserve most of the intrinsic properties of the interface, while providing a route towards spatial modulation of surface chemistry [1].

Monolayers of diynoic fatty acids, such as 10-12 pentacosadiynoic acid (PCDA), self-assemble noncovalently in a head-to-head lying-down phase on graphene, stabilized both by the epitaxial match between the alkyl zig-zag and the hexagonal graphene lattice, as well the formation of hydrogen bonded dimers between adjacent rows of head groups [7, 32–34]. In this manner, stripes of polar head groups are arranged in a lamellar pattern with a 6 nm pitch. The diyne moiety can be polymerized in these ordered monolayers to form an ene-yne polymer backbone [32, 33], providing a means to stabilize the interface towards solvothermal processing steps [35].

In a similar manner, diyne phospholipids can be used to template surfaces with ordered patterns [7,36]. The phospholipid bilayer of the cell membrane coordinates a wide array of noncovalent self-assembly as well as charge transfer phenomena. Lying-down phases of phospholipids, essentially a repeating cross section of the lipid bilayer [7, 33, 34], therefore produce sub-10 nm chemical patterns with potential for directing further self-assembly in a biomimetic fashion. Modifications to properties such as head group size and charge, as well as tail length and diyne position can generate high fidelity striped interfaces with various pitches, stability and chemical functionality. In fact, recent work has shown that the nanoscale wettability of these lying-down monolayers, a critical property for bottom up device fabrication, can be substantially modulated by structure of the constituent lipid [36,37]. However, scalable device fabrication utilizing high resolution templates of noncovalent monolayers requires a screening process to determine if the initial templates are suitably well ordered for further processing steps. Furthermore, many steps may include solvothermal conditions, which can disrupt the order of the monolayer. A means to screen monolayer order in a manner that is fast, inexpensive, and non-destructive is therefore highly desirable.

Scanning probe microscopy techniques such as atomic force microscopy (AFM) are routinely employed to assess the interfacial order of lying-down phase lipid monolayers. AFM allows for resolution of domain edges at scales up to 50 μm under ideal conditions on atomically flat substrates such as highly oriented pyrolytic graphite (HOPG), and can resolve lamellar structure of domains at scales of $\sim$1 μm [7,36]. However, more technologically relevant surfaces, such as chemical vapor deposited (CVD) graphene on nickel are often much topographically rougher, limiting the resolving power of AFM at micron and nanometer scales.

Scanning electron microscopy (SEM) can resolve domains of lying-down monolayers up to the millimeter scale [38]. Disordered monolayer domains are characterized by their amorphous appearance, and lamellar structure of ordered monolayers can be inferred out to 50 μm by the appearance of lamellar cracks, due to structural shifts

from polymerization induced by the electron beam. Additionally, SEM can characterize rougher substrates with greater ease than AFM, though is more destructive towards adsorbed noncovalent monolayers. Further, both AFM and SEM provide no information on bond molecular orientation, a critical property for inferring template functionality.

Polarization modulated infrared reflection absorption spectroscopy (PM-IRRAS), is routinely employed to detect both covalent and noncovalent changes in monolayer structure at interfaces [39–41]. By rapidly alternating the polarization of IR light between s- and p-planes relative to the substrate, PM-IRRAS characterizes the orientation and order of sub-monolayer amounts of material, while being insensitive to isotropically adsorbing bulk and gas phase species [42, 43]. PM-IRRAS is also relatively inexpensive, requires no sample preparation, and is fast and non-destructive, making it suitable as a screening technique for the order of noncovalent lipid monolayers at graphitic interfaces.

In this work, I demonstrate the utility of PM-IRRAS as a screening process for alkyl chain ordering of PCDA monolayers self-assembled on CVD graphene on nickel substrates. Due to the selection rules of metallic CVD graphene on nickel [44, 45], the intensity of the C-H stretch response produced by the alkyl methylenes is proportional to the order of the monolayer. This relationship is confirmed by comparing the spectral response of substrates to corresponding SEM images, confirming that greater C-H stretch intensity is correlated with higher monolayer order. Furthermore, the spectral ratio $I(CH_{2a})/I(CH_{3a})$ accurately distinguishes between substrates functionalized with ordered and disordered monolayers of PCDA, irrespective of total coverage. Spectral metrics are also capable of screening monolayers on HOPG. Therefore, PM-IRRAS is a fast, non-destructive method for screening alkyl chain order in noncovalent monolayers of lying down phases on 2D materials, as precursors for further device fabrication steps.

Once a monolayer has been screened for order, the next step is to determine the appropriate conditions for further device fabrication steps. For OPVs, bottom-

up self-assembly strategies that can reduce the required number of processing steps and occur under mild conditions are highly desirable. Both n- and p-type organic semiconductors exploit aromatic structural elements that generate excited states via photoexcitation, followed by charge transfer to produce current [46]. Peptides represent a class of biomolecules with well characterized self-assembly properties that incorporate a variety of chemical motifs in their side chains, including aromatic moieties. Additionally, peptides are intrinsically biocompatible, easy to fabricate and environmentally friendly compared to typical organic semiconductor species. Due to these advantages, a great deal of recent interest has developed in understanding how interfacial processes can be used to regulate the self-assembly of peptides into hierarchical structures [6, 10, 11, 47–49]. Numerous experimental and theoretical studies have examined the interplay between peptide-peptide, peptide-solvent, and peptide-substrate interactions in regulating the interfacial self-assembly process [6]. This includes approaches ranging from combinatorial phage display libraries for optimizing peptide binding to graphene [50, 51], as well as increasingly accurate *ab initio* and semi-empirical *in silico* methodologies for predicting and monitoring peptide-substrate interactions [52–54].

Diphenylalanine (FF), the aromatic dipeptide core of the Aβ1-42 amyloid polypeptide, rapidly self-assembles into complex, robust structures under mild aqueous conditions [55, 56]. Modifications to the termini and side chains of FF produce variations in the final structures, such as nanospheres, nanorods and hydrogels [56–58]. Further, self-assembled structures of FF and similar peptides demonstrate semiconducting properties [59–61] that have been exploited for applications including power generation [62] and biosensing [63]. Co-incubation of FF and FFF has been shown to modulate the electronic properties of the resulting nanostructures, demonstrating the potential for regulating the band gap, a critical property for OPV device efficiency [64]. However, for aromatic peptides to be effectively exploited for OPV applications, their self-assembly must be templated such that not only do they express

domains at the 10 nm scale, but also in a way that directs their aromatic ineractions for tuning the band gap.

Here, I present a strategy towards templating epitaxially aligned nanostructures of fluorenyl-9-methoxycarbonyl-diphenylalanine (Fmoc-FF) on noncovalently functionalized HOPG. Peptide structures are often coordinated by noncovalent interactions with the cell membrane [65, 66]. Therefore, monolayers composed of lipid molecules are candidates for directing the interfacial self-assembly of peptides with similar effectiveness as the cell membrane. HOPG passivated with monolayers of PCDA and 1,2-bis(10,12-tricosadiynoyl)-sn-glycero-3-phosphoethanolamine (diyne PE) templates the nucleation and growth of Fmoc-FF nanostructures. The nucleation and growth of Fmoc-FF is consistent with the displacement of the lipid monolayers by the peptides, with widths commensurate with the removal of integer units of lipids. Additionally, monolayer head group chemistry, order and stability are all shown to modulate the self-assembly of the tapes, highlighting the utility of noncovalent strategies for spatially regulated bottom-up synthesis of organic semiconductors for potential OPV applications.

1. SPECTROSCOPIC METRICS FOR ALKYL CHAIN ORDERING IN LYING-DOWN NONCOVALENT MONOLAYERS OF DIYNOIC ACIDS ON GRAPHENE

A version of this chapter was previously published in *Chemistry of Materials*.
DOI: 10.1021/acs.chemmater.7b04434

1.1 Introduction

As 2D materials are integrated into hybrid architectures [1–9,67], controlling their surface chemistry at large scales and throughout solution and thermal processing becomes increasingly important [7, 36, 68, 69]. Layered materials such as graphene are frequently functionalized noncovalently (e.g., with lying-down phases of long-chain alkanes or polycyclic aromatic molecules) to preserve electronic conjugation within the basal plane [1, 2, 70, 71]. However, relatively weak noncovalent interactions within the monolayer [1, 2, 6] increase the probability of molecular disorder, during either assembly or subsequent processing. Noncovalent monolayers have been imaged down to sub-nanometer scales using scanning probe microscopy [32, 33, 72–75]; however, heterogeneity is also common at micrometer and larger scales, necessitating appropriate characterization methods. Spectroscopic metrics have been developed to assess large-scale ordering in standing phase monolayers (e.g., alkanethiols on coinage metals) [42, 76, 77]. Equivalent metrics for 2D materials noncovalently functionalized with lying-down phases would have potentially broad utility, but must account for differences in molecular orientation and in some cases substrate selection rules. Here, we develop spectroscopic metrics for ordering in noncovalent monolayers of diynoic

acids on graphene and graphite, using polarization-modulated IR reflection adsorption spectroscopy (PM-IRRAS) correlated with scanning electron microscopy (SEM).

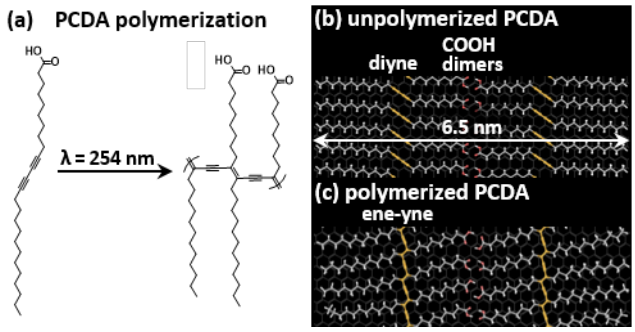

Figure 1.1.: (a) Chemical structure of unpolymerized (left) and polymerized (right) PCDA. Molecular models of (b) unpolymerized PCDA and (c) polymerized PCDA on HOPG, illustrating lamellar width, H-bonded COOH dimers along lamellar median, and polymerization of diyne to form eneyne.

Diynoic amphiphiles, including long-chain carboxylic acids (e.g., 10,12-pentacosadiynoic acid, PCDA, Figure 1.1a), are prevalent in noncovalent functionalization of graphene [72, 78, 79], highly ordered pyrolytic graphite (HOPG) [2, 32, 33, 80, 81], and other 2D materials [82]. Lying-down lamellar phases assemble due to epitaxy between the zigzag carbon skeleton of the alkyl chain and the <1120> axis of the basal plane [32, 83, 84], ordering domains at ∼120° angles [2, 85]. Molecules orient head-to-head, forming carboxylic acid dimers that stabilize the lamellar median (Figure 1.1b). Topochemical photopolymerization of aligned diynes produces an ene-yne polymer backbone (Figure 1.1a,c), which has been examined for molecular electronics applications [72, 85]. Polymerization also increases monolayer robustness toward solvent exchanges or other processing [7].

The degree of alkyl chain ordering governs many chemical properties of the assembled interface. For example, topochemical polymerization efficiency for diynes varies strongly with the distance between bond-forming carbons [33, 82], in addition to details of chain structure and packing [86–89]. We have also found that long-range ordering of diyne monolayers impacts interfacial stability after polymerization in the context of solution processing [35], and that structure-specific headgroup dynamics

(a form of controlled disordering) modulate interfacial wettability [37]. Conversely, monolayer defects can promote undesirable interfacial processes such as nonspecific adsorption and charge carrier trapping [78, 90–92]. Thus, evaluating molecular ordering is central in screening for interfaces that will exhibit desired physical properties in subsequent use.

In principle, atomic force microscopy (AFM) can be used to characterize surface structure at lateral scales up to 100 μm. However, our experience suggests the upper limit for useful AFM topographic imaging of noncovalent lying-down monolayers of diynoic acids on HOPG is 10 μm; beyond this scale, contributions from the substrate itself typically dominate contrast [7, 36]. Characterization of monolayers on more technologically interesting 2D materials such as chemical vapor deposited (CVD) graphene is further complicated by increased surface roughness (e.g., wrinkling) and the topography of the underlying support. Together, these factors make high resolution AFM imaging of PCDA monolayers on CVD graphene at scales significantly >1 μm challenging.

We have recently observed that SEM mitigates these issues, enabling noncovalent monolayer structure on HOPG to be characterized at scales as large as millimeters and as small as tens of nanometers [38]. In the present work, we find that domain structures can be imaged on rougher CVD graphene, at scales up to 30-50 μm, enabling correlation of interfacial structure with functionalization conditions and spectral features. We have also observed previously that the SEM electron beam induces cracking in ordered, but not disordered, PCDA domains, due to conformational changes that occur when rows of ordered molecules polymerize under the electron beam. Polymerization induced cracking can thus be used to distinguish between ordered and disordered areas in molecular films (discussed in more detail below), with implications for film quality in electronic or other applications. Repeated imaging of the same area shows that, during high-resolution SEM imaging, the electron beam also degrades the monolayers, impeding subsequent use of areas of the surface screened in this way.

Addressing this issue, we also develop a nondestructive spectroscopic probe for alkyl chain ordering in noncovalently adsorbed lying-down monolayers on graphene and HOPG. Correlating PM-IRRAS data with subsequently acquired SEM images of the same samples enables us to establish the relationship between spectral characteristics and surface structure. Surface selection rules for metallic substrates emphasize dipole components oriented in the plane of incidence (the plane defined by the surface normal and the incoming beam path) [44, 45]; this provides a basis for analyzing the average degree of alkyl chain ordering in monolayers of PCDA on CVD graphene on nickel substrates. Applicable to broad classes of functional molecules used in noncovalent modification of 2D materials, this approach enables nondestructive screening of interfacial ordering at scales relevant for many applications.

1.2 Results and Discussion

1.2.1 Monolayer Preparation by Langmuir-Schaefer Conversion

To create surfaces with varying degrees of order, PCDA monolayers on graphene were prepared by Langmuir- Schaefer (LS) conversion of standing phase Langmuir films on an aqueous subphase (Figure 1.2a). Although this approach levies additional requirements on sample preparation in comparison with the more expedient drop-casting approach, we find that LS transfer improves uniformity across the entire 1 cm 1 cm substrate (Figure A.2).

Moving barriers compress the Langmuir film to a desired mean area available per molecule (mma). Changes in surface pressure during compression (Figure 1.2b,c) reveal phase transitions in the Langmuir film with increasing order, which impact molecular transfer to the graphene or HOPG. Controlling the temperature of the subphase (T_{sp}) also provides a means of modulating ordering of the Langmuir film (Figure 1.2b vs Figure 1.2c). Here, performing transfers at 20 and 30 °C facilitated comparisons with SEM data we have collected previously for transfers to HOPG under similar conditions (see Appendix A).

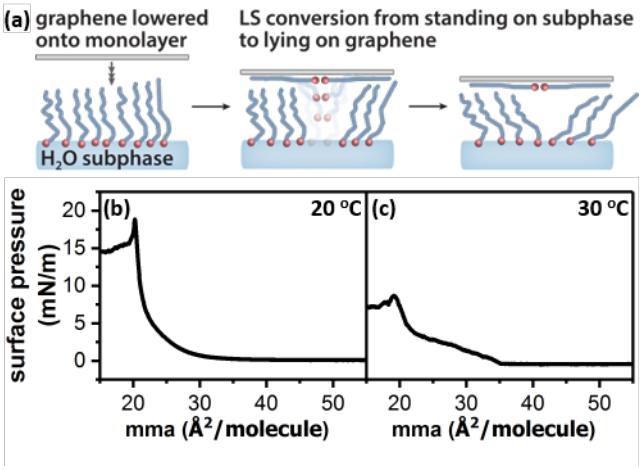

Figure 1.2.: (a) Schematic of LS conversion of PCDA to form lying-down phase monolayers on CVD graphene or HOPG. (b, c) Surface pressure isotherms for PCDA with subphase temperatures (T_{sp}'s) of (b) 20 and (c) 30 °C.

1.2.2 AFM and SEM Evaluation of Monolayer Ordering

AFM imaging is frequently used to evaluate ordering and domain structure in lying-down monolayers. AFM images of ordered regions of unpolymerized monolayers on HOPG and CVD graphene prepared at $T_{sp} = 30$ °C and mma = 30 Å^2/molecule are shown in Figure 1.3. For comparison, similar images from samples prepared by drop-casting are included in Appendix A. Larger flat terraces in an HOPG substrate (Figure 1.3a) contribute to clearer molecular rows than in monolayers on CVD graphene (Figure 1.3b). In both cases, however, lamellar domains with edge lengths >100 nm are visible, assembled in epitaxy with the graphitic basal plane with domains oriented at 120° angles. Already at sub-μm scales, heterogeneities in the graphene surface reduce scanning probe image quality in comparison with HOPG.

In order to examine monolayer structure over larger areas to make useful comparisons with spectroscopic data, we utilized SEM (Figures 1.4 and 1.5). Figure 1.4 compares SEM images of ordered PCDA monolayers on CVD graphene (Figure 1.4a,b) and HOPG (Figure 1.4c,d). In each pair of images, the inset is the original image, and the larger image is the highlighted region, cropped and enlarged to show

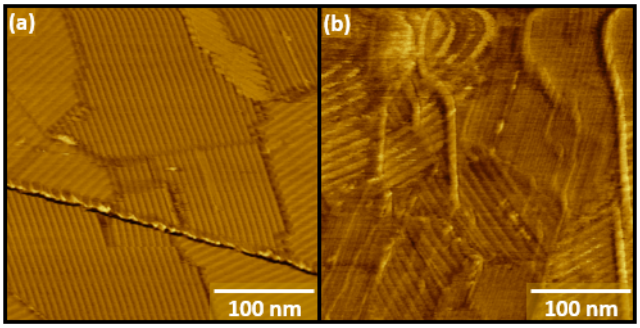

Figure 1.3.: AFM images of PCDA assembled on (a) HOPG and (b) CVD graphene.

detail. Monolayers exhibit cracking defects characteristic of Angstrom-scale decreases in lamellar width as the diyne rehybridizes to form the ene-yne. This behavior is consistent with previous results indicating that ordered regions of such monolayers can be polymerized by electrons in an SEM [38] or STM [93]. AFM imaging of domains of this type next to vacancies on the substrate indicate topographic protrusions of ∼0.5 nm, consistent with lying-down monolayers (see the Supporting Information).

In contrast, disordered molecular domains transferred from Langmuir films at larger mma values (Figure 1.5) exhibit fewer geometric edges, and instead of cracks evolve rounded vacancies under the electron beam; ordered and disordered domains may coexist, as shown in Figure 1.5d. SEM imaging is also possible for monolayers of nondiyne molecules (Figure A.12), though evaluating order is more challenging, suggesting broader applications of this approach.

1.2.3 Evaluation of Monolayer Ordering via PM-IRRAS

PM-IRRAS can detect differences in monolayer ordering that impact alignment of alkyl C-H stretch dipoles [76]. Figure 1.6 illustrates the relationship between molecular ordering and PM-IRRAS signal strength in the C-H stretching region. For previous studies of 2D and 3D crystals of long-chain alkanes, the CH_2 asymmetric stretch (Figure 1.6a right inset, (CH_{2a}) ∼2925 cm^{-1}) and the orthogonal CH_2 symmetric stretch ((CH_{2s}) ∼2850 cm^{-1}) have been used to assess alkyl chain orientation and

ordering. [76, 94, 95] At the bottom of each panel in Figure 1.6a,b, CH_{2a} dipoles are highlighted in red in a side view. In a highly ordered PCDA monolayer, the dipoles are aligned predominantly parallel to the plane of incidence (defined by the surface normal and the beam path, 70° relative to the surface normal for the experiments presented here).

The vector diagram in Figure 1.6a illustrates the distribution of CH_{2a} dipoles for the well-ordered model; vectors deviate from the surface normal by 4° ± 4°. Conversely, dipoles in disordered monolayers have a low degree of alignment in the plane of incidence. For the disordered model shown in Figure 1.6b, vectors deviate from the surface normal by 42° ± 29°. PM-IRRAS peak intensities can be approximated as proportional to the cosine squared of the average dipole angle relative to the p-polarized component of the IR beam. For a beam with an angle of incidence of 70° (i.e., p-polarized component 20° relative to surface normal), this suggests an approximately 2 fold difference in peak intensities for the highly ordered and disordered cases shown in the models. Overall, greater integrated C_{2a} peak intensities, $I(CH_{2a})$, should be correlated with local alkyl chain order. Figure 1.6c,d shows representative spectra acquired from monolayers under conditions that lead to high and low degrees of molecular ordering, similar to the SEM images in Figures 1.4 and 1.5.

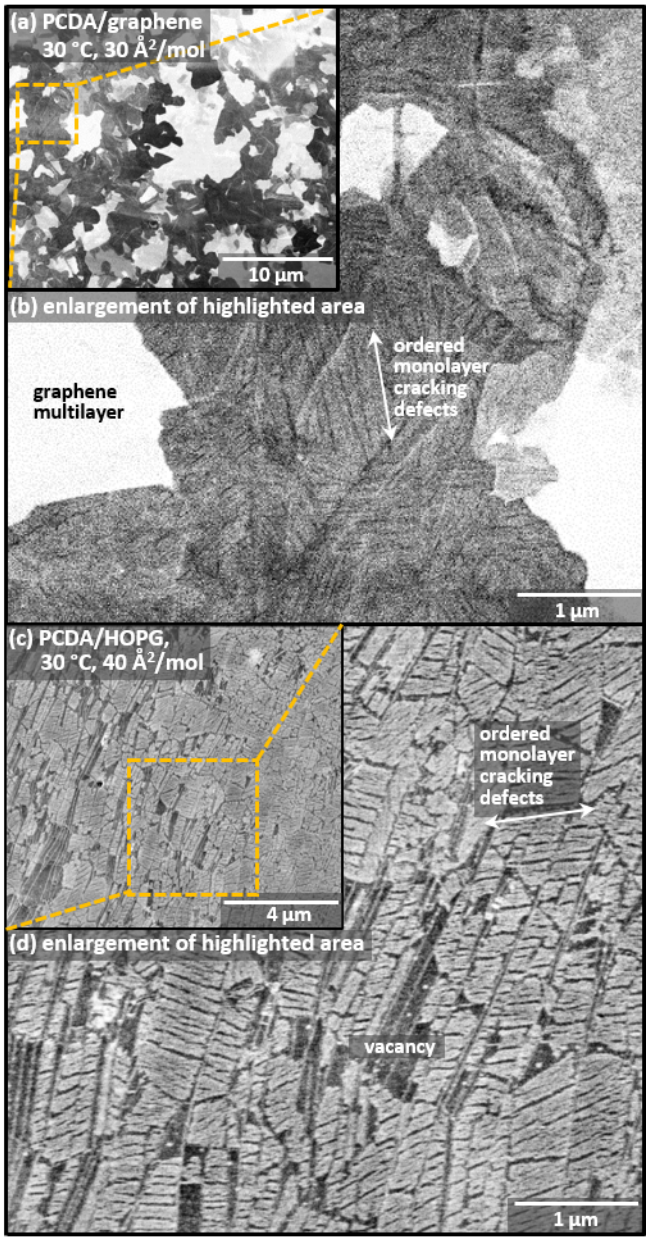

Figure 1.4.: (a) SEM image of ordered PCDA on CVD graphene. (b) Enlargement of highlighted region of part a showing detail in original image with 30 μm edge length. (c) SEM image of PCDA on HOPG, showing ordered regions of lying-down monolayers. (d) Enlargement of highlighted region of part c.

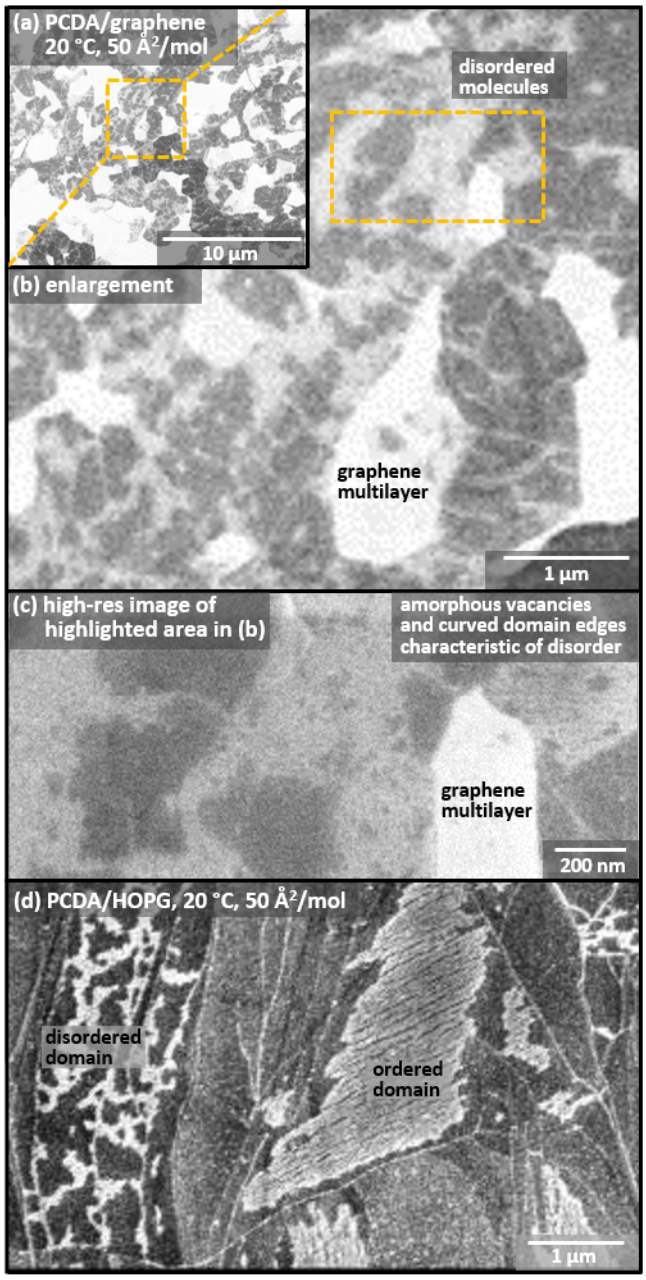

Figure 1.5.: (a) SEM image of disordered PCDA on CVD graphene. (b) Enlargement of highlighted region in part a showing detail. (c) Higher resolution image of region labeled disordered molecules in part b. (d) SEM image of PCDA on HOPG, illustrating coexistence of ordered and disordered regions.

Figure 1.7 compares molecular domain structure observed in SEM images (Figure 1.7e-l, Appendix A, Figures A.8 and A.8, for larger-scale original images) with

I(CH_{2a}). Spectral trace colors match dashed lines in the isotherm that indicate the mma at transfer. Domain structure in films transferred to CVD graphene varies with transfer conditions, similar to our previous observations for transfer to HOPG [38].

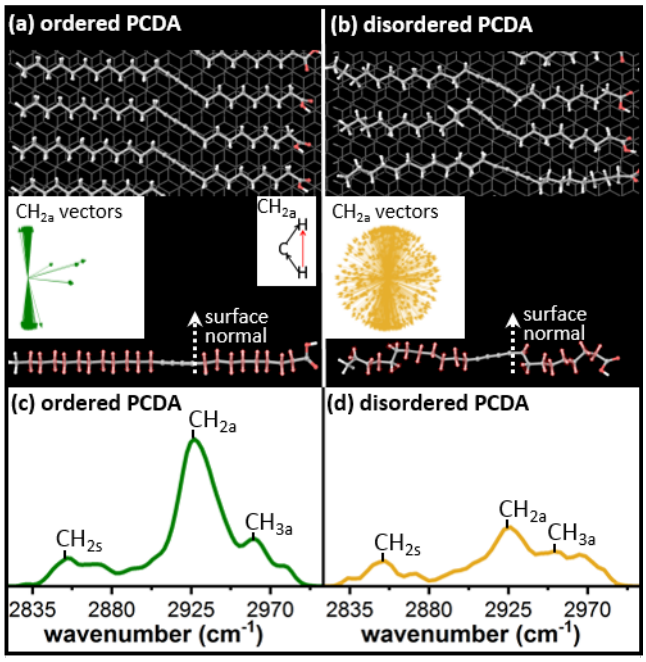

Figure 1.6.: Molecular models for (a) ordered and (b) disordered PCDA (top), and side view of a PCDA monomer with CH_{2a} dipoles highlighted with red arrows (bottom). Insets illustrate CH_{2a} dipole vector distributions. PM-IRRAS spectra for (c) ordered and (d) disordered PCDA.

Interestingly, we find that intermediate values of I(CH_{2a}) correspond to transferred film structures consisting of lying-down lamellar domains (Figure 1.7i,j). Amorphous domains transferred at large mma (40-50 $Å^2$/molecule) exhibit low PM-IRRAS signal intensities (Figure 1.7c,d, orange and red traces). At 20 °C, transferred films remain poorly ordered at mma values as low as 30 $Å^2$/molecule, and I(CH_{2a}) remains low (Figure 1.7c, green trace).

In contrast, at 30 °C, surface pressure begins to increase prior to 30 $Å^2$/molecule; transferred monolayers then exhibit higher coverage and order (Figure 1.7j), producing intermediate values of I(CH_{2a}) (Figure 1.7d, green trace). Ordered domains also transfer from highly compressed Langmuir films (20 $Å^2$/molecule, Figure 1.7e,i).

However, rod-like structures (presumably small 3D crystals of PCDA) appear in SEM images (Figure 1.7e) for T_{sp} = 20 °C. The presence of these structures is correlated with much larger values of $I(CH_{2a})$ (Figure 1.7c, blue trace) and would be undesirable for many applications. Thus, it is not feasible to screen for noncovalent monolayer ordering solely by maximizing $I(CH_{2a})$.

1.2.4 $I(CH_{2a})/I(CH_{3a})$ as a Metric of Monolayer Ordering

Ideally, spectral metrics should distinguish between increases in signal intensity due to increased surface coverage and increased monolayer ordering. The total intensity (I_{total}) of peaks in the C-H stretching region is a convolution of molecular coverage and interfacial order. However, CH_{2a} and CH_{2s} are orthogonal stretches; CH_{2a} aligns strongly in the plane of incidence for ordered monolayers (Figure 1.6a). Thus, for lying-down phases of PCDA, ordering of the zigzag alkyl backbone parallel to the substrate should increase $I(CH_{2a})$ and decrease $I(CH_{2a})$. In contrast, the CH_3 asymmetric stretch ((CH_{3a}) 2960 cm^{-1}) is less sensitive to monolayer ordering [96].

To distinguish between surface coverage and the degree of alkyl chain ordering, we examined ratios of $I(CH_{2a})$, $I(CH_{2s})$, and $I(CH_{3a})$. I_{total} and $I(CH_{2a})/I(CH_{2s})$ (Figure 1.8) have been employed previously to assess coverage and degree of ordering, respectively, of standing phase monolayers and bulk crystals [76, 95]. Both I_{total} (Figure 1.8c,d) and $I(CH_{2a})/I(CH_{2s})$ (Figure 1.8e,f) increase for transfers at smaller mma, consistent with increased coverage of ordered domains (SEM images, Figure 1.7). However, I_{total} and $I(CH_{2a})/I(CH_{2s})$ both vary strongly with coverage of 3D PCDA rods at 20 Å^2/molecule, leading to much larger mean values at 20 °C than 30 °C, even though samples prepared at 30 °C exhibit similar fractions of desirable ordered lamellar coverage. Further, lamellar coverage varies significantly for transfers at T_{sp} = 30 °C and mma >30 Å^2/molecule (discussed in more detail below); this variability is not captured by either metric.

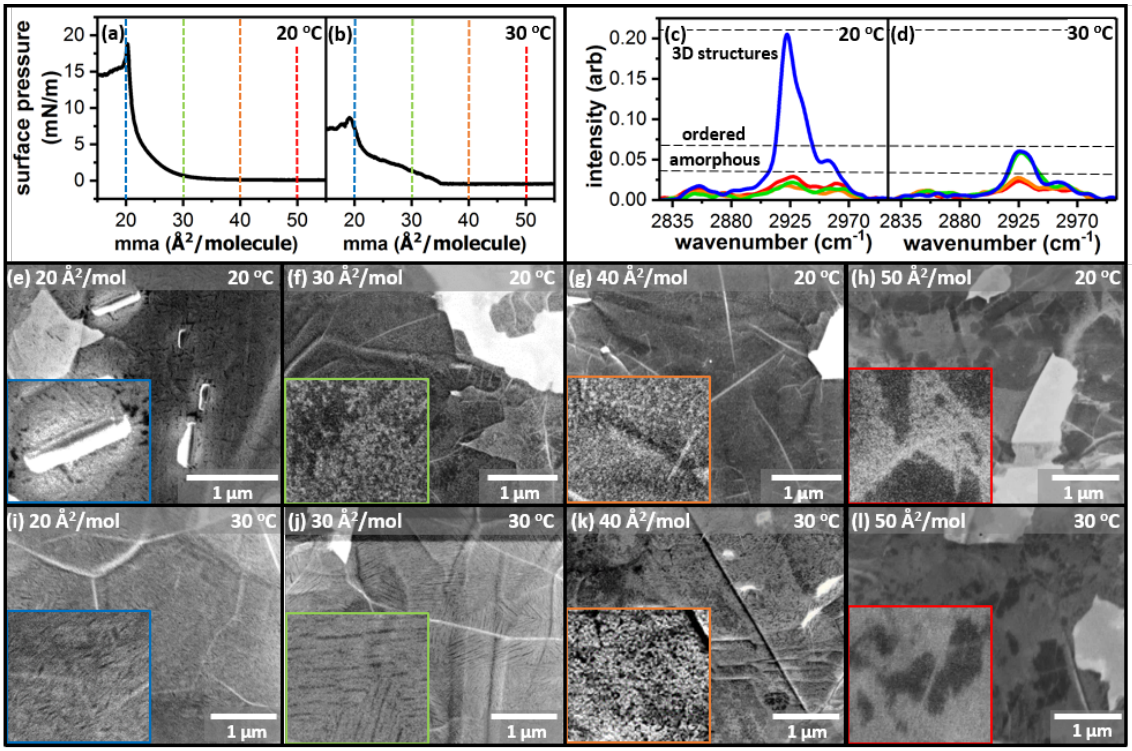

Figure 1.7.: (a, b) Surface pressure isotherms for PCDA with subphase temperatures of (a) 20 and (b) 30 °C; dotted lines indicate mma values at which films were transferred. Representative PM-IRRAS spectra for PCDA transferred to graphene at (c) 20 and (d) 30 °C, showing increased signal intensity for samples transferred at lower values of mma. (e-l) Representative SEM images of samples transferred at the indicated temperature and mma. (See Figures A.8 and A.9 for larger-scale original images.)

Peak frequency shifts are also used to assess ordering in standing phase monolayers of alkanethiols [97]; however, we have not found strong correlations between peak frequencies and degree of ordering observed in SEM and AFM images for the monolayers examined here (A.10). Likely, this is because greater steric freedom afforded to alkyl chains in lying-down monolayers broadens peaks and results in Fermi resonances [95] in the C-H stretching region due to coupling with C-H rocking and wagging motions.

In contrast, transferred films with similar values of $I(CH_{2a})/ I(CH_{3a})$ exhibit similar interfacial structure in SEM images, enabling ordering to be screened independent

from surface coverage. Plots of $I(CH_{2a})/I(CH_{3a})$ vs mma (Figure 1.8g,h) are qualitatively similar to plots of I_{total} (Figure 1.8c,d).

However, $I(CH_{2a})/I(CH_{3a})$ better accounts for the large variation in signal metrics at 40 and 50 Å^2/molecule at 30 °C (due to large variations in ordered surface coverage under these conditions). Additionally, $I(CH_{2a})/I(CH_{3a})$ exhibits a large standard deviation at 25 Å^2/molecule and 20 °C, coinciding with the variable populations of PCDA rods that contribute to signal intensity for transfers under these conditions.

Interpreting $I(CH_{3a})$ as a metric of surface coverage that is approximately independent of monolayer ordering, the ratio $I(CH_{2a})/I(CH_{3a})$ measures the degree of monolayer ordering normalized against surface coverage. Therefore, it would be reasonable to expect substrates with high values of $I(CH_{2a})/ I(CH_{3a})$ to exhibit a high degree of ordering. Figure 1.9a plots $I(CH_{2a})$ vs $I(CH_{3a})$ for a representative distribution of substrates prepared under the range of tested transfer conditions; substrates with values of $I(CH_{2a})$ near the green fit line (high ratio, 3.2 ± 0.1) are characterized by a high degree of order (SEM images in Figure 1.9c-e), with domains exhibiting polymerization-induced cracks visible across large areas of the substrate. In contrast, samples with values of $I(CH_{2a})$ near the gold line (low ratio, 1.6 ± 0.1) exhibit primarily amorphous domains (SEM images in Figure 1.9f-h). The percentage of lamellar surface coverage for PCDA on HOPG was quantified across a range of transfer parameters by SEM and also correlates well with $I(CH_{2a})/I(CH_{3a})$ (Figure A.13). Thus, PM-IRRAS can be used to rapidly and nondestructively screen for order in lying-down monolayers on 2D materials.

Although the CH_{2s} peak intensity could also, in principle, serve as a metric of ordering, in practice, the symmetric stretch intensity does not appear to vary systematically with molecular ordering (Figure 1.9b). As described above, $I(CH_{2a})/I(CH_{3a})$ increases linearly with spectral response per molecule, $I_{total}/I(CH_{3a})$; this relationship is graphed in Figure 1.9b as red and blue circles, with a value of $R^2 = 0.96$ for the linear fit. In contrast, there is not an equivalent increase in $I(CH_{2s})/I(CH_{3a})$ (Figure 1.9b, red and blue diamonds, $R^2 = 0.04$).

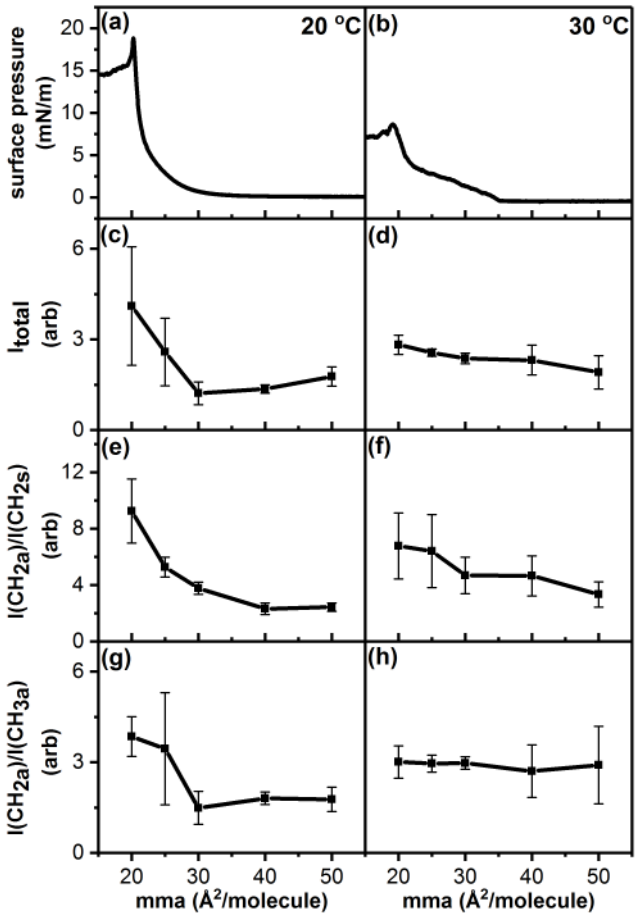

Figure 1.8.: Surface pressure isotherms for PCDA at (a) $T_{sp} = 20$ °C and (b) $T_{sp} = 30$ °C. (c, d) Total intensity (I_{total}), (e, f) $I(CH_{2a})/I(CH_{2s})$, and (g, h) $I(CH_{2a})/I(CH_{3a})$ of the CH stretching region for films transferred at given values of T_{sp} and mma.

1.2.5 Comparison of PCDA Ordering on Graphene and HOPG

PM-IRRAS can also be used to screen noncovalent molecular ordering on HOPG. Raw signal intensities are overall lower for monolayers on HOPG than for those on CVD graphene. However, the selection rules for semimetallic HOPG are similar to those of nickel, with peak asymmetry introduced by dielectric properties [98]. Figure 1.10 shows PM-IRRAS peak ratios (Figure 1.10a,b) and SEM images (Figure 1.10c-f) comparing molecular transfer on HOPG and CVD graphene at 30 and 50 Å^2/molecule with $T_{sp} = 30$ °C. HOPG and CVD graphene exhibit a nearly identical

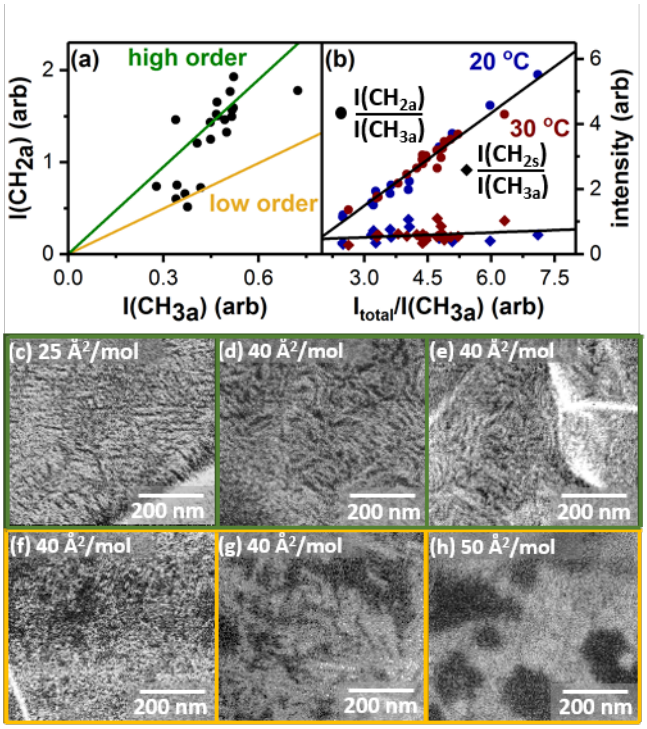

Figure 1.9.: (a) $I(CH_{2a})/I(CH_{3a})$. (b) Peak intensity vs inverse CH_{3a} intensity fraction. Circles represent $I(CH_{2a})/I(CH_{3a})$ while diamonds represent $I(CH_{2s})/I(CH_{3a})$, with $T_{sp} = 20$ °C (blue) and $T_{sp} = 30$ °C (red). (ce, green frames; fh, yellow frames) Representative SEM images from samples with values of $I(CH_{2a})$ near green and yellow fit lines.

ordering/coverage relationship (Figure 1.10a). For both substrates, ordered films transferred at 30 $Å^2$/molecule have high values of $I(CH_{2a})/I(CH_{3a})$ (Figure 1.10b, upper oval; SEM images in Figure 1.10c,d); less ordered films (Figure 1.10e,f; for larger versions of images, see the Supporting Information) transferred at 50 $Å^2$/molecule have low values (Figure 1.10b, lower oval). HOPG substrates typically exhibit higher values of $I(CH_{3a})$, likely due to a combination of the flatter surface resulting in greater extent of transfer during LS conversion and the asymmetric PM-IRRAS peak shapes.

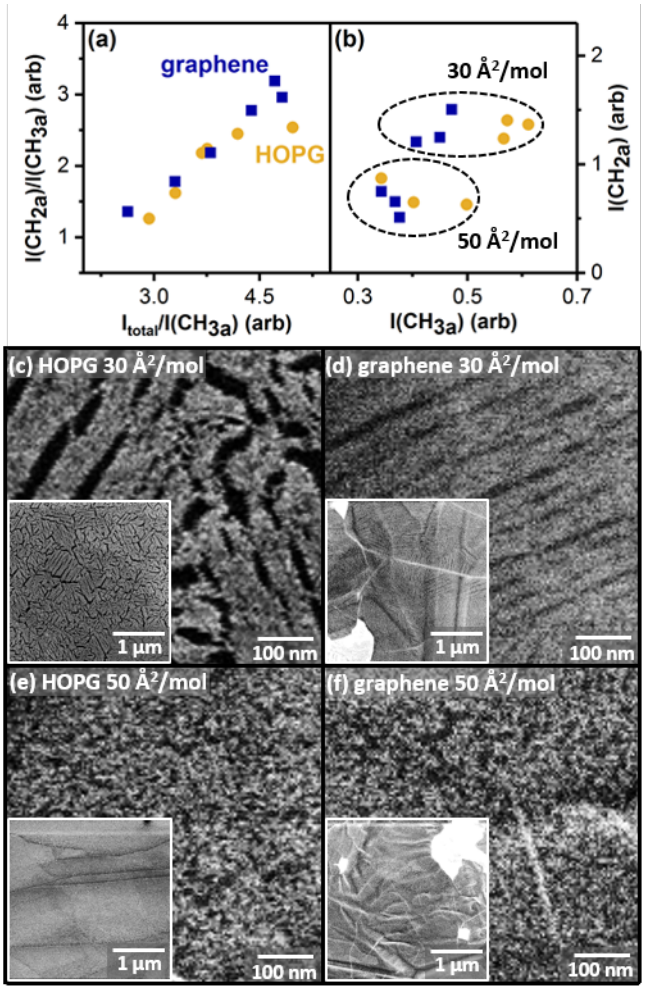

Figure 1.10.: (a) $I(CH_{2a})/I(CH_{3a})$ vs inverse CH3a intensity fraction for HOPG and graphene. (b) $I(CH_{2a})$ vs $I(CH_{3a})$ for the same substrates. (cf) Representative SEM images of samples from part b with insets illustrating overall surface topography.

1.3 Conclusion

We utilized a combination of PM-IRRAS spectra and SEM imaging to assess the degree of ordering in noncovalently adsorbed PCDA monolayers assembled on graphene and HOPG. Monolayers that exhibit a high degree of order in SEM images (e.g., large areas with polymerization-induced cracking) exhibit larger values of $I(CH_{2a})/I(CH_{3a})$ than less ordered monolayers. In contrast, spectral metrics com-

monly used to assess ordering in standing phase monolayers and bulk crystals are less straightforward to correlate with ordering in the lying-down monolayers probed here.

Broadly, PM-IRRAS provides a nondestructive means for examining the degree of local alkyl chain ordering over large areas in 2D materials noncovalently modified with lying-down phases of functional molecules. Other technologically relevant 2D materials exhibit different surface selection rules [99–101] that may ultimately enable more detailed assessment of monolayer structure. Analogous metrics can also be developed for other classes of molecules utilized for noncovalent functionalization of 2D materials by connecting PM-IRRAS spectra with imaging techniques such as SEM and AFM. For applications in which large domain sizes or specific geometries are desirable, SEM also provides a straightforward method to develop relationships between surface preparation conditions and long-range ordering.

1.4 Experimental Methods

1.4.1 Materials

The 10,12-pentacosadiynoic acid ($\geq$97.0% purity) was purchased from Sigma-Aldrich (St. Louis, MO), and used as received. Chloroform (ChromAR grade) was purchased from Macron Fine Chemicals (Center Valley, PA) and used as received. Self-assembled monolayers of diynoic acids were deposited on either 1 cm $\times$ 1 cm CVD graphene on nickel substrates (Graphene Supermarket, Calverton, NY) or highly oriented pyrolytic graphite (HOPG, SPI Supplies, West Chester, PA) substrates; HOPG was freshly cleaved immediately prior to sample deposition. All initial steps in the deposition process were carried out under UV-filtered light to prevent premature polymerization.

1.4.2 Langmuir-Schaefer Conversion

LS conversion was performed using a KSV-NIMA Langmuir-Blodgett trough (Biolin Scientific, Stockholm, Sweden). In a typical transfer, 12 μL of a 0.75 mg/mL solution of PCDA in chloroform was deposited on a subphase of deionized water ($\sim$18 MΩ cm). After the small amount of chloroform used for amphiphile transfer was allowed to evaporate, trough barriers were slowly moved inward to adjust the mean molecular area.

During trough equilibration and compression, the CVD graphene substrates were heated on a hot plate at 300 °C for 10 min to drive off surface contaminants, as the surface cannot be cleaved. The hot plate temperature was subsequently lowered to 120 °C; following removal from the hot plate, substrates underwent additional cooling as they were loaded on the dipper and lowered to the subphase. Typical final substrate temperatures prior to contact with the subphase were $\sim$30 °C. HOPG substrates were subjected to the same treatment for consistency, but were cleaved immediately prior to being loaded on the dipper.

When the Langmuir film was compressed to the desired mean molecular area (e.g., 30 Å^2/molecule), the CVD graphene or HOPG substrate was slowly lowered onto the subphase with the cleaved surface facing down, nearly parallel to the liquid interface. Sample translation was performed using an automated dipper that suspends the sample on a hanging wire, to maximize stability of the substrate-subphase contact. After 4 min in contact with the liquid interface, the substrate was gently lifted out of contact with the liquid using the automated dipper. Samples prepared in this manner were immediately blown dry with N_2 and scanned in the PM-IRRAS. Three substrates were spectroscopically analyzed for each temperature/mma data point, except for values of mma that produced a large variation of monolayer order in transferred films (i.e., at 40 and 50 Å^2/molecule for 30 °C). In these cases, either six or nine substrates were analyzed.

1.4.3 PM-IRRAS

Spectra were acquired using a custom-built PM-IRRAS spectrophotometer. The infrared light source, interferometer, data collection, and processing were provided by a Nicolet iS50R spectrometer (Thermo, Waltham, MA). All optical components were purchased from Thorlabs (Newton, NJ) unless otherwise specified. The infrared beam was passed from the spectrometer exit port into a polycarbonate enclosure and directed through an f/8 BaF_2 lens (Infrared Optical Products, Farmingdale, NY) at a 70° incidence angle using gold mirrors with a protective coating. The beam then passed through a holographic BaF2 linear polarizer set at an angle of 45° relative to the optical axis of a Hinds Series II ZNS50 photoelastic modulator (Hinds Instruments, Portland, OR), which modulated the beam at a 50 kHz frequency and a half wave retardation of 2500 cm^{-1}. The beam was then focused onto the sample and reflected through a second BaF_2 linear polarizer which was adjusted to minimize the polarization effects of the substrate. Finally, the light was focused through a BaF_2 lens onto a HgCdTe high D* detector (Thermo, Waltham, MA). Spectra were acquired at 8 cm^{-1} resolution and 1024 scans (CVD graphene) or 4096 scans (HOPG).

1.4.4 Spectral Analysis

All PM-IRRAS spectra were processed using Origin Pro software. Baseline subtraction was performed using a least squares asymmetric smoothing fit, and peak areas were calculated using the ProFit package to solve for the individual peak areas.

1.4.5 SEM Imaging

All SEM images were acquired using a Nova NanoSEM instrument in immersion imaging mode with a Through-the-Lens detector. Imaging was performed with dwell times of 48 μs under a 5 kV electron beam and working distance of 3 mm, with magnifications ranging from 16 000× to 70 000×

1.4.6 AFM Imaging

All AFM measurements were performed in tapping mode under ambient conditions (in air) using a Bruker (Bruker Instruments, Billerica, MA) MultiMode AFM instrument equipped with an E scanner with 0.01-0.025 Ohm cm antimony (n)-doped Si Bruker RFESP-75 tips (nominal force constant 3 N/m and radius of curvature <12 nm).

1.4.7 Image Analysis

Images were processed using Gwyddion [102] scanning probe microscopy data visualization and analysis software to perform median line corrections, plane flattening, scar artifact removal, and contrast adjustment.

1.4.8 Energy Minimization

Software packages Maestro [103] and Macromodel [104] were used, respectively, to visualize molecular structures and to perform force field minimizations. Models were minimized using the OPLS_2005 force field [105], with normal cutoffs for van der Waals, electrostatic, and hydrogen bonding interactions. PCDA monolayers were assembled by organizing 32 molecules on top of a bilayer of graphene. The PCDA monomers were arranged into 2 columns of 16 molecules each, forming hydrogen-bonded dimers between each pair of molecules. To simulate a randomly disordered monolayer, the PCDA monolayer was subjected to molecular dynamics for 1 ns at 300 °C. All calculations were executed in the presence of explicit water molecules and with the graphene bilayer frozen. Minimizations were performed using the Polak-Ribiere conjugate gradient (PRCG) algorithm and gradient method with 50 000 runs and a convergence threshold of 0.05 kJ/(mol Å). Dynamics were run with 10 ps of pre-equilibration time and a 1.5 fs step time, using SHAKE for bonded hydrogens. The distribution of CH_{2a} dipole stretch vectors was determined by exporting the atom

coordinates and calculating their angles with respect to the graphene surface normal vector.

2. PEPTIDE INTERFACES WITH GRAPHENE: AN EMERGING INTERSECTION OF ANALYTICAL CHEMISTRY, THEORY, AND MATERIALS

A version of this chapter was previously published in *Analytical and Bioanalytical Chemistry*.
DOI: 10.1007/s00216-015-9262-5

2.1 Introduction

Since its discovery in 2004 [23], graphene has been studied extensively because of its exceptional properties [70, 106, 107], including high room temperature conductivity [23], impressive mechanical strength [24], half-integer quantum Hall effect [71], and massless Dirac fermion transport capabilities [108]. Strategic functionalization of the graphene surface can modulate its interactions with analytes, [109] its solubility [110, 111], and its local band gap [4]; functionalization is particularly critical for biological applications, because the hydrophobic graphene surface can otherwise cause proteins to denature [26]. Many applications take advantage of noncovalent modification strategies [112–114] to preserve the high conductivity and intrinsic strength of the graphene sheet [115–124].

Interfaces between graphene and polypeptides or proteins have been of particular interest because of the chemical diversity that can be engineered into the interface, mirroring the diversity of biological structure and function. Even fairly simple interfaces can be useful: graphene and its derivatives have catalyzed hydrolysis of proteins [125], formed nanowire hybrids with polyalanine [126], and acted as templates

for protein and peptide organization via noncovalent binding motifs [26, 127]. Taking advantage of graphenes electron transport properties and susceptibility to molecular doping [128] also permits detection of analyte binding from solution, even at extremely low concentrations [129]. The ability to arbitrarily design peptide- graphene interfaces with molecular precision would open further possibilities ranging from molecular logic devices [130] to biocatalytic reactor surfaces similar to enzymes [131].

However, the structural and chemical diversity of the interface also creates a set of critical analytical and predictive challenges (Figure 2.1). When a peptide adsorbs to graphene, one face interacts with the graphene substrate (important for adsorption stability and/or electronic doping) and one face is exposed to the solvent (important for analyte binding, solubilization, or coupling to create extended materials). Because noncovalent adsorption depends on a delicate balance of molecule-substrate, molecule-molecule, and molecule-solvent interactions [2], a single peptide can have many binding modes. Creation of well-defined interfaces requires the ability to predict peptide adsorption geometries on graphene and to analyze details of peptide binding, including ordering and orientation. The analytical challenges here *also* mirror those in biologythose related to protein folding [132]. Just as with protein folding, assembly involves hydrophilic-hydrophobic interfaces, a vast conformational space, and many local energy minima. At the same time, graphene also makes fundamental changes to the characterization problem, because of its 2D structure, conductivity, and strong optical absorbance.

The ability to achieve both predictive and analytical goals lies near the current limits of theory and experiment. This article first discusses selected examples of bioanalytical applications to provide context for the utility and general structures of peptide-graphene interfaces. Next, we discuss analytical techniques, first those used predominantly to characterize the graphene component of the interface, then we highlight a subset of techniques that provide more detailed information about peptide adsorption and ordering. Recent advances in modeling peptide-graphene interfaces are also examined, with discussion of the trade-offs that are frequently required in

approximating the behavior of the peptide, the solvent, and the substrate. Finally, we provide a brief forward-looking perspective on opportunities for development of experimental and theoretical methods in this area. Although both graphene and graphene oxide have been widely used as substrates for the assembly of peptides, here we largely focus on pristine graphene and graphitic (e.g., highly oriented pyrolytic graphite, HOPG) interfaces, which are more straightforward substrates for detailed characterization and modeling of the molecule-substrate and molecule-molecule interactions that drive assembly. Insights from pristine graphitic materials can ultimately be used to improve understanding of other graphene derivatives.

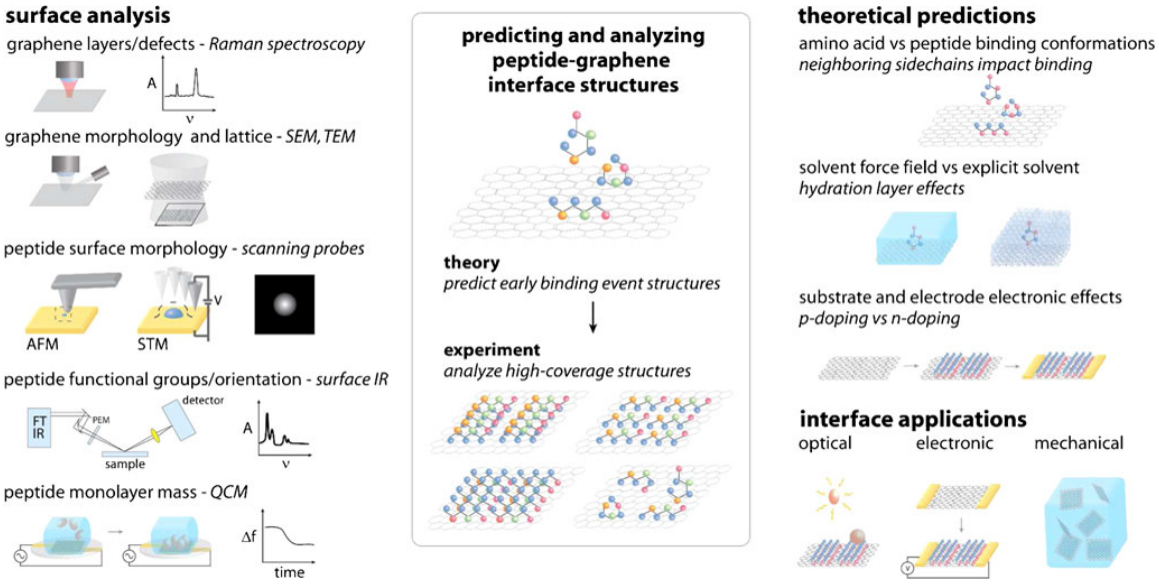

Figure 2.1.: The development, characterization, and utilization of peptide- graphene interfaces represents an emerging frontier for analytical chemistry and theory. (AFM) atomic force microscopy, ($FTIR$) Fourier transform IR, (PEM) photoelastic modulator, (QCM) quartz crystal microgravimetry, (SEM) scanning electron microscopy, (STM) scanning tunneling microscopy, (TEM) transmission electron microscopy

2.2 Context: Applications of Peptide-Graphene Interfaces

Applications of peptide-graphene interfaces may utilize the electronic, optical, and/or mechanical properties of the graphene substrate, which arise from its regular lattice structure. These are combined with the diverse and powerful chemical specificity available from peptides to afford molecular recognition, solubility, spatial ordering, or other properties [113].

For instance, graphene-based sensing applications frequently leverage either conductivity changes produced when an analyte binds to the interface and creates local electronic doping, or fluorescence quenching effects. Early sensors based on nanowires and nanotubes exhibited excellent sensitivity but limited specificity [133]; engineering a peptide monolayer substantially increases the analytical discriminating power of graphene interfaces for sensing. Mannoor et al. designed a wireless bio-interfaced sensor [134], based on bifunctional peptides designed to both bind graphene and specifically detect desired bacterial species (Figure 2.2a). On changes in electronic conductivity (e.g., through a binding event), an electromagnetic signal would be induced and wirelessly transmitted by a gold coil patterned on the graphene. To specifically detect bacteria, a graphene-binding peptide (GBP) was covalently linked via a triglycine sequence to antimicrobial peptide odorranin-HP, which shows specificity toward diseaserelevant bacteria: *Escherichia coli*, *Helicobacter pylori*, and *Staphylococcus aureus* [135]. The device operated successfully in complex mixtures, detecting *S. aureus* content as low as one bacterium per microliter of blood in an intravenous bag, and *H. pylori* binding to a bovine tooth, with a lower detection limit of about 100 cells [136].

Graphenes fluorescence quenching properties can also be utilized in the design of biosensing devices. Frequently such applications use graphene oxide, because of its increased solubility [133]. For example, Zhang et al. designed a protease monitoring device utilizing fluorescence resonance energy transfer with a graphene oxide-peptide interface (Figure 2.2b) [137]. When a fluorescein isothiocyanate (FITC)-labeled

thrombin recognizing peptide (sequence KCALNNGSGdFPRGRAK) was mixed with graphene oxide, the FITC fluorescence was quenched as the fluorophore was brought near the graphene surface. Thrombin, a serine protease important in platelet activation, works by cleaving the Arg-Gly bond, which in this case released the FITC tag, restoring its fluorescence. Here, the sensor was able to detect thrombin activity at peptide concentrations as low as 2 nM.

Thus, both the electronic and the optical properties of biomolecule- graphene interfaces can be used in biochemical assays. However, these applications require specific adsorption configurations to ensure the availability of one segment of the peptide to a solvated binding partner (e.g., thrombin), and simultaneously, the strong binding of another segment to the graphene interface. Similar requirements are levied in other applications, such as the development of hybrid materials, in which the peptide must either passivate or electronically modulate the substrate, while also providing solubility and/or molecular recognition to couple elements of the material [138].

2.3 Analytical Techniques Applied to Peptide-Graphene Interfaces

Continued development of peptide-graphene interfaces [119–121] will benefit from detailed analysis of interface structure. This is analogous to the impact interface-sensitive analytical techniques have had on progress in the field of alkanethiol self-assembled monolayers on coinage metal and other surfaces [139–141]. Surface IR spectroscopy [77], X-ray photoelectron spectroscopy [142], and scanning probes—for example, atomic force microscopy (AFM) and scanning tunneling microscopy (STM) [143–145]—have elucidated molecular tilt angles, binding energies, and lattice structures of such self-assembled monolayers. A detailed understanding of structural aspects of self-assembled monolayers has opened up new applications in the field of nanoscience [101, 139], ranging from bio-inspired mineralization [146] to molecular electronics [147]. The noncovalent monolayer structures formed by peptides on

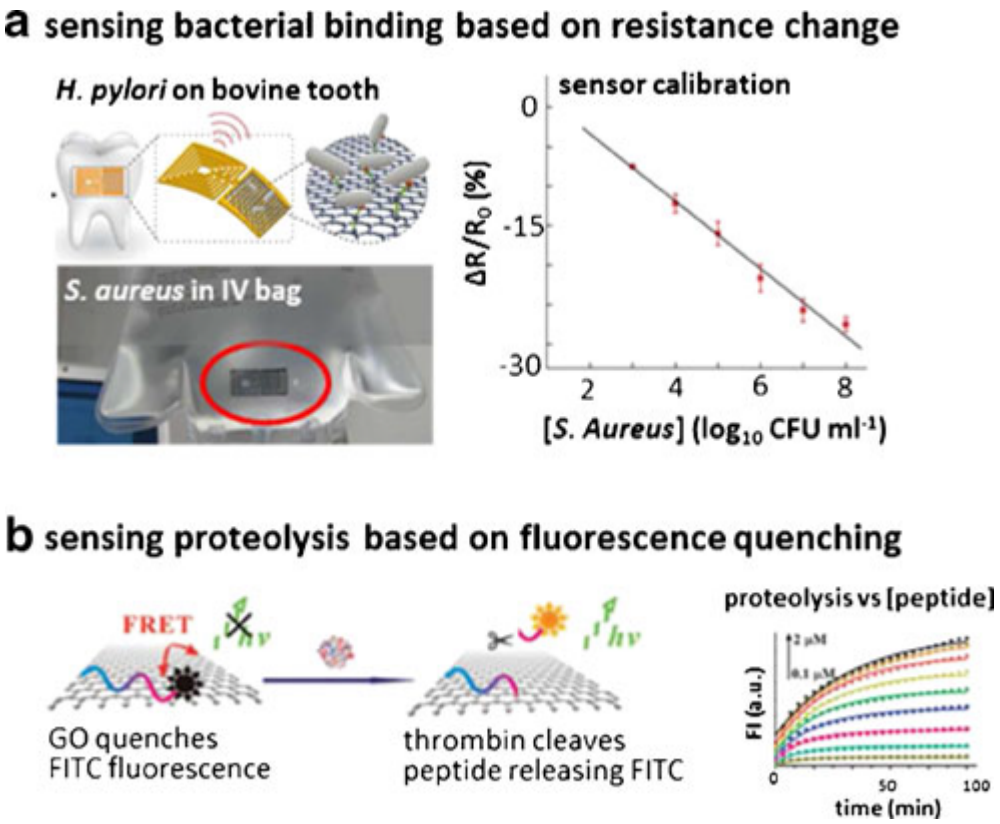

Figure 2.2.: Analytical devices based on biomolecule-graphene interfaces. (a) Functionalized graphene interface conductivity changes in response to bacterial binding. (b) A graphene oxide (GO)-peptide sensor monitors protease activity on the basis of an increase in fluorescence as fluorescein isothiocyanate ($FITC$) is released after peptide cleavage by thrombin. (CFU) colony-forming units, (Fl) fluorescence, ($FRET$) fluorescence resonance energy transfer, (IV) intravenous. (Adapted with permission from [134, 137].)

graphene necessitate certain differences in characterization methods to establish ordering and orientation. For instance, whereas X-ray photoelectron spectroscopy is routinely used to establish Au-S bond formation in alkanethiol monolayers [139] (a starting point for understanding molecular orientation), peptide-graphene interfaces lack this type of spectroscopic signature.

A number of interface-sensitive techniques are useful for the characterization of peptide-graphene assemblies at the material scale (e.g., structure of a graphene sheet or morphology of a peptide aggregate on the sheet). For instance, Raman spec-

troscopy is routinely used to analyze both the number of graphene layers (on the basis of the intensity ratio between the G band peak at approximately 1586 cm^{-1} and the 2D peak at approximately 2695 cm^{-1}) and the presence of graphene defects (on the basis of the intensity of the D band peak at approximately 1350 cm^{-1}) [148]. For instance, in preparing peptide-graphene hybrid materials, Lerner et al. [149] used Raman spectroscopy to evaluate changes in the graphene sheet structure after treatment with diazonium salts and before mixing with peptides (Figure 2.3a). Although the technique is informative in analysis of graphene structure, low Raman scattering cross sections of most organic molecules typically preclude spectroscopy of peptide monolayers. Scanning electron microscopy, with a typical spatial resolution of 5-10 nm [150], is useful in assessing the 3D morphologies of graphene sheets; Figure 2.3b shows the technique used to visualize the rolled geometry of a graphene sheet enveloping a peptide fibril [126]. Transmission electron microscopy (TEM) has spatial resolving power adequate to image sub-nanometer atomic lattices in nanoscopic metals and semiconductors [151] and to observe morphologies of large supramolecular organic structures such as amyloid fibrils interfaced with graphene (Figure 2.3c) [152]. Visualizing organic materials frequently requires staining with contrast agents such as uranyl acetate, since electron scattering is proportional to atomic number. This raises challenges in detecting structure in heterogeneous monolayers of organic material (e.g., peptides), although the more regular structures of graphene and graphene oxide can be resolved with aberration-corrected high-resolution instrumentation. For instance, Figure 2.3d shows high-resolution TEM images of a graphene oxide substrate in which the lattice is visible in parts of the layer. To the right in Figure 2.3d, a model and simulated image show a ferritin protein with a nanocrystalline ferrihydrite core. The core and its lattice structure are visible in the high-resolution TEM image (bottom of Figure 2.3d), whereas the lower-contrast organic protein material is not easily resolved [153]. Continued advances in this instrumentation (e.g., aberration-corrected lenses [151] and graphene liquid cells [154, 155]) may ultimately

make such characterization more feasible for thin, heterogeneous organic structures such as peptide monolayers as well [156].

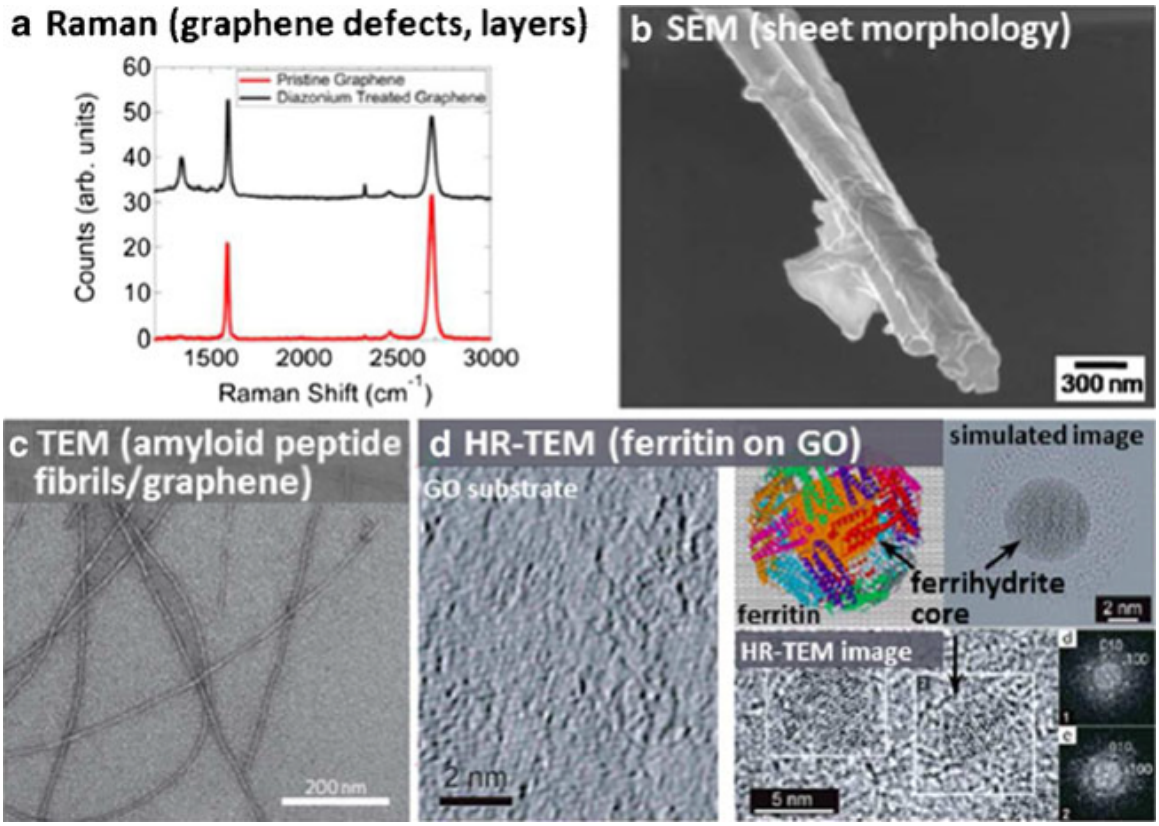

Figure 2.3.: Analytical techniques applied to graphitic interfaces with biomolecules. (a) Raman spectroscopy used to characterize formation of defects in graphene during preparation of peptide-graphene hybrid materials. (b) Scanning electron microscopy (*SEM*) used to characterize graphene sheet morphology following exposure to peptide nanotubes. (c) Transmission electron microscopy (*TEM*) used to visualize peptide fibril morphology on a graphene support. (d) High-resolution (*HR*) TEM used first to visualize local lattice structure in graphene oxide (*GO*) support, and ferritin proteins, including ferrihydrite nanocrystal core. (Adapted with permission from [126,149,152, 153].)

Certain surface analysis techniques, including scanning probes [68], surface IR spectroscopy, and quartz crystal microgravimetry (QCM), have been successfully applied to analyze details of monolayer structure and assembly dynamics in peptide interfaces with layered materials.

Both AFM [51, 157, 158] and STM [159, 160] have proven useful in this regard, because of their extremely high spatial resolution (typically 1 nm lateral and 0.1 nm vertical for AFM; less than 0.1 nm lateral and vertical for STM). For instance, Claridge et al. [160] used a combination of AFM and STM to observe structures of small model amyloid peptides forming β sheets at graphitic interfaces. Figure 4a shows AFM images of peptide lamellar structures with a periodicity of approximately 5 nm formed in epitaxy with the hexagonal graphite lattice. STM images (Figure 2.4b) resolved individual peptides with a lateral spacing of approximately 0.45 nm characteristic of a β sheet, and textural differences corresponding to repeats of histidine and alanine residues. However, the relatively weak noncovalent adsorption mechanism-raises challenges for scanning probes, evident in the ultrahigh vacuum STM image (Figure 2.4c), in which the motion of the probe sweeping across the surface results in streaking as some peptides in the β sheet become dislodged. Although scanning probe techniques cannot typically probe fast interfacial dynamic events, AFM imaging has frequently been used to observe self-assembly dynamics of peptide-graphite interfaces in liquids on timescales of minutes to hours, as in the earlier work of Kowalewski and Holtzman [161]. AFM tips can also be functionalized with a molecule of interest (e.g., a biotin tether) and brought in and out of contact with a functional surface (e.g., streptavidin modified) to measure the strength of a binding interaction [162], suggesting the possibility of the use of peptidemodified AFM tips to measure the strength of interactions with a graphene surface.

The kinetics of early binding events during monolayer formation can be probed by means of QCM [163], which detects mass changes as small as 1 ng associated with analytes (including biomolecules) binding at an interface. The typical monolayer mass for an area the size of a commercial QCM sensor (e.g., circular film 2 mm in diameter) is on the order of 10-100 ng, making it possible to probe monolayer assembly with time resolution of approximately 1 s. Kim et al. [164] used this approach to analyze the amount of a GBP that adsorbed on a set of graphene interfaces on the basis of the number of layers (zero to eight) and the support substrate (SiO_2, TiO_2, or Cu)

(Figure 2.4d). For thicker films of soft materials (e.g., those using antibodies and other large biomolecules, which may have diameters greater than 10 nm), dissipative losses must be accounted for [165], although for nanometer-thick layers such as lying-down monolayers of peptides this is less of an issue.

The chemical environment (and in some cases orientation) of functional groups at a graphene interface can be assessed by use of IR reflection techniques, including attenuated total reflection spectroscopy and IR reflection-absorption spectroscopy (IRRAS) [160, 166]. These techniques can be used to analyze hydrogen bonding and other noncovalent interactions within a monolayer, to monitor the assembly process. Shifts in the amide I band in an IR reflection absorption spectrum provide a readout of peptide secondary structure, with peak positional differences corresponding to α helices, β sheets, and disordered structures (Figure 2.4e) [167]. For detailed characterization of monolayer structure, it is also useful to examine the *orientation* of functional groups relative to the substrate, which can be achieved by use of the subset of polarization modulation approaches such as polarization modulation IRRAS. Because ordered bond dipoles preferentially absorb either s- or p-polarized light depending on their orientation (and surface selection rules), the difference spectrum can be used to assess orientational ordering in nanometer-thick films at interfaces. Although these techniques do not provide spatially resolved chemical information (typical spot sizes may be up to 1 cm^2), they are useful for analyzing monolayers with long-range order to understand which chemical functional groups will be displayed at the solvent and substrate interfaces.

2.4 Theory and Experiment Used in Tandem to Predict Interface Characteristics

Whereas analytical techniques such as AFM, STM, and surface IR spectroscopy typically characterize high-coverage (complete or nearly complete) peptide monolayers on graphene, theoretical simulations shed light on early adsorption events during

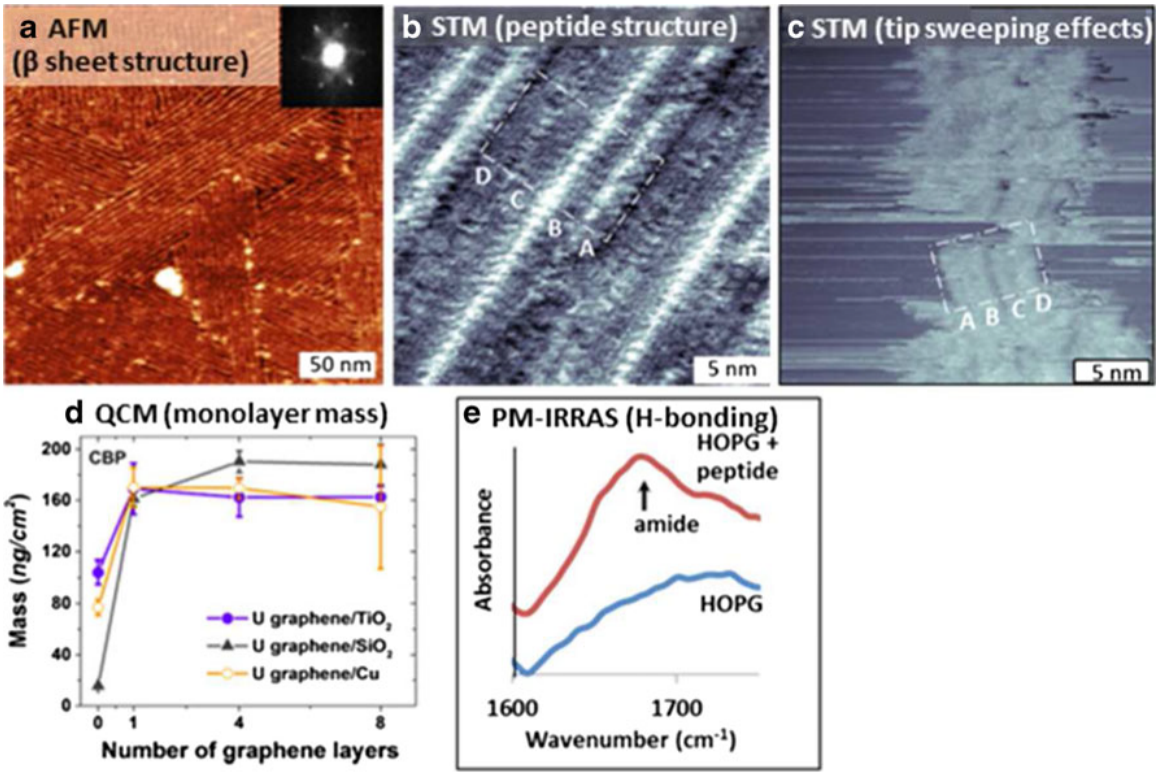

Figure 2.4.: Analytical techniques applied to graphitic interfaces with biomolecules. (a) Atomic force microscopy (*AFM*) resolves peptide β sheets on highly oriented pyrolytic graphite (HOPG). (b) Scanning tunneling microscopy (*STM*) resolves sub-molecular structure in individual peptides (c) Tip dragging effects are problematic for scanning probes in low-coverage monolayers (d) Quartz crystal microgravimetry (*QCM*) resolves sub-nanogram changes in interfacial mass as molecules adsorb during monolayer formation. (e) Polarization modulation IR reflection absorption spectroscopy (PM-IRRAS) detects bond vibration shifts due to hydrogen bonding in peptide monolayers. Carbon nanotube binding peptide (*CBP*) . (Adapted with permission from [160, 164].)

interface assembly. Fast, accurate modeling would streamline predictive design of surfaces to bind arbitrary analytes, or materials with tailored optical or electronic properties. However, because of the complexity of the interface (i.e., large flexible adsorbates, hydrogen-bonding solvent, electronically polarizable substrate), molecular dynamics methods still require various amounts of approximation to reduce computational burden and run time.

Here, we discuss a set of recent theoretical approaches that incorporate different sets of approximations in order to simulate the adsorption of peptides at a solvated graphene interface. For instance, to model the binding of multiple peptides (important in building up a monolayer structure), one approach parameterizes a peptide as a series of residues rather than incorporating the contributions of each atom (which would be more accurate, but also more computationally costly) [168]. Some calculations use explicit water molecules to understand the role water plays in determining which amino acid residues bind most strongly (e.g., due to ordering of water at the hydrophobic interface, or hydrogen bonding to the peptide) [54, 168]. Other calculations use a force field to represent the solvent (less accurate, but also less costly), meaning that the peptide and graphene contributions can then be modeled in more detail. Finally, the electronic polarizability of the graphene substrate almost certainly plays an important role [52, 54]. A number of force fields have been developed to represent graphene with differing levels of accuracy (and expense): AMOEBAPRO is a fairly widely used option that is both accurate and computationally costly; other alternatives such as GRAPPA are more approximate, but also less computationally costly in cases where solvent or adsorbate contributions are of primary importance.

Peptide binding affinities for graphene are important determinants of peptide-graphene interface behavior; calculated values differ depending on how the contributions of the solvent and the substrate are approximated. For instance, Camden et al. [168] used a computationally efficient "four-box" method (Figure 2.5a) to calculate binding enthalpies for peptides binding to graphene [169]; the computational efficiency of the approach allowed the inclusion of explicit water molecules. Surprisingly, in these simulations many residues with hydrophilic side chains exhibited greater binding enthalpies than aromatic residues, because of interactions with the relatively dense first hydration layer at the graphene surface. These calculations were performed with the TEAM force field [170], which parameterizes molecules on the basis of molecular fragments rather than atoms to facilitate model construction. Other computational studies using force fields such as AMOEBAPRO in combina-

tion with implicit solvent predict that aromatic residues such as tryptophan should exhibit the strongest binding because of π-π stacking [171]. This divergence raises important questions regarding the relative importance of the contributions of solvent and substrate in the assembly process, in particular the role of water ordering at the hydrophobic interface.

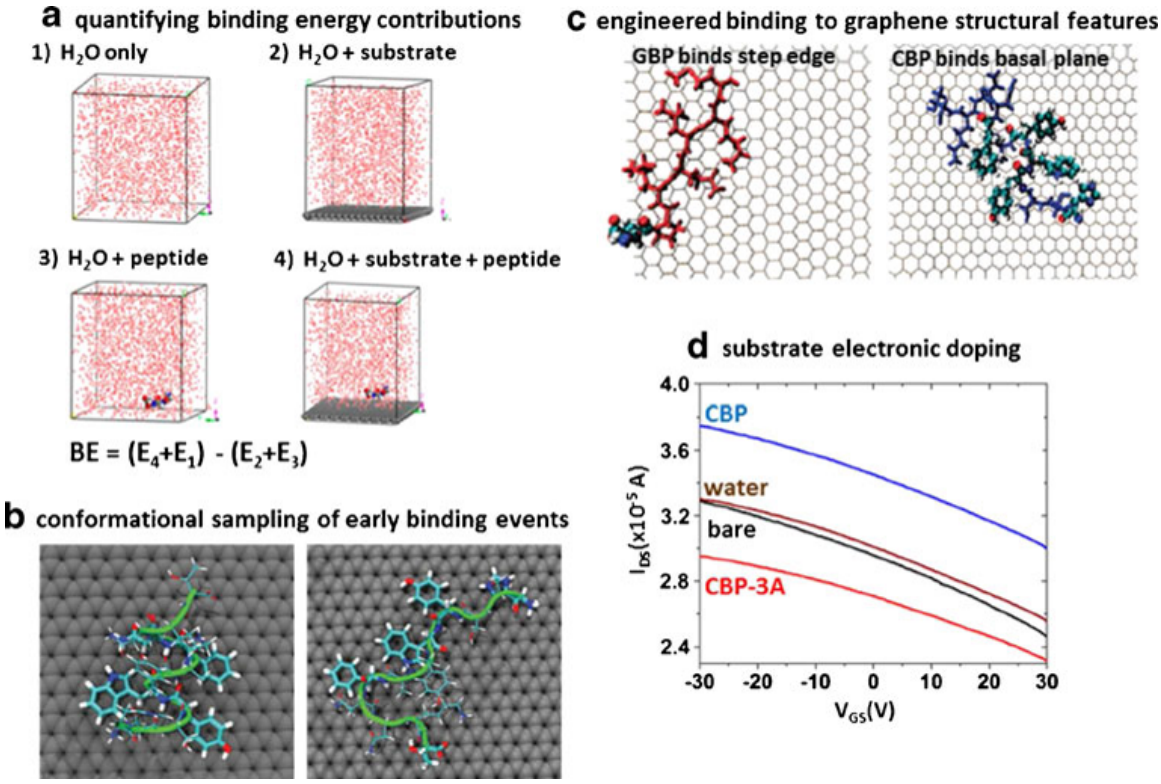

Figure 2.5.: Modeling of early binding events. (a) Four-box model quantifies solvent, substrate, and peptide contributions to binding enthalpy (BE). (b) Replica exchange allows broad conformational sampling to ensure the lowest energy structure is found. (c) Peptides can be engineered to bind either graphene step edges or graphene basal plane. (d) Theory can be used to predict graphene electronic doping by peptides. Graphene binding peptide (GBP). (Adapted with permission from [50, 52, 168, 172].)

The extensive conformational space for complex peptides requires broad sampling to ensure the lowest-energy conformer is found [173]. Parallel tempering (also known as replica exchange) allows multiple conformations to be sampled simultaneously at different temperatures and interchanged to improve the dynamic properties of the

simulation [174]. However, the sheer scale of the conformational space of a peptide means that parallel tempering often requires excessive computational resources. Replica exchange with solute tempering reduces the number of replicas required by varying the temperature of only the solute (as opposed to the solute and solvent) between replicas [175]. Hughes and Walsh [54] used this approach in tandem with the relatively inexpensive GRAPPA force field (which models graphene polarization using a rigid rod dipole, and is less rigorous and expensive than multipole AMOEBAPRO), allowing the use of explicit solvent (Figure 2.5b). Again in this approach, a new possible driving principle for self-assembly of peptides on graphene emerges with the use of explicit solvent molecules. In addition to large, planar side groups (e.g., arginine, tryptophan, and tyrosine) typically used in graphene-binding motifs, small compact groups (e.g., glycine) also displayed high binding affinity; adsorption brings the functional groups out of dense hydration layers approximately 3 and 6 Åfrom the surface. Again, this suggests that a detailed understanding of solvent behavior may be important in the prediction of noncovalent interface structures

In graphene, the sheet edges and basal plane have different chemical characteristics, which can be exploited in the development of peptide-graphene interfaces, making it important to accurately model the substrate. This possibility has been explored both experimentally and theoretically, because it is experimentally straightforward to distinguish between step edge and basal plane adsorption with use of AFM. Experimentally, McAlpine and coworkers [50,51] have leveraged combinatorial phage display libraries to engineer peptides that not only bind specifically to graphitic interfaces but also exhibit preferences for either step edges or the basal plane (Figure 2.5c). For instance, a phage-selected GBP (sequence EPLQLKM) displayed affinity toward HOPG step edges, whereas a previously engineered carbon nanotube binding peptide (CBP) (sequence HSSYWYAFNNKT) bound uniformly across the HOPG surface. Molecular dynamics simulations in explicit water indicated that the GBP is attracted to the slightly positive step edges through its negatively charged glutamate residue. Conversely, the CBP maximizes π-π off-stacking interactions between its aromatic

groups and the graphene surface. In these calculations, approximations were made regarding the peptide: interactions of individual peptides with a graphene sheet were first modeled by all-atom simulations; these results were used to normalize parameters for residue- graphene coarse grain interactions [53, 176] to reduce computational complexity for larger models over longer time frames. Simulations performed with this approach were able to capture the greater basal plane binding potential of CBP versus GBP, as well as the critical importance of the residues YWY in anchoring CBP to the graphene basal plane. Here, the ability to combine experiment with theory helps ensure appropriate levels of approximation are used in the simulation.

In some cases, the goal of creating a non-covalently modified graphene interface is to create local electronic doping (Figure 2.5d) [52,92], making it especially important to accurately model the substrate. Akdim et al. [52] tested peptide doping effects in graphene field effect transistors using both simulations and experiment [50]. The simulations used the AMOEBAPRO force field [177] and implicit solvent. The electron transport properties of the peptide-functionalized graphene were then modeled with use of nonequilibrium Greens functions [178] and density functional tight binding [179], a semi-empirical method that allows calculation of the density of states in an extended system. Interestingly, their calculations indicated that p-doping can arise *either* from π stacking with aromatic side chains *or* from interactions with the peptide backbone near residues with small side chains (e.g., alanine), suggesting the possibility of an alternative class of peptide doping motifs. However, whereas the experimental results demonstrated a large p-doping effect for CBP, a small n-doping effect was observed for the alanine peptide. Such divergence could arise from approximations made in the simulation or experimentally from the presence of graphene defects or electronic effects caused by the introduction of metal electrodes. This highlights the need for both improved experimental techniques to assess detailed interfacial structure directly and improved theoretical methods to treat the presence of features observed in real device architectures.

2.5 Outlook

Interfaces between layered materials and biomolecules, such as the peptide-graphene interface, have the potential to create fundamentally new types of surface chemistry with applications ranging from sensing to nanoscale electronics to hybrid functional materials. However, complex interactions between biomolecules, solvent, and substrate can result in a variety of adsorption conformations, impacting both substrate electronic structure and solvent interface chemistry in ways that are not currently well predicted. Conversely, this means that a rich variety of interface structures (both chemical and electronic) will become available if predictive control can be developed through a coupling of theory and experiment. A few key issues will likely shape development of this area.

The hydrophobic-hydrophilic interface dynamics important in assembly of biomolecules on graphene present key opportunities for contributions from theory. However, noncovalent interactions are difficult to capture accurately in energy minimizations, and understanding early stages of assembly at hydrated graphene interfaces requires quantification of contributions from both ordered water layers in the nanometer nearest the hydrophobic surface and the electronic polarization of the substrate. Therefore, it is likely that the most successful strategies will develop experimental methods to assess common enthalpic and entropic contributions to assembly and use these known values to reduce simulation complexity. Polarized optical measurement methods such as polarization modulation IRRAS and polarized nonlinear optical spectroscopies that have the potential to resolve bond orientations and vibrational energy shifts at an interface are thus especially promising in this regard.

In the comparison of theory with experimental results, another critical challenge is the imperfection of real interfaces. Although graphene and graphene derivatives are now widely available commercially, variations in manufacturing and transfer procedures can result in batch-to-batch variations that become important in the assembly and characterization of peptide-graphene monolayers. Additionally, recent experi-

ments indicate that in the 24 h following synthesis or thermal annealing to produce a clean graphene interface, adsorption of adventitious contaminants from the laboratory atmosphere substantially changes the surface chemistry [180]. Thus, the capability to not only prepare clean interfaces but also to routinely and quickly assess the presence of non-covalently adsorbed contaminants will become key to successful interface development.

Finally, new experimental techniques that simultaneously offer single-molecule spatial resolution and chemical information have the potential to resolve adsorption geometries and interface chemistry directly. For instance, force-curve-based and molecular-recognition-based AFM measurements can resolve certain types of molecular interactions on a substrate, and STM measurements based on microwave-frequency bias modulation and inelastic tunneling can also be used to resolve the presence of key functional groups [68].

A rigorous understanding of design principles for peptide- graphene interfaces can ultimately be expected to open new routes for not only in vitro sensing and electronics but also for establishment of in vivo interfaces with layered materials. Such applications will allow the exceptional mechanical, optical, and electronic properties of layered materials to be intimately mixed with the diverse and powerful chemistry that emerges from noncovalent interactions in biology.

3. TEMPLATED ASSEMBLY OF AROMATIC DIPEPTIDES ON GRAPHITE PASSIVATED BY AMPHIPHILLIC MONOLAYER RESISTS WITH SUB-10-NM CHEMICAL PATTERNS

3.1 Introduction

Interface-mediated nucleation and assembly of soft matter, including peptide nanostructures, is central to issues ranging from human health to nanoscale device fabrication [6,10,11,47–49]. From a medicinal perspective, surface-mediated self-assembly of amyloid peptides (e.g. Aβ1-42 derivatives) has been investigated to provide insights into the progression of proteopathic diseases such as Alzheimers [47, 181–186]. Fibrillation of the Aβ peptides has been monitored on surfaces such as highly oriented pyrolytic graphite (HOPG) and mica [183, 187–189], to characterize interfacial effects on self-assembly, which is thought to play a role in amyloidogenesis. From a materals perspective, control over the density and morphology of self-assembled peptides has been examined at a variety of interfaces [6, 10, 184, 190–192]. For example, Ryan et al. demonstrated the ability to modulate the binding and growth of charged peptides on HOPG by applying a potential difference to the surface [31]. Techniques ranging from physical vapor deposition [193], to electrodeposition [31, 190, 194] and covalent modification with hydrogelators [49, 191] have been employed to regulate the self assembly of peptide structures.

Even very short peptides (e.g. elaborations of the Phe-Phe amyloid core motif) can assemble into chemically and thermally robust structures exhibiting useful morphological variations in response to structural modifications and environmental cues [55–58, 195, 196]. Eckes et al. have utilized modified dipeptides to create hy-

drogels susceptible to nonenzymatic degradation [197]. Work from the groups of Gazit and others has exploited protecting ligands and side chain modifications to the dipeptide core, generating structures ranging from hydrogels to rigid fibers and nanospheres [198–200]. The peptide self-assembly process has found utility in guiding the growth of metal wires and nanocatalysts [57, 201, 202]. Hydrogels have been utilized in device applications ranging from sensing [63,203] to biomimetic growth matrices [204,205]. Additionally, nanostructures generated from peptides expressing aromatic side chains demonstrate potential for electron and proton transfer, highlighting their potential utility as biocompatible, cost-effective organic semiconductors [59–61]. Longer range applications like power generation [62], tissue regeneration [206] and drug delivery [207] have been explored.

Heterogeneous self-assembly of peptide crystals has been studied primarily in the context of modulating surface-peptide interactions [6, 10, 21, 22, 29, 49, 190]. Surface mediated self-assembly of crystal structures has several advantages, including lower activation energy for nucleation, promoting selective growth of otherwise unfavorable crystal orientations and generating spatial control over both the nucleation and growth of crystals [22, 208].

In many applications, it would be advantageous to direct the hierarchical self-assembly of peptide structures using surfaces to template growth at the nm scale. Patterning surfaces with high fidelity, chemically distinct regions at somewhat larger scales can be achieved with soft and mechanical lithography [16, 17], in addition to more established techniques, such as photolithography [13–15]. Generally speaking, there are compromises between scalability (and ease of use) and pattern resolution (e.g. comparing microcontact printing with PDMS stamps and dip-pen nanolithography with an AFM tip). For viable applications in device fabrication, interfacial peptide structures must be templated with high spatial resolution using a facile, scalable process.

Self assembled monolayers (SAMs), such as alkanethiols on Au(111), have been particularly useful in directing heterogeneous peptide crystallization [21, 22], due to

their facile preparation, high degree of order and the wide array of chemical modifications that can be presented at the interface. However, other classes of monolayers present structural features with potential utility in the context of controlling assembly at the interface. Recent work has demonstrated that HOPG and graphene modified with monolayers of amphiphilic lipids (e.g. 10,12-pentacosadiynoic acid, PCDA) produce a template displaying alternating stripes of functional headgroups and extended alkyl chains with sub-10 nm periodicity, analogous to a repeating cross-section of a cell membrane [7, 33, 34]. These high-fidelity chemical patterns modulate the wetting and templating properties of the graphitic basal plane [36, 37], while preserving desirable electronic and physical properties [113, 209]. Peptide structures are often coordinated by noncovalent interactions with the cell membrane [65, 66]. Therefore, monolayers composed of lipid molecules (e.g. 1,2-bis(10,12-tricosadiynoyl)-sn-glycero-3-phosphoethanolamine, diyene PE) are candidates for directing the interfacial self-assembly of peptides with similar effectiveness as the cell membrane.

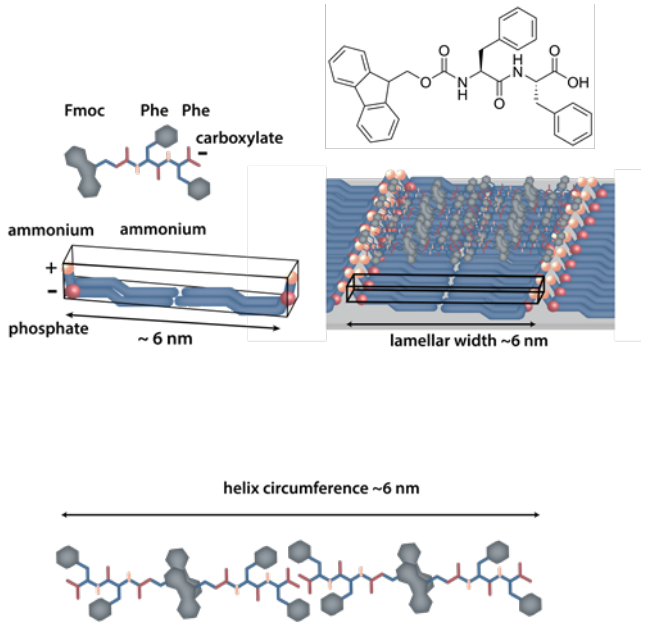

Figure 3.1.: Scheme illustrating concept of Fmoc-FF assembly and lying-down monolayers

In this work we template the growth of fluorenyl-9-methoxycarbonyl-diphenylalanine (Fmoc-FF, Figure 3.1) tapes onto HOPG modified with PCDA and diyne PE. We demonstrate that the passivation of the HOPG basal plane with amphiphiles activates the growth of highly regular Fmoc-FF tapes, whose growth can be modulated by the monolayer head-group chemistry.

3.2 Results and Discussion

3.2.1 Assembly of Fmoc-FF on HOPG, PCDA and diyne PE monolayers

Monolayers of PCDA were prepared via Langmuir-Schaeffer (LS) conversion from an aqueous subphase as previously reported [7]. Briefly, PCDA was deposited from a 0.75 mg/mL chloroform solution onto a subphase of DI H_2O heated to 30 °C. After allowing the chloroform to evaporate, a set of barriers was compressed until the mean area available per molecule was 30 Å^2. At this point, a freshly cleaved HOPG substrate was lowered into contact with the subphase for 4 min, after which it was removed from the subphase and remaining water on the surface was blown off with N_2. Monolayers of diyne PE were prepared in the same manner, except it was transferred at a surface pressure of 16 mN/m with a heated dip head (nominal temperature 60 °C) [35].

In previous work done by others, hydrogels of Fmoc-FF have typically assembled from aqueous solutions with concentrations of 1-2 mg/mL [55, 195, 200]. Under these conditions, dense mats of fibrils form in solution and coat the interface within minutes. Here, to establish the structural relationship between the peptides and the substrate, we examined assembly at lower concentrations (e.g. 12.5 μg/mL), and an incubation time of 60 s (Figure 3.2).

Each Fmoc-FF peptide contains three aromatic ring systems, enabling strong π-π interactions with the HOPG substrate (-117 kJ/mol based on molecular modeling). Experimentally, we do not discern extensive epitaxial assemblies on bare HOPG

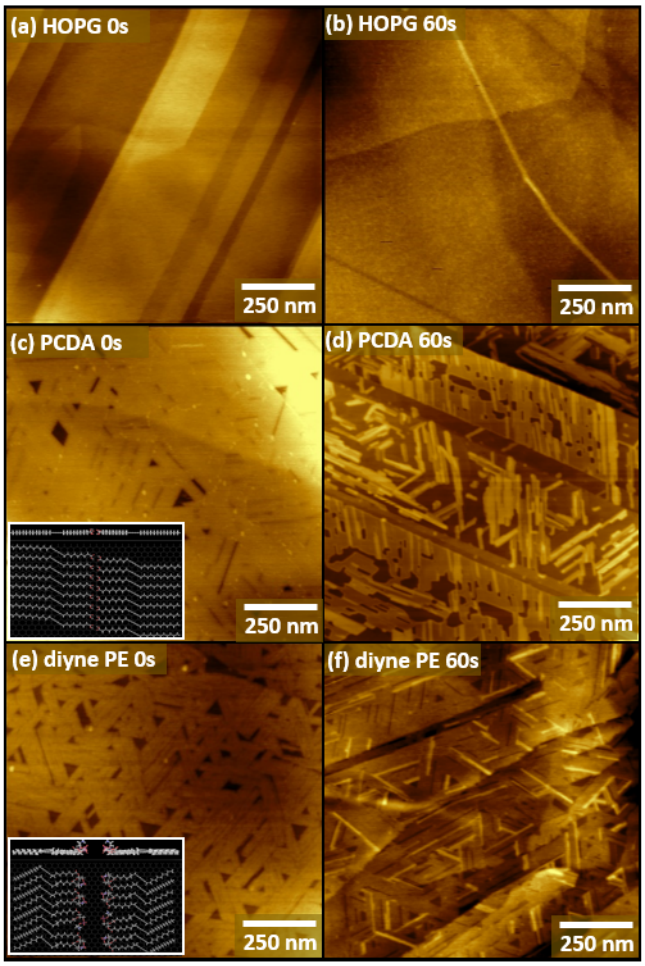

Figure 3.2.: Fmoc-FF incubated on monolayers of (a,b) HOPG, (c,d) PCDA and (e,f) diyne PE with an aqueous concentration of 12.5 μg/mL for (a,c,e) 0 s (i.e. no peptides), and (b,d,f) 60 s. Insets show molecular models of lipid monolayers on passivated HOPG interfaces.

(Figure 3.2b), consistent with strong peptide-substrate interactions limiting peptide-peptide interactions necessary for self-assembly (though localized self-assembly can be observed near step edges). After 60 s in contact with PCDA monolayers, Fmoc-FF assembles into epitaxial tape structures (Figure 3.2d), comprising both partial domain coverage of isolated tapes (apparent widths ~20 nm) as well as complete domain coverage by fused sheets. Oligopeptides designed around the same propensity for aqueous self-assembly have been reported to similarly assemble epitaxially

on HOPG, primarily through aromatic interactions of the side chains with the basal plane, and stabilized through the formation of β-sheets [6, 29, 30]. This suggests that passivation of the HOPG reduces the activation energy of nucleating the peptide tapes by preventing the strong monomer-substrate interactions. Diyne PE monolayers produce slower assembly (Figure 3.2f) with tape widths consistent with those observed on PCDA, although tapes are again strongly epitaxial. This creates the question as to how the monolayer contributes structurally to the Fmoc-FF growth mechanism.

Incubating Fmoc-FF at 12.5 μg/mL for 60 s on disordered monolayers of PCDA (prepared by LS transfer at 75 Å^2/molecule) results in no peptide tape growth (Figure 3.3a). Hence, the lamellar structure of the monolayers play a critical role in nucleating the initial crystals. More specifically, we suspect that it is high surface energy defects in the ordered monolayers that act as nucleation sites for Fmoc-FF tapes, and the lamellar direction of the monolayer that controls the further growth of the tapes. Two potential mechanisms are likely in this case; either the tapes grow on top of the monolayer, or they displace the monolayer and template directly on the graphite.

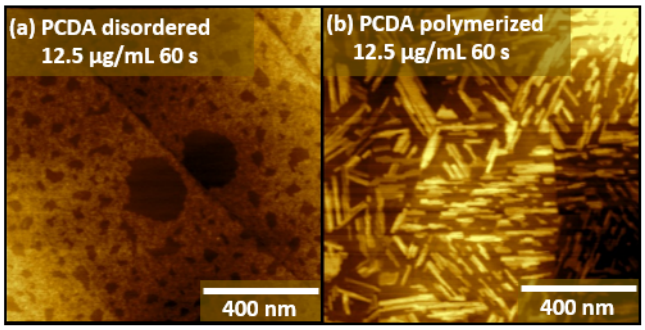

Figure 3.3.: AFM height images comparing Fmoc-FF growth on (a) disordered PCDA and (b) polymerized PCDA incubated for 60 s with 12.5 μg/mL Fmoc-FF.

Polymerizing the PCDA monolayer has the effect of suppressing Fmoc-FF tape growth (Figure 3.3b). Fmoc-FF was incubated on polymerized PCDA (irradiated for 1 hr with 254 nm light) for 60 s, and the growth of the fused sheets was notably reduced compared to the unpolymerized equivalents. Previously, we have observed that polymerization of PCDA monolayers stabilizes them towards removal via sol-

vent washing [35]. In the context of the experiments presented here, this suggests that stabilizing the monolayer towards removal inhibits the nucleation and growth of the peptide tapes, consistent with a displacement mechanism. We note that the same apparent widths of isolated tapes (∼20 nm) is observed for both the polymerized and unpolymerized samples. This points to the structural properties of the monolayer governing the tape width, in a manner similar to a resist used during device fabrication.

3.2.2 Quantification of Fmoc-FF tape growth on passivated HOPG in lower dielectric solvent

Reducing the solvent dielectric reduces the rate of interfacial peptide assembly, allowing observation of earlier stages in the self-assembly process. This is consistent with previous studies showing that the primary factor governing the aqueous self-assembly of FF peptides is the dewetting of the aromatic side chains [197]. Fmoc-FF was incubated at 12.5 μg/mL for 60-180 s on PCDA in either pure water (100% H_2O) or a 1:3 (v:v) MeOH:H_2O solution (75% H_2O) (Figure 3.4). Epitaxial assembly of the peptide tapes is retained in both solvents. In 100% H_2O, partial coverage of isolated tapes and fused sheets at 60 s (Figure 3.4a) progresses to uniform coverage with numerous well defined vacancies at 120 s (Figure 3.4b). At 180 s a second layer of Fmoc-FF tapes is observed (Figure 3.4c). The heights and uniformity of the peptides increase over time from 1.2 ± 0.3 nm (60 s) to 1.5 ± 0.3 nm (180 s) (Figure 3.4d). With the addition of 25% MeOH, assemblies are reduced in height at each time point (Figure 3.4e-g), 0.7 ± 0.2 nm (60 s) and 0.9 ± 0.3 nm (180 s) (Figure 3.4h), consistent with both the slower growth of the tapes, as well as the fact that they likely adopt a less rigid structure in a lower dielectric environment. Based on measured heights, we propose that the tapes assemble in a standing phase, stabilized in one axis by anti-parallel β-sheet hydrogen bonding, and in the other by strong interactions of the aromatic side chains (Figure 3.5).

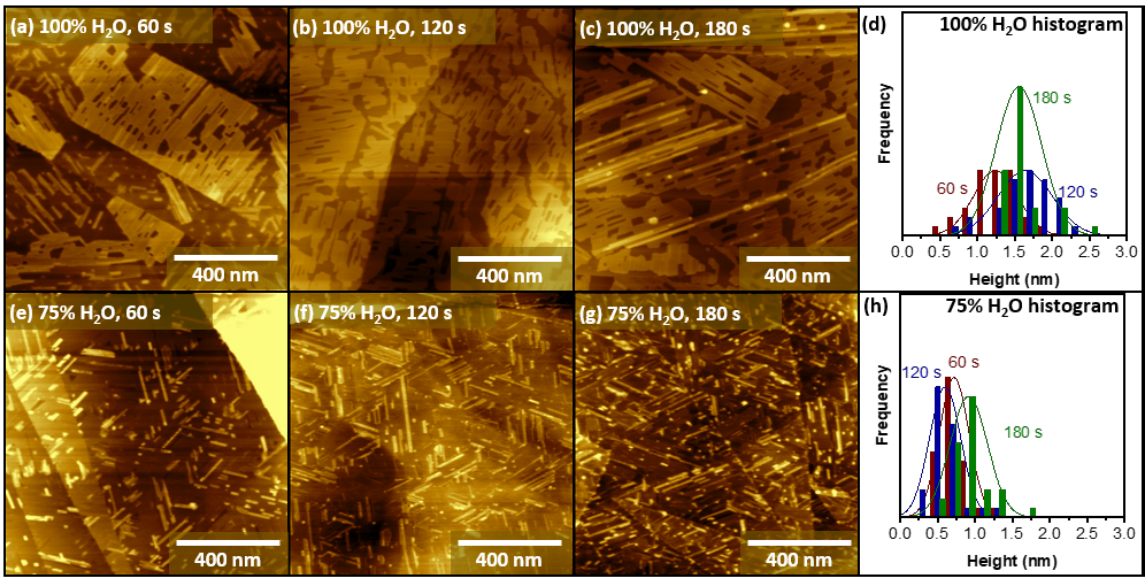

Figure 3.4.: AFM height images of Fmoc-FF (12.5 μg/mL) incubated for 60 s on PCDA in a solution of either (a-c) 100% H_2O or (e-g) 1:3 (v:v) MeOH:H_2O (75% H_2O) for (a,e) 60 s, (b,f) 120 s or (c,g) 180 s. Histograms corresponding to tape heights assembled in (d) 100% H_2O or (h) 75% H_2O.

Lower surface coverages of peptide sheets are observed in the lower dielectric solvent, but the apparent widths of tapes remains similar at ~20 nm. A previous AFM study of peptide tape assemblies on HOPG reported similar apparent widths, and tip deconvolution of these apparent widths produced corrected widths of 3-4 nm, which were attributed to the dimensions of the oligopeptide monomer [6]. Our calculations produce larger corrected widths for the tapes in this study (Figure 3.6a). Interestingly, while the corrected widths are distributed between 10-20 nm, they appear to be grouped into sets corresponding to the dimensions of the monolayer lamellar structure, specifically its 6 nm pitch (equivalent to two PCDA monomers ca. 3 nm in length) (Figure 3.6b). The most common widths in order of frequency are 12.0 ± 0.8 nm, followed by 15 ± 0.8 nm and finally 17.5 ± 0.9 nm, with a much smaller population of widths that are smaller and larger. These common widths would correspond to the removal of 4, 5 and 6 PCDA molecular lengths respectively.

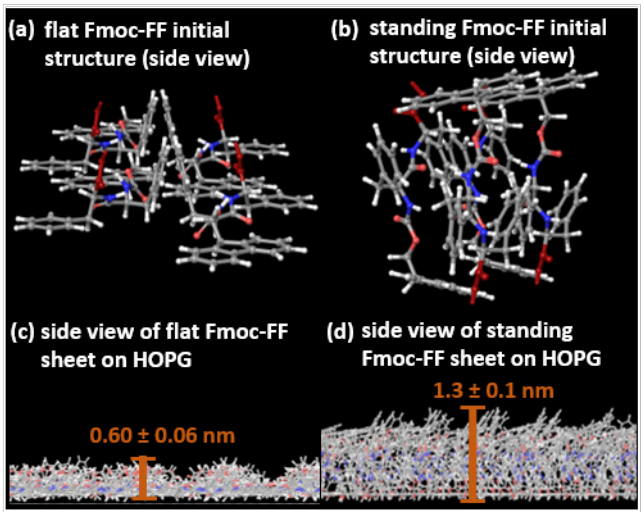

Figure 3.5.: (a) Top view of lying-down Fmoc-FF and (b) side view of standing antiparallel Fmoc-FF structures on HOPG with carboxylic acids highlighted in dark red. Side views of full structure for (c) lying-down and (d) standing Fmoc-FF.

We also observe numerous features 0.2-0.3 nm in height on top of the monolayer (and occasionally the peptide tapes), with lamellar pitches consistent with PCDA (Figure 3.7). We do not observe these features during control experiments in 75% H_2O without peptides, and therefore attribute these to redeposited PCDA displaced by the Fmoc-FF.

Incubations with Fmoc-FF derivatives only produce epitaxial tape structures when the N terminus is protected by an aromatic group. Figure 3.8 shows that only carboxylbenzyl diphenylalanine (Z-FF, Figure 3.8c) and Fmoc-FF (Figure 3.8d) generate peptide tapes, while diphenylalanine (FF, Figure 3.8a) and tert-butylcarboxycarbonyl diphenylalanine (Boc-FF, Figure 3.8b) do not self-assemble at the interface, even at a higher concentration of 25 μg/mL. All four of these dipeptides are known to self-assemble into ordered solution phase structures under similar conditions at concentrations of 1-2 mg/mL [56]. This suggests that the aromatic protecting group plays a key role in the nucleation and growth of these peptides at these ordered lipid monolayers, perhaps in driving the initial displacement of the lipid monomers. The fact

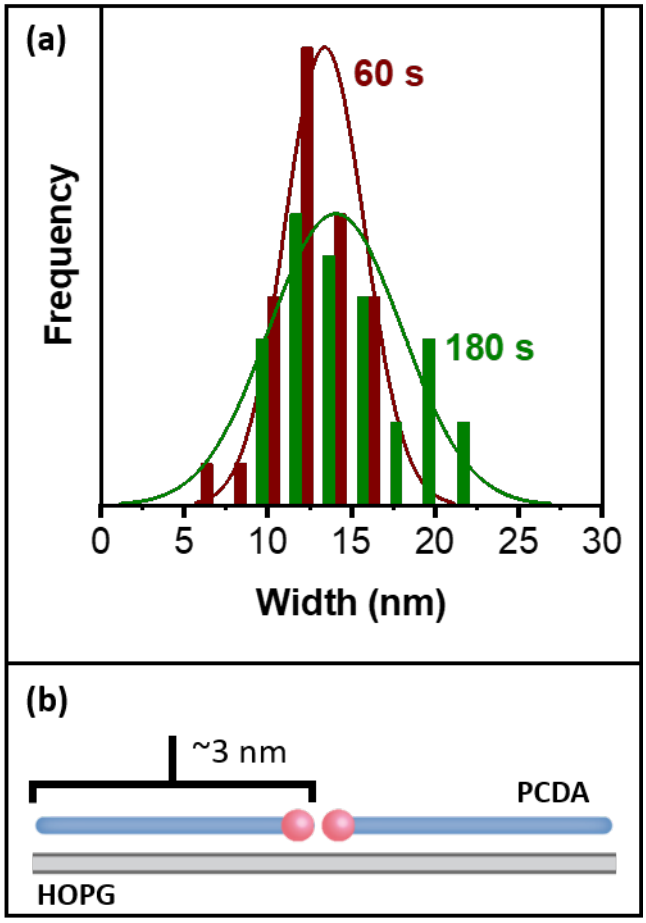

Figure 3.6.: (a) Corrected widths of Fmoc-FF tapes (12.5 μg/mL) incubated on PCDA in a solution of 75% H_2O. (b) Schematic highlighting the 3 nm monomer unit of the PCDA monolayer.

that Z-FF assembles more slowly than Fmoc-FF indicates that modifications to the protecting group could be exploited to further refine tape growth.

3.3 Summary and Future Plans

Passivation of HOPG with lying-down SAMs of PCDA and diyne PE induces the growth of epitaxially aligned crystals of Fmoc-FF peptides. Lowering the solvent dielectric inhibits assembly, suggesting that aromatic interactions play a role in the self-assembly process. Based on the observed tape heights and widths, we spec-

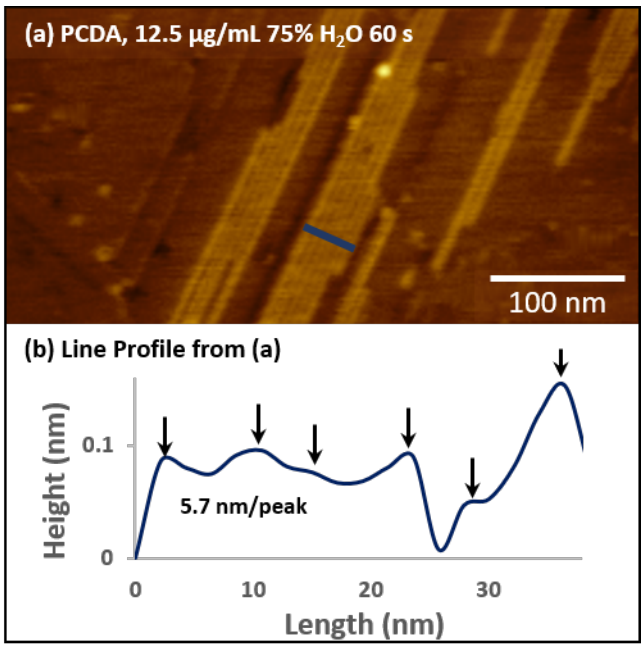

Figure 3.7.: (a) AFM image of PCDA incubated with 12.5 μg/mL Fmoc-FF in 75% H_2O for 60 s, with the blue line showing where the line profile was extracted. (b) Line profile extracted from (a)

ulate that the Fmoc-FF tapes nucleate at high surface energy defects in the lipid monolayer (e.g. domain boundaries) and grow by displacing the lipids, enabling peptides to interact directly with HOPG. Corrected tape widths support the monolayer lamellar structure modulating the dimensions of the tape, though the exact mechanism is not known. Current work investigates the roles of head group architecture and polymerization in nucleating the peptide tapes. Fmoc-FF is being incubated on both polymerized and unpolymerized monolayers of 10-12-Pentacosadiyne (PCD), an analog to PCDA, which lacks a headgoup. Additionally, molecular models are being tested to investigate the early stages of Fmoc-FF nucleation, specifically the thermodynamics of the Fmoc group substituting the lipid monomers.

While lying-down monolayers of lipids show utility for extending nanoscale control to the self-assembly of aromatic peptide structures, understanding and controlling the peptide-peptide and peptide-monolayer interactions requires more research. However,

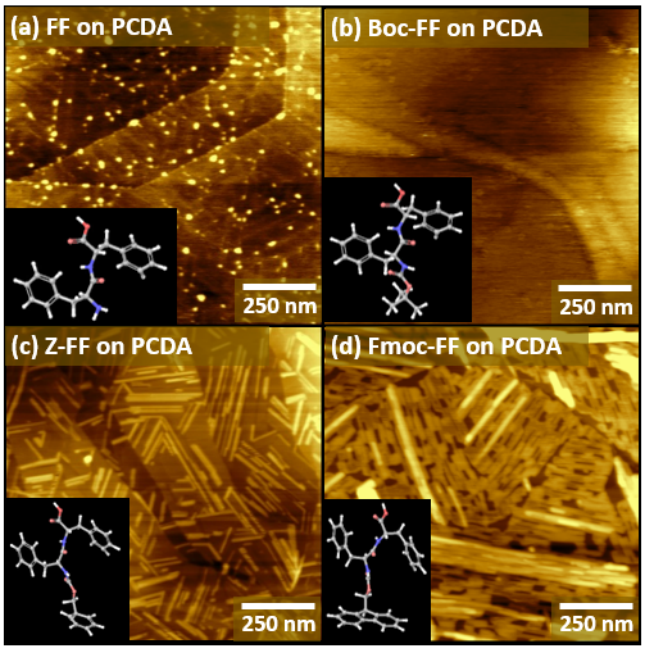

Figure 3.8.: AFM Imges of PCDA incubated with 25 μg/mL (a) FF, (b) Boc-FF, (c) Z-FF and (d) Fmoc-FF for 60 s.

exploiting these self-assembly principles towards generating aromatic peptide nanostructures with sub-10-nm resolution potentially translates to other organic semiconductor precursors. Therefore, noncovalent lying-down phase lipid monolayers serve as a promising template for facilitating the fabrication and performance of OPVs.

3.4 Experimental Methods

3.4.1 Materials

10,12-Pentacosadiynoic acid (PCDA, $\geq$ 97.0% purity), dichloromethane and 1,1,1,3,3,3-hexafluoro-2-propanol (HFP) were purchased from Sigma-Aldrich (St. Louis, MO), and used as received. Chloroform (ChromAR grade) was purchased from Macron Fine Chemicals (Center Valley, PA) and used as received. Fluorenyl-9-methoxycarbonyl-diphenylalanine (Fmoc-FF) was purchased from BaChem (Bubendorf, Switzerland) and used as received. 1,2-bis(10,12-tricosadiynoyl)-sn-glycero-3-

phosphoethanolamine (diyne PE, >99% purity) was purchased from Avanti Polar Lipids (Alabaster, AL) and used as received. Self-assembled monolayers of lipids were deposited on highly oriented pyrolytic graphite (HOPG, SPI Supplies, West Chester, PA) substrates; HOPG was freshly cleaved immediately prior to sample deposition. All initial steps in the deposition process were carried out under UV-filtered light to prevent premature polymerization.

3.4.2 Langmuir-Schaefer Conversion

LS conversion was performed using a KSV-NIMA Langmuir-Blodgett trough (Biolin Scientific, Stockholm, Sweden). In a typical PCDA transfer, 12 μL of a 0.75 mg/mL solution of PCDA in chloroform was deposited on a subphase of deionized water (18 MΩcm). After the small amount of chloroform used for amphiphile transfer was allowed to evaporate, trough barriers were slowly moved inward to adjust the mean molecular area. For diyne PE, the process was the same, except the deposition was carried out using a 0.5 mg/mL diyne PE solution in dichloromethane.

During trough equilibration and compression, HOPG substrates were cleaved and kept at 120 °C on a hotplate prior to dipping.

When the Langmuir film was compressed to the desired mean molecular area (e.g. 30 Å^2/molecule for PCDA) or surface pressure (e.g. 16 mN/m for diyne PE), the HOPG substrate was slowly lowered onto the subphase with the cleaved surface facing down, nearly parallel to the liquid interface. Sample translation was performed using an automated dipper that suspends the sample on a hanging wire, to maximize stability of the substrate-subphase contact. In the case of diyne PE, a heated dipper head set to 60 °C was used to suspend the substrate. After 4 min in contact with the liquid interface, the substrate was gently lifted out of contact with the liquid using the automated dipper. Samples prepared in this manner were immediately blown dry with N_2. The substrates were either used immediately for Fmoc-FF incubation studies, or stored in the dark to avoid photopolymerization.

3.4.3 Incubation of Fmoc-FF Peptides

Fmoc-FF was dissolved in HFP to a concentration of 5 mg/mL. This stock solution was then diluted down to the required HFP solution concentration for each incubation. Fresh HFP sock solutions were made for every series of incubations. A 100 μL drop of either 1:3 MeOH:H_2O (by volume) or DI H_2O was deposited on a given substrate and 1 μL of the HFP Fmoc-FF solution delivered into the water drop, for an aqueous concentration of 0.01X the initial concentration in HFP. Following incubation, the drop was blown off with N_2 after the required incubation time.

3.4.4 AFM Imaging

All AFM measurements were performed in tapping mode under ambient conditions (in air) using a Bruker (Bruker Instruments, Billerica, MA) MultiMode AFM equipped with an E scanner with 0.01-0.025 Ohm-cm Antimony (n)-doped Si Bruker RFESP-75 tips (nominal force constant 3 N/m and radius of curvature <12 nm).

3.4.5 Image Analysis

Images were processed using Gwyddion [102] scanning probe microscopy data visualization and analysis software to perform median line corrections, plane flattening, scar artifact removal, and contrast adjustment.

3.4.6 Energy Minimization

Software packages Maestro [103] and Macromodel [104] were used, respectively, to visualize molecular structures and to perform force field minimizations. Models were minimized using the OPLS_2005 force field [105], with normal cutoffs for Van der Waals, electrostatic and hydrogen bonding interactions. PCDA monolayers were assembled by organizing 128 molecules on top of a layer of graphene. The PCDA monomers were arranged into 4 columns of 32 molecules each, forming hy-

drogen bonded dimers between each pair of molecules. Diyne PE monolayers were constructed identically, except that 64 molecules were used. All monolayers were first minimized prior to the addition of a peptide layer. All calculations were executed with the built in water force field the graphene layer frozen. Minimizations were performed using the Polak-Ribiere conjugate gradient (PRCG) algorithm and gradient method with 50000 runs and a convergence threshold of 0.05 kJ/molÅ.

REFERENCES

[1] Jason a. Mann and William Robert Dichtel. Noncovalent functionalization of graphene by molecular and polymeric adsorbates. *Journal of Physical Chemistry Letters*, 4(16):2649–2657, 2013.

[2] J. M. Macleod and F. Rosei. Molecular self-assembly on graphene. *Small*, 10(6):1038–1049, 2014.

[3] Xiao Huang, Xiaoying Qi, Freddy Boey, and Hua Zhang. Graphene-based composites. *Chemical Society Reviews*, 41(2):666–686, 2012.

[4] Bing Li, Alexander V. Klekachev, Mirco Cantoro, Cedric Huyghebaert, André Stesmans, Inge Asselberghs, Stefan De Gendt, and Steven De Feyter. Toward tunable doping in graphene FETs by molecular self-assembled monolayers. *Nanoscale*, 5(20):9640–9644, 2013.

[5] D. Cui, J. M. Macleod, M. Ebrahimi, D. F. Perepichka, and F. Rosei. Solution and air stable host/guest architectures from a single layer covalent organic framework. *Chemical Communications*, 51(92):16510–16513, 2015.

[6] Shane R. Russell and Shelley A. Claridge. Peptide interfaces with graphene: An emerging intersection of analytical chemistry, theory, and materials. *Analytical and Bioanalytical Chemistry*, 408(11):2649–2658, 2016.

[7] Jae Jin Bang, Kortney K. Rupp, Shane R. Russell, Shi Wah Choong, and Shelley A. Claridge. Sitting Phases of Polymerizable Amphiphiles for Controlled Functionalization of Layered Materials. *Journal of the American Chemical Society*, 138(13):4448–4457, 2016.

[8] Kian Ping Loh, Shi Wun Tong, and Jishan Wu. Graphene and Graphene-like Molecules: Prospects in Solar Cells. *Journal of the American Chemical Society*, 138(4):1095–1102, 2016.

[9] Shu Zhong, Jian Qiang Zhong, Hong Ying Mao, Rui Wang, Yu Wang, Dong Chen Qi, Kian Ping Loh, Andrew Thye Shen Wee, Zhi Kuan Chen, and Wei Chen. CVD graphene as interfacial layer to engineer the organic donor-acceptor heterojunction interface properties. *ACS Applied Materials and Interfaces*, 4(6):3134–3140, 2012.

[10] Cécile Vigier-Carrière, Fouzia Boulmedais, Pierre Schaaf, and Loïc Jierry. Surface-Assisted Self-Assembly Strategies Leading to Supramolecular Hydrogels. *Angewandte Chemie - International Edition*, 57(6):1448–1456, 2018.

[11] Rui Li, Natasha L. McRae, Daniel R. McCulloch, Mitchell Boyd-Moss, Colin J. Barrow, David R. Nisbet, Nicole Stupka, and Richard J. Williams. Large and Small Assembly: Combining Functional Macromolecules with Small Peptides to Control the Morphology of Skeletal Muscle Progenitor Cells. *Biomacromolecules*, 19(3):825–837, 2018.

[12] Oleksandr V. Mikhnenko, Paul W. M. Blom, and Thuc-Quyen Nguyen. Exciton diffusion in organic semiconductors. *Energy Environ. Sci.*, 8:1867–1888, 2015.

[13] Wayne M. Moreau. *Semiconductor Lithography.* Springer US, Boston, MA, 1988.

[14] P. Rai-Choudhury and Society of Photo-optical Instrumentation Engineers. *Handbook of microlithography, micromachining, and microfabrication. Volume 1, Microlithography.* SPIE Opt. Engineer. Press, Bellingham, WA.

[15] D. Brambley, B. Martin, and P. D. Prewett. Microlithography: An overview. *Advanced Materials for Optics and Electronics*, 4(2):55–74, mar 1994.

[16] Younan Xia and George M. Whitesides. Soft Lithography. *Annual Review of Materials Science*, 28(1):153–184, 1998.

[17] R S Kane, S Takayama, E Ostuni, D E Ingber, and G M Whitesides. Patterning proteins and cells using soft lithograpy. *American Journal of Hospital Pharmacy*, 51(9):1156, 1994.

[18] Richard D. Piner, Jin Zhu, Feng Xu, Seunghun Hong, and Chad A. Mirkin. "dip-pen" nanolithography. *Science*, 283(5402):661–663, 1999.

[19] Miri Park, Christopher Harrison, Paul M. Chaikin, Richard A. Register, and Douglas H. Adamson. Block copolymer lithography: Periodic arrays of 1011 holes in 1 square centimeter. *Science*, 276(5317):1401–1404, 1997.

[20] Sang Ouk Kim, Harun H. Solak, Mark P. Stoykovich, Nicola J. Ferrier, Juan J. de Pablo, and Paul F. Nealey. Epitaxial self-assembly of block copolymers on lithographically defined nanopatterned substrates. *Nature*, 424(6947):411–414, jul 2003.

[21] Alfred Y. Lee, Abraham Ulman, and Allan S. Myerson. Crystallization of amino acids on self-assembled monolayers of rigid thiols on gold. *Langmuir*, 18(15):5886–5898, 2002.

[22] Aniruddh Singh, In Sung Lee, Kitae Kim, and Allan S. Myerson. Crystal growth on self-assembled monolayers. *CrystEngComm*, 13(1):24–32, dec 2011.

[23] K. S. Novoselov, A. K. Geim, S. V. Morozov, D. Jiang, Y. Zhang, S. V. Dubonos, I. V. Grigorieva, and A. A. Firsov. Electric field effect in atomically thin carbon films. *Science*, 306(5696):666–669, 2004.

[24] Changgu Lee, Xiaoding Wei, Jeffrey W. Kysar, and James Hone. Measurement of the elastic properties and intrinsic strength of monolayer graphene. *Science*, 321(5887):385–388, 2008.

[25] Yoshimichi Yui. Purchases of condominiums by single women and their backgrounds in Tokyo: Housing problems for women. *Geographical Review of Japan*, 79(12):165–179, 2006.

[26] Thomas Alava, Jason A. Mann, Cécile Théodore, Jaime J. Benitez, William R. Dichtel, Jeevak M. Parpia, and Harold G. Craighead. Control of the graphene-protein interface is required to preserve adsorbed protein function. *Analytical Chemistry*, 85(5):2754–2759, 2013.

[27] Priscilla Kailian Ang, Manu Jaiswal, Candy Haley Yi Xuan Lim, Yu Wang, Jagadish Sankaran, Ang Li, Chwee Teck Lim, Thorsten Wohland, Ozyilmaz Barbaros, and Kian Ping Loh. A bioelectronic platform using a graphene-lipid bilayer interface. *ACS Nano*, 4(12):7387–7394, 2010. PMID: 21067155.

[28] Jennifer F. Campbell, Ingrid Tessmer, H. Holden Thorp, and Dorothy A. Erie. Atomic force microscopy studies of dna-wrapped carbon nanotube structure and binding to quantum dots. *Journal of the American Chemical Society*, 130(32):10648–10655, 2008. PMID: 18627153.

[29] Feng Zhang, Hai Ning Du, Zhi Xiang Zhang, Li Na Ji, Hong Tao Li, Lin Tang, Hua Bin Wang, Chun Hai Fan, Hong Jie Xu, Yi Zhang, Jun Hu, Hong Yu Hu, and Jian Hua He. Epitaxial growth of peptide nanofilaments on inorganic surfaces: Effects of interfacial hydrophobicity/hydrophilicity. *Angewandte Chemie - International Edition*, 45(22):3611–3613, may 2006.

[30] Seung Gu Kang, Tien Huynh, Zhen Xia, Yi Zhang, Haiping Fang, Guanghong Wei, and Ruhong Zhou. Hydrophobic interaction drives surface-assisted epitaxial assembly of amyloid-like peptides. *Journal of the American Chemical Society*, 135(8):3150–3157, 2013.

[31] Catherine M. Kelly, Thomas Northey, Kate Ryan, Bernard R. Brooks, Andrei L. Kholkin, Brian J. Rodriguez, and Nicolae Viorel Buchete. Conformational dynamics and aggregation behavior of piezoelectric diphenylalanine peptides in an external electric field. *Biophysical Chemistry*, 196:16–24, 2015.

[32] Y. Okawa and M. Aono. Linear chain polymerization initiated by a scanning tunneling microscope tip at designated positions. *Journal of Chemical Physics*, 115(5):2317–2323, 2001.

[33] Yuji Okawa, Megumi Akai-Kasaya, Yuji Kuwahara, Swapan K. Mandal, and Masakazu Aono. Controlled chain polymerisation and chemical soldering for single-molecule electronics. *Nanoscale*, 4(10):3013–3028, 2012.

[34] Elisseos Verveniotis, Yuji Okawa, Marina V. Makarova, Yasuo Koide, Jiangwei Liu, Bretislav Smd, Kenji Watanabe, Takashi Taniguchi, Katsuyoshi Komatsu, Takeo Minari, Xuying Liu, Christian Joachim, and Masakazu Aono. Self-assembling diacetylene molecules on atomically flat insulators. *Physical Chemistry Chemical Physics*, 18(46):31600–31605, 2016.

[35] Tyler R. Hayes, Jae Jin Bang, Tyson C. Davis, Caroline F. Peterson, David G. McMillan, and Shelley A. Claridge. Multimicrometer Noncovalent Monolayer Domains on Layered Materials through Thermally Controlled Langmuir-Schaefer Conversion for Noncovalent 2D Functionalization. *ACS Applied Materials and Interfaces*, 9(41):36409–36416, 2017.

[36] Shi Wah Choong, Shane R. Russell, Jae Jin Bang, Justin K. Patterson, and Shelley A. Claridge. Sitting Phase Monolayers of Polymerizable Phospholipids

Create Dimensional, Molecular-Scale Wetting Control for Scalable Solution-Based Patterning of Layered Materials. *ACS Applied Materials and Interfaces*, 9(22):19326–19334, 2017.

[37] Terry A. Villarreal, Shane R. Russell, Jae Jin Bang, Justin K. Patterson, and Shelley A. Claridge. Modulating Wettability of Layered Materials by Controlling Ligand Polar Headgroup Dynamics. *Journal of the American Chemical Society*, 139(34):11973–11979, 2017.

[38] Tyson C. Davis, Jae Jin Bang, Jacob T. Brooks, David G. McMillan, and Shelley A. Claridge. Hierarchically Patterned Noncovalent Functionalization of 2D Materials by Controlled Langmuir-Schaefer Conversion. *Langmuir*, 34(4):1353–1362, 2018.

[39] T. Buffeteau, B. Desbat, and J. M. Turlet. Polarization modulation ft-ir spectroscopy of surfaces and ultra-thin films: Experimental procedure and quantitative analysis. *Appl. Spectrosc.*, 45(3):380–389, Mar 1991.

[40] Mila Boncheva and Horst Vogel. Formation of stable polypeptide monolayers at interfaces: controlling molecular conformation and orientation. *Biophysical Journal*, 73(2):1056 – 1072, 1997.

[41] Daniel Blaudez, Thierry Buffeteau, Bernard Desbat, and Jean Marie Turlet. Infrared and raman spectroscopies of monolayers at the airwater interface. *Current Opinion in Colloid Interface Science*, 4(4):265 – 272, 1999.

[42] Barbara J. Barner, Michael J. Green, Edna I. Saez, and Robert M. Corn. Polarization modulation fourier transform infrared reflectance measurements of thin films and monolayers at metal surfaces utilizing real-time sampling electronics. *Analytical Chemistry*, 63(1):55–60, 1991.

[43] Michael J. Green, Barbara J. Barner, and Robert M. Corn. Realtime sampling electronics for double modulation experiments with fourier transform infrared spectrometers. *Review of Scientific Instruments*, 62(6):1426–1430, 1991.

[44] J. F. Rabolt, F. C. Burns, N. E. Schlotter, and J. D. Swalen. Molecular orientation in thin monolayer films by infrared spectroscopy. *Journal of Electron Spectroscopy and Related Phenomena*, 30(1):29–34, 1983.

[45] C. Naselli, J. F. Rabolt, and J. D. Swalen. Orderdisorder transitions in LangmuirBlodgett monolayers. I. Studies of twodimensional melting by infrared spectroscopy. *The Journal of Chemical Physics*, 82(4):2136–2140, 1985.

[46] Askari. Mohammad Bagher. Introduction to organic solar cells. *Sustainable Energy*, 2(3):85–90, 2014.

[47] Christina L. Brown, Ilhan A. Aksay, Dudley A. Saville, and Michael H. Hecht. Template-directed assembly of a de novo designed protein. *Journal of the American Chemical Society*, 124(24):6846–6848, 2002.

[48] Richard G. Weiss. The past, present, and future of molecular gels. What is the status of the field, and where is it going? *Journal of the American Chemical Society*, 136(21):7519–7530, 2014.

[49] Maria Galini Faidra Angelerou, Akmal Sabri, Rhiannon Creasey, Polyxeni Angelerou, Maria Marlow, and Mischa Zelzer. Surface-directed modulation of supramolecular gel properties. *Chemical Communications*, 52(23):4298–4300, 2016.

[50] Sang N. Kim, Zhifeng Kuang, Joseph M. Slocik, Sharon E. Jones, Yue Cui, Barry L. Farmer, Michael C. McAlpine, and Rajesh R. Naik. Preferential binding of peptides to graphene edges and planes. *Journal of the American Chemical Society*, 133(37):14480–14483, 2011.

[51] Yue Cui, Sang N. Kim, Sharon E. Jones, Laurie L. Wissler, Rajesh R. Naik, and Michael C. McAlpine. Chemical functionalization of graphene enabled by phage displayed peptides. *Nano Letters*, 10(11):4559–4565, 2010.

[52] Brahim Akdim, Ruth Pachter, Steve S. Kim, Rajesh R. Naik, Tiffany R. Walsh, Steven Trohalaki, Gongyi Hong, Zhifeng Kuang, and Barry L. Farmer. Electronic properties of a graphene device with peptide adsorption: Insight from simulation. *ACS Applied Materials and Interfaces*, 5(15):7470–7477, 2013.

[53] Ras B. Pandey, Hendrik Heinz, Barry L. Farmer, Lawrence F. Drummy, Sharon E. Jones, Richard A. Vaia, and Rajesh R. Naik. Layer of clay platelets in a peptide matrix: Binding, encapsulation, and morphology. *Journal of Polymer Science, Part B: Polymer Physics*, 48(24):2566–2574, 2010.

[54] Zak E. Hughes and Tiffany R. Walsh. What makes a good graphene-binding peptide? Adsorption of amino acids and peptides at aqueous graphene interfaces. *Journal of Materials Chemistry B*, 3(16):3211–3221, 2015.

[55] Meital Reches and Ehud Gazit. Designed aromatic homo-dipeptides: Formation of ordered nanostructures and potential nanotechnological applications. *Physical Biology*, 3(1):S10–S19, 2006.

[56] Ehud Gazit. Self-assembled peptide nanostructures: The design of molecular building blocks and their technological utilization. *Chemical Society Reviews*, 36(8):1263–1269, 2007.

[57] Meital Reches and Ehud Gazit. Casting metal nanowires within discrete self-assembled peptide nanotubes. *Science*, 300(5619):625–627, 2003.

[58] Claire Tang, Andrew M. Smith, Richard F. Collins, Rein V. Ulijn, and Alberto Saiani. Fmoc-Diphenylalanine Self-ASsembly Mechanism Induces Apparent pKaShifts. *Langmuir*, 25(16):9447–9453, 2009.

[59] Kai Tao, Pandeeswar Makam, Ruth Aizen, and Ehud Gazit. Self-assembling peptide semiconductors. *Science*, 358(6365):eaam9756, nov 2017.

[60] Brahim Akdim, Ruth Pachter, and Rajesh R. Naik. Self-assembled peptide nanotubes as electronic materials: An evaluation from first-principles calculations. *Applied Physics Letters*, 106(18):183707, may 2015.

[61] Dorothea Pinotsi, Luca Grisanti, Pierre Mahou, Ralph Gebauer, Clemens F. Kaminski, Ali Hassanali, and Gabriele S. Kaminski Schierle. Proton Transfer and Structure-Specific Fluorescence in Hydrogen Bond-Rich Protein Structures. *Journal of the American Chemical Society*, 138(9):3046–3057, mar 2016.

[62] Vu Nguyen, Ren Zhu, Kory Jenkins, and Rusen Yang. Self-assembly of diphenylalanine peptide with controlled polarization for power generation. *Nature Communications*, 7:6, 2016.

[63] Meiling Lian, Xu Chen, Yanluo Lu, and Wensheng Yang. Self-Assembled Peptide Hydrogel as a Smart Biointerface for Enzyme-Based Electrochemical Biosensing and Cell Monitoring. *ACS Applied Materials and Interfaces*, 8(38):25036–25042, 2016.

[64] Cong Guo, Zohar A. Arnon, Ruxi Qi, Qingwen Zhang, Lihi Adler-Abramovich, Ehud Gazit, and Guanghong Wei. Expanding the nanoarchitectural diversity through aromatic di- and tri-peptide coassembly: Nanostructures and molecular mechanisms. *ACS Nano*, 10(9):8316–8324, 2016. PMID: 27548765.

[65] Wim G.J. Hol, Louis M. Halie, and Christian Sander. Dipoles of the α-helix and β-sheet: Their role in protein folding. *Nature*, 294(5841):532–536, 1981.

[66] W. G.J. Hol, P. T. Van Duijnen, and H. J.C. Berendsen. The α-helix dipole and the properties of proteins. *Nature*, 273(5662):443–446, 1978.

[67] Kazukuni Tahara, Keisuke Katayama, Matthew Oliver Blunt, Kohei Iritani, Steven De Feyter, and Yoshito Tobe. Functionalized surface-confined pores: Guest binding directed by lateral noncovalent interactions at the solid-liquid interface. *ACS Nano*, 8(8):8683–8694, 2014.

[68] J. J. Bang, S. R. Russell, K. K. Rupp, and S. A. Claridge. Multimodal scanning probe imaging: Nanoscale chemical analysis from biology to renewable energy. *Analytical Methods*, 7(17):7106–7127, 2015.

[69] Shuai Wang, Priscilla Kailian Ang, Ziqian Wang, Ai Ling Lena Tang, John T.L. Thong, and Kian Ping Loh. High mobility, printable, and solution-processed graphene electronics. *Nano Letters*, 10(1):92–98, 2010.

[70] A. H. Castro Neto, F. Guinea, N. M. R. Peres, K. S. Novoselov, and A. K. Geim. The electronic properties of graphene. *Rev. Mod. Phys.*, 81:109–162, Jan 2009.

[71] Yuanbo Zhang, Yan Wen Tan, Horst L. Stormer, and Philip Kim. Experimental observation of the quantum Hall effect and Berry's phase in graphene. *Nature*, 438(7065):201–204, 2005.

[72] Aparna Deshpande, Chun Hong Sham, Justice M.P. Alaboson, Jonathan M. Mullin, George C. Schatz, and Mark C. Hersam. Self-assembly and photopolymerization of sub-2 nm one-dimensional organic nanostructures on graphene. *Journal of the American Chemical Society*, 134(40):16759–16764, 2012.

[73] Qing Hua Wang and Mark C. Hersam. Room-temperature molecular-resolution characterization of self-assembled organic monolayers on epitaxial graphene. *Nature Chemistry*, 1(3):206–211, 2009.

[74] Haifeng Ma, Lita Lee, Paula A. Brooksby, Simon A. Brown, Sara J. Fraser, Keith C. Gordon, Yann R. Leroux, Philippe Hapiot, and Alison J. Downard. Scanning tunneling and atomic force microscopy evidence for covalent and noncovalent interactions between aryl films and highly ordered pyrolytic graphite. *Journal of Physical Chemistry C*, 118(11):5820–5826, 2014.

[75] Yan Yang and Matthew B. Zimmt. Shape amphiphiles in 2-d: Assembly of 1-d stripes and control of their surface density. *Journal of Physical Chemistry B*, 119(24):7740–7748, 2015.

[76] Tamara Elzein, Ahmad Fahs, Maurice Brogly, Amina Elhiri, Bénédicte Lepoittevin, Philippe Roger, and Véronique Planchot. Adsorption of alkanethiols on gold surfaces: PM-IRRAS study of the influence of terminal functionality on alkyl chain orientation. *Journal of Adhesion*, 89(5):416–432, 2013.

[77] Robert V. Duevel, Robert M. Corn, Min D. Liu, and Charles R. Leidner. Orientation and organization in functionalized phospholipid monolayers at gold surfaces as measured by polarization modulation Fourier transform infrared spectroscopy. *Journal of Physical Chemistry*, 96(1):468–473, 1992.

[78] Justice M P Alaboson, Chun Hong Sham, Sumit Kewalramani, Jonathan D. Emery, James E. Johns, Aparna Deshpande, Teyu Chien, Michael J. Bedzyk, Jeffrey W. Elam, Michael J. Pellin, and Mark C. Hersam. Templating sub-10 nm atomic layer deposited oxide nanostructures on graphene via one-dimensional organic self-assembled monolayers. *Nano Letters*, 13(12):5763–5770, 2013.

[79] Sebastian Wickenburg, Jiong Lu, Johannes Lischner, Hsin Zon Tsai, Arash A. Omrani, Alexander Riss, Christoph Karrasch, Aaron Bradley, Han Sae Jung, Ramin Khajeh, Dillon Wong, Kenji Watanabe, Takashi Taniguchi, Alex Zettl, A. H.Castro Neto, Steven G. Louie, and Michael F. Crommie. Tuning charge and correlation effects for a single molecule on a graphene device. *Nature Communications*, 7, 2016.

[80] Kunal S. Mali, Nicholas Pearce, Steven De Feyter, and Neil R. Champness. Frontiers of supramolecular chemistry at solid surfaces. *Chemical Society Reviews*, 46(9):2520–2542, 2017.

[81] Roald Phillipson, César J. Lockhart De La Rosa, Joan Teyssandier, Peter Walke, Deepali Waghray, Yasuhiko Fujita, Jinne Adisoejoso, Kunal S. Mali, Inge Asselberghs, Cedric Huyghebaert, Hiroshi Uji-I, Stefan De Gendt, and Steven De Feyter. Tunable doping of graphene by using physisorbed self-assembled networks. *Nanoscale*, 8(48):20017–20026, 2016.

[82] Rajiv Giridharagopal and Kevin F. Kelly. Substrate-dependent properties of polydiacetylene nanowires on graphite and Mo S2. *ACS Nano*, 2(8):1571–1580, 2008.

[83] G. C. McGonigal, R. H. Bernhardt, and D. J. Thomson. Imaging alkane layers at the liquid/graphite interface with the scanning tunneling microscope. *Applied Physics Letters*, 57(1):28–30, 1990.

[84] A. J. Groszek. Selective Adsorption at Graphite/Hydrocarbon Interfaces. *Proceedings of the Royal Society A: Mathematical, Physical and Engineering Sciences*, 314(1519):473–498, 1970.

[85] Jürgen P. Rabe and Stefan Buchholz. Molecular structure and dynamics in monolayers of long chain alkanes and alkylderivatives. *Makromolekulare Chemie. Macromolecular Symposia*, 50(1):261–268, 1991.

[86] B. Tieke, H. J. Graf, G. Wegner, B. Naegele, H. Ringsdorf, A. Banerjie, D. Day, and J. B. Lando. Polymerization of mono- and multilayer forming diacetylenes. *Colloid and Polymer Science Kolloid-Zeitschrift & Zeitschrift für Polymere*, 255(6):521–531, 1977.

[87] Günter Lieser, Bernd Tieke, and Gerhard Wegner. Structure, phase transitions and polymerizability of multilayers of some diacetylene monocarboxylic acids. *Thin Solid Films*, 68(1):77–90, 1980.

[88] Shuxia Yin, Chen Wang, Xiaohui Qiu, Xu Bo, and Chunli Bai. Theoretical study of the effects of intermolecular interactions in self-assembled long-chain alkanes adsorbed on graphite surface. *Surface and Interface Analysis*, 32(1):248–252, 2001.

[89] Yuji Okawa, Daisuke Takajo, Shigeru Tsukamoto, Tsuyoshi Hasegawa, and Masakazu Aono. Atomic force microscopy and theoretical investigation of the lifted-up conformation of polydiacetylene on a graphite substrate. *Soft Matter*, 4(5):1041–1047, 2008.

[90] Asen Asenov, Savas Kaya, and Andrew R. Brown. Intrinsic parameter fluctuations in decananometer MOSFETs introduced by gate line edge roughness. *IEEE Transactions on Electron Devices*, 50(5):1254–1260, 2003.

[91] R. Fabian Pease and Stephen Y. Chou. Lithography and other patterning techniques for future electronics. *Proceedings of the IEEE*, 96(2):248–270, 2008.

[92] Kunal S. Mali, John Greenwood, Jinne Adisoejoso, Roald Phillipson, and Steven De Feyter. Nanostructuring graphene for controlled and reproducible functionalization. *Nanoscale*, 7(5):1566–1585, 2015.

[93] Daisuke Takajo, Yuji Okawa, Tsuyoshi Hasegawa, and Masakazu Aono. Chain polymerization of diacetylene compound multilayer films on the topmost surface initiated by a scanning tunneling microscope tip. *Langmuir*, 23(10):5247–5250, 2007.

[94] R. A. MacPhail, H. L. Strauss, R. G. Snyder, and C. A. Elliger. Carbon-hydrogen stretching modes and the structure of n-alkyl chains. 2. Long, all-trans chains. *The Journal of Physical Chemistry*, 88(3):334–341, 1984.

[95] R. A. MacPhail, H. L. Strauss, R. G. Snyder, and C. A. Elliger. Carbon-hydrogen stretching modes and the structure of n-alkyl chains. 2. Long, all-trans chains. *The Journal of Physical Chemistry*, 88(3):334–341, 1984.

[96] Evangelina Pensa, Carolina Vericat, Doris Grumelli, Roberto C. Salvarezza, Sung Hyun Park, Gabriel S. Longo, Igal Szleifer, and Lucila P. Méndez De Leo. New insight into the electrochemical desorption of alkanethiol SAMs on gold. *Physical Chemistry Chemical Physics*, 14(35):12355–12367, 2012.

[97] Antonella Badia, Louis Cuccia, Linette Demers, Fred Morin, and R. Bruce Lennox. Structure and dynamics in alkanethiolate monolayers self-assembled on gold nanoparticles: A DSC, FT-IR, and deuterium NMR study. *Journal of the American Chemical Society*, 119(11):2682–2692, 1997.

[98] Thomas Leitner, Jürgen Kattner, and Helmuth Hoffmann. Infrared reflection spectroscopy of thin films on highly oriented pyrolytic graphite. *Applied Spectroscopy*, 57(12):1502–1509, 2003.

[99] Michaël A. Ramin, Gwénaëlle Le Bourdon, Karine Heuzé, Marie Degueil, Colette Belin, Thierry Buffeteau, Bernard Bennetau, and Luc Vellutini. Functionalized hydrogen-bonding self-assembled monolayers grafted onto SiO2substrates. *Langmuir*, 28(51):17672–17680, 2012.

[100] J. Saccani, T. Buffeteau, B. Desbat, and D. Blaudez. Increasing Detectivity of Polarization Modulation Infrared Reflection-Absorption Spectroscopy for the Study of Ultrathin Films Deposited on Various Substrates. *Applied Spectroscopy*, 57(10):1260–1265, 2003.

[101] Lingzi Sang, Anoma Mudalige, Ajaya K. Sigdel, Anthony J. Giordano, Seth R. Marder, Joseph J. Berry, and Jeanne E. Pemberton. PM-IRRAS determination of molecular orientation of phosphonic acid self-assembled monolayers on indium zinc oxide. *Langmuir*, 31(20):5603–5613, 2015.

[102] David Nečas and Petr Klapetek. Gwyddion: An open-source software for SPM data analysis. *Central European Journal of Physics*, 10(1):181–188, 2012.

[103] Maestro, 2015.

[104] Macromodel, 2015.

[105] Jay L. Banks, Hege S. Beard, Yixiang Cao, Art E. Cho, Wolfgang Damm, Ramy Farid, Anthony K. Felts, Thomas A. Halgren, Daniel T. Mainz, Jon R. Maple, Robert Murphy, Dean M. Philipp, Matthew P. Repasky, Linda Y. Zhang, Bruce J. Berne, Richard A. Friesner, Emilio Gallicchio, and Ronald M. Levy. Integrated Modeling Program, Applied Chemical Theory (IMPACT). *Journal of Computational Chemistry*, 26(16):1752–1780, 2005.

[106] D. S.L. Abergel, V. Apalkov, J. Berashevich, K. Ziegler, and Tapash Chakraborty. Properties of graphene: A theoretical perspective. *Advances in Physics*, 59(4):261–482, 2010.

[107] F. Bonaccorso, Z. Sun, T. Hasan, and A. C. Ferrari. Graphene photonics and optoelectronics. *Nature Photonics*, 4(9):611–622, 2010.

[108] K. S. Novoselov, A. K. Geim, S. V. Morozov, D. Jiang, M. I. Katsnelson, I. V. Grigorieva, S. V. Dubonos, and A. A. Firsov. Two-dimensional gas of massless Dirac fermions in graphene. *Nature*, 438(7065):197–200, 2005.

[109] Vanesa C. Sanchez, Ashish Jachak, Robert H. Hurt, and Agnes B. Kane. Biological interactions of graphene-family nanomaterials: An interdisciplinary review. *Chemical Research in Toxicology*, 25(1):15–34, 2012.

[110] Sbastien Haar, Artur Ciesielski, Joseph Clough, Huafeng Yang, Raffaello Mazzaro, Fanny Richard, Simone Conti, Nicolas Merstorf, Marco Cecchini, Vittorio Morandi, Cinzia Casiraghi, and Paolo Samor. A supramolecular strategy to leverage the liquid-phase exfoliation of graphene in the presence of surfactants: Unraveling the role of the length of fatty acids. *Small*, 11(14):1691–1702, 2014.

[111] Hongkun He and Chao Gao. General approach to individually dispersed, highly soluble, and conductive graphene nanosheets functionalized by nitrene chemistry. *Chemistry of Materials*, 22(17):5054–5064, 2010.

[112] Yan-Li Zhao and J. Fraser Stoddart. Noncovalent Functionalization of Single-Walled Carbon Nanotubes. *Accounts of Chemical Research*, 42(8):1161–1171, 2009.

[113] Vasilios Georgakilas, Michal Otyepka, Athanasios B. Bourlinos, Vimlesh Chandra, Namdong Kim, K. Christian Kemp, Pavel Hobza, Radek Zboril, and Kwang S. Kim. Functionalization of graphene: Covalent and non-covalent approaches, derivatives and applications. *Chemical Reviews*, 112(11):6156–6214, 2012.

[114] Tapas Kuila, Saswata Bose, Ananta Kumar Mishra, Partha Khanra, Nam Hoon Kim, and Joong Hee Lee. Chemical functionalization of graphene and its applications. *Progress in Materials Science*, 57(7):1061–1105, 2012.

[115] Hatef Sadeghi, L. Algaragholy, T. Pope, S. Bailey, D. Visontai, D. Manrique, J. Ferrer, V. Garcia-Suarez, Sara Sangtarash, and Colin J. Lambert. Graphene sculpturene nanopores for DNA nucleobase sensing. *Journal of Physical Chemistry B*, 118(24):6908–6914, 2014.

[116] Yuyan Shao, Jun Wang, Hong Wu, Jun Liu, Ilhan A. Aksay, and Yuehe Lin. Graphene based electrochemical sensors and biosensors: A review. *Electroanalysis*, 22(10):1027–1036, 2010.

[117] Dmitriy Khatayevich, Tamon Page, Carolyn Gresswell, Yuhei Hayamizu, William Grady, and Mehmet Sarikaya. Selective detection of target proteins by peptide-enabled graphene biosensor. *Small*, 10(8):1505–1513, 2014.

[118] Lingyan Feng, Li Wu, and Xiaogang Qu. New horizons for diagnostics and therapeutic applications of graphene and graphene oxide. *Advanced Materials*, 25(2):168–186, 2013.

[119] Cassandra L. Weaver, Jaclyn M. Larosa, Xiliang Luo, and Xinyan Tracy Cui. Electrically controlled drug delivery from graphene oxide nanocomposite films. *ACS Nano*, 8(2):1834–1843, 2014.

[120] Andy H. Hung, Robert J. Holbrook, Matthew W. Rotz, Cameron J. Glasscock, Nikhita D. Mansukhani, Keith W. Macrenaris, Lisa M. Manus, Matthew C. Duch, Kevin T. Dam, Mark C. Hersam, and Thomas J. Meade. Graphene oxide enhances cellular delivery of hydrophilic small molecules by co-incubation. *ACS Nano*, 8(10):10168–10177, 2014.

[121] Sang Ha Hwang, Dongwoo Kang, Rodney S. Ruoff, Hyeon Suk Shin, and Young Bin Park. Poly(vinyl alcohol) reinforced and toughened with poly(dopamine)-treated graphene oxide, and its use for humidity sensing. *ACS Nano*, 8(7):6739–6747, 2014.

[122] Eddie Wang, Malav S. Desai, Kwang Heo, and Seung Wuk Lee. Graphene-based materials functionalized with elastin-like polypeptides. *Langmuir*, 30(8):2223–2229, 2014.

[123] Jinhui Wang, Xiaojia Zhao, Jingfeng Li, Xiao Kuang, Yuqian Fan, Gang Wei, and Zhiqiang Su. Electrostatic assembly of peptide nanofiber-biomimetic silver nanowires onto graphene for electrochemical sensors. *ACS Macro Letters*, 3(6):529–533, 2014.

[124] Zhiqiang Su, Huiyan Shen, Haixia Wang, Jinhui Wang, Jingfeng Li, Gerd Ulrich Nienhaus, Li Shang, and Gang Wei. Motif-Designed Peptide Nanofibers Decorated with Graphene Quantum Dots for Simultaneous Targeting and Imaging of Tumor Cells. *Advanced Functional Materials*, 25(34):5472–5478, 2015.

[125] Heeyoung Lee, Minh Hai Tran, Hae Kyung Jeong, Jinwoo Han, Sei Heon Jang, and Changwoo Lee. Nonspecific cleavage of proteins using graphene oxide. *Analytical Biochemistry*, 451(1):31–34, 2014.

[126] Tae Hee Han, Won Jun Lee, Duck Hyun Lee, Ji Eun Kim, Eun Young Choi, and Sang Ouk Kim. Peptide/graphene hybrid assembly into core/shell nanowires. *Advanced Materials*, 22(18):2060–2064, 2010.

[127] Vamsi K. Kodali, Jan Scrimgeour, Suenne Kim, John H. Hankinson, Keith M. Carroll, Walt A. De Heer, Claire Berger, and Jennifer E. Curtis. Nonperturbative chemical modification of graphene for protein micropatterning. *Langmuir*, 27(3):863–865, 2011.

[128] Xiaochen Dong, Yumeng Shi, Wei Huang, Peng Chen, and Lain Jong Li. Electrical detection of DNA hybridization with single-base specificity using transistors based on CVD-grown graphene sheets. *Advanced Materials*, 22(14):1649–1653, 2010.

[129] Wenrong Yang, Kyle R. Ratinac, Simon R. Ringer, Pall Thordarson, J. Justin Gooding, and Filip Braet. Carbon nanomaterials in biosensors: Should you use nanotubes or graphene. *Angewandte Chemie - International Edition*, 49(12):2114–2138, 2010.

[130] Wei Tao Huang, Hong Qun Luo, and Nian Bing Li. Boolean logic tree of graphene-based chemical system for molecular computation and intelligent molecular search query. *Analytical Chemistry*, 86(9):4494–4500, 2014.

[131] Ioannis V. Pavlidis, Michaela Patila, Uwe T. Bornscheuer, Dimitrios Gournis, and Haralambos Stamatis. Graphene-based nanobiocatalytic systems: Recent advances and future prospects. *Trends in Biotechnology*, 32(6):312–320, 2014.

[132] Christopher M. Dobson. Protein folding and misfolding. *Nature*, 426(6968):884–890, 2003.

[133] Tapas Kuila, Saswata Bose, Partha Khanra, Ananta Kumar Mishra, Nam Hoon Kim, and Joong Hee Lee. Recent advances in graphene-based biosensors. *Biosensors and Bioelectronics*, 26(12):4637–4648, 2011.

[134] Manu S. Mannoor, Hu Tao, Jefferson D. Clayton, Amartya Sengupta, David L. Kaplan, Rajesh R. Naik, Naveen Verma, Fiorenzo G. Omenetto, and Michael C. McAlpine. Graphene-based wireless bacteria detection on tooth enamel. *Nature Communications*, 3, 2012.

[135] Lihua Chen, Yuhong Li, Jianxu Li, Xueqing Xu, Ren Lai, and Quanming Zou. An antimicrobial peptide with antimicrobial activity against Helicobacter pylori. *Peptides*, 28(8):1527–1531, 2007.

[136] J. V. Solnick, L. M. Hansen, D. R. Canfield, and J. Parsonnet. Determination of the infectious dose of Helicobacter pylori during primary and secondary infection in rhesus monkeys (Macaca mulatta). *Infection and Immunity*, 69(11):6887–6892, 2001.

[137] Min Zhang, Bin Cheng Yin, Xian Fei Wang, and Bang Ce Ye. Interaction of peptides with graphene oxide and its application for real-time monitoring of protease activity. *Chemical Communications*, 47(8):2399–2401, 2011.

[138] Ying Wang, Zhaohui Li, Jun Wang, Jinghong Li, and Yuehe Lin. Graphene and graphene oxide: Biofunctionalization and applications in biotechnology. *Trends in Biotechnology*, 29(5):205–212, 2011.

[139] J. Christopher Love, Lara A. Estroff, Jennah K. Kriebel, Ralph G. Nuzzo, and George M. Whitesides. Self-assembled monolayers of thiolates on metals as a form of nanotechnology. *Chemical Reviews*, 105(4):1103–1169, 2005.

[140] Shelley A. Claridge, Jeffrey J. Schwartz, and Paul S. Weiss. Electrons, photons, and force: Quantitative single-molecule measurements from physics to biology. *ACS Nano*, 5(2):693–729, 2011.

[141] Shelley A. Claridge, Wei Ssu Liao, John C. Thomas, Yuxi Zhao, Huan H. Cao, Sarawut Cheunkar, Andrew C. Serino, Anne M. Andrews, and Paul S. Weiss. From the bottom up: Dimensional control and characterization in molecular monolayers. *Chemical Society Reviews*, 42(7):2725–2745, 2013.

[142] Anne Sophie Duwez. Exploiting electron spectroscopies to probe the structure and organization of self-assembled monolayers: A review. *Journal of Electron Spectroscopy and Related Phenomena*, 134(2-3):97–138, 2004.

[143] Alexandra Riposan and Gang Yu Liu. Significance of local density of states in the scanning tunneling microscopy imaging of alkanethiol self-assembled monolayers. *Journal of Physical Chemistry B*, 110(47):23926–23937, 2006.

[144] H. Klein, W. Blanc, R. Pierrisnard, C. Fauquet, and Ph Dumas. Self-assembled monolayers of decanethiol on Au(111)/mica. *European Physical Journal B*, 14(2):371–376, 2000.

[145] Xiaobo Mao, Yuanyuan Guo, Yin Luo, Lin Niu, Lei Liu, Xiaojing Ma, Huibin Wang, Yanlian Yang, Guanghong Wei, and Chen Wang. Sequence effects on peptide assembly characteristics observed by using scanning tunneling microscopy. *Journal of the American Chemical Society*, 135(6):2181–2187, 2013.

[146] Joanna Aizenberg. Crystallization in patterns: A bio-inspired approach. *Advanced Materials*, 16(15 SPEC. ISS.):1295–1302, 2004.

[147] Paul S. Weiss. Functional molecules and assemblies in controlled environments: Formation and measurements. *Accounts of Chemical Research*, 41(12):1772–1781, 2008.

[148] A. C. Ferrari, J. C. Meyer, V. Scardaci, C. Casiraghi, M. Lazzeri, F. Mauri, S. Piscanec, D. Jiang, K. S. Novoselov, S. Roth, and A. K. Geim. Raman spectrum of graphene and graphene layers. *Physical Review Letters*, 97(18), 2006.

[149] Mitchell B. Lerner, Felipe Matsunaga, Gang Hee Han, Sung Ju Hong, Jin Xi, Alexander Crook, Jose Manuel Perez-Aguilar, Yung Woo Park, Jeffery G. Saven, Renyu Liu, and A. T.Charlie Johnson. Scalable production of highly sensitive nanosensors based on graphene functionalized with a designed G protein-coupled receptor. *Nano Letters*, 14(5):2709–2714, 2014.

[150] Douglas A. Skoog, F. James Holler, and Stanley R. Crouch. *Principles of Instrumental Analysis, Sixth Edition*. Cengage, Stamford, CT, 2007.

[151] P. E. Batson, N. Dellby, and O. L. Krivanek. Sub-aångstrom resolution using aberration corrected electron optics. *Nature*, 418(6898):617–620, 2002.

[152] Chaoxu Li, Jozef Adamcik, and Raffaele Mezzenga. Biodegradable nanocomposites of amyloid fibrils and graphene with shape-memory and enzyme-sensing properties. *Nature Nanotechnology*, 7(7):421–427, 2012.

[153] Neil R. Wilson, Priyanka A. Pandey, Richard Beanland, Robert J. Young, Ian A. Kinloch, Lei Gong, Zheng Liu, Kazu Suenaga, Jonathan P. Rourke, Stephen J. York, and Jeremy Sloan. Graphene Oxide: Structural Analysis and Application as a Highly Transparent Support for Electron Microscopy. *ACS Nano*, 3(9):2547–2556, 2009.

[154] Jong Min Yuk, Jungwon Park, Peter Ercius, Kwanpyo Kim, Daniel J. Hellebusch, Michael F. Crommie, Jeong Yong Lee, A. Zettl, and A. Paul Alivisatos. High-resolution EM of colloidal nanocrystal growth using graphene liquid cells. *Science*, 335(6077):61–64, 2012.

[155] Jungwon Park, Hyesung Park, Peter Ercius, Adrian F. Pegoraro, Chen Xu, Jin Woong Kim, Sang Hoon Han, and David A. Weitz. Direct Observation of Wet Biological Samples by Graphene Liquid Cell Transmission Electron Microscopy. *Nano Letters*, 15(7):4737–4744, 2015.

[156] Ondrej L. Krivanek, Matthew F. Chisholm, Valeria Nicolosi, Timothy J. Pennycook, George J. Corbin, Niklas Dellby, Matthew F. Murfitt, Christopher S. Own, Zoltan S. Szilagyi, Mark P. Oxley, Sokrates T. Pantelides, and Stephen J. Pennycook. Atom-by-atom structural and chemical analysis by annular dark-field electron microscopy. *Nature*, 464(7288):571–574, 2010.

[157] Guangyan Qing, Shilong Zhao, Yüting Xiong, Ziyu Lv, Fenglei Jiang, Yi Liu, Hui Chen, Mingxi Zhang, and Taolei Sun. Chiral effect at protein/graphene interface: A bioinspired perspective to understand amyloid formation. *Journal of the American Chemical Society*, 136(30):10736–10742, 2014.

[158] Tiziana Svaldo-Lanero, Amanda Penco, Mirko Prato, Chiara Toccafondi, Maurizio Canepa, Ranieri Rolandi, and Ornella Cavalleri. Aligning amyloid-like fibrils on nanopatterned graphite. *BioNanoScience*, 2012.

[159] X.-B. Mao, C.-X. Wang, X.-K. Wu, X.-J. Ma, L. Liu, L. Zhang, L. Niu, Y.-Y. Guo, D.-H. Li, Y.-L. Yang, and C. Wang. Beta structure motifs of islet amyloid polypeptides identified through surface-mediated assemblies. *Proceedings of the National Academy of Sciences*, 108(49):19605–19610, 2011.

[160] Shelley A. Claridge, John C. Thomas, Miles A. Silverman, Jeffrey J. Schwartz, Yanlian Yang, Chen Wang, and Paul S. Weiss. Differentiating amino acid residues and side chain orientations in peptides using scanning tunneling microscopy. *Journal of the American Chemical Society*, 135(49):18528–18535, 2013.

[161] T. Kowalewski and D. M. Holtzman. In situ atomic force microscopy study of Alzheimer's -amyloid peptide on different substrates: New insights into mechanism of -sheet formation. *Proceedings of the National Academy of Sciences*, 96(7):3688–3693, 1999.

[162] B. Cappella and G. Dietler. Force-distance curves by atomic force microscopy. *Surface Science Reports*, 34(1-3):1–104, 1999.

[163] Michael Rodahl, Fredrik Höök, Anatol Krozer, Peter Brzezinski, and Bengt Kasemo. Quartz crystal microbalance setup for frequency and Q-factor measurements in gaseous and liquid environments. *Review of Scientific Instruments*, 66(7):3924–3930, 1995.

[164] Steve S. Kim, Zhifeng Kuang, Yen H. Ngo, Barry L. Farmer, and Rajesh R. Naik. Biotic-abiotic interactions: Factors that influence peptide-graphene interactions. *ACS Applied Materials and Interfaces*, 7(36):20447–20453, 2015.

[165] F. Hook, M. Rodahl, P. Brzezinski, and B. Kasemo. Energy dissipation kinetics for protein and antibody-antigen adsorption under shear oscillation on a quartz crystal microbalance. *Doktorsavhandlingar vid Chalmers Tekniska Hogskola*, 14(1356):729–734, 1997.

[166] Gabor A. Somorjai. Modern Surface Science and Surface Technologies: An Introduction. *Chemical Reviews*, 96(4):1223–1236, 1996.

[167] Samuel Krimm and Jagdeesh Bandekar. Vibrational spectroscopy and conformation of peptides, polypeptides, and proteins. *Advances in Protein Chemistry*, 38(C):181–364, 1986.

[168] Aerial N. Camden, Stephen A. Barr, and Rajiv J. Berry. Simulations of peptide-graphene interactions in explicit water. *The Journal of Physical Chemistry B*, 117(37):10691–10697, 2013. PMID: 23964693.

[169] D. A. C. Beck, D. O. V. Alonso, D. Inoyama, and V. Daggett. The intrinsic conformational propensities of the 20 naturally occurring amino acids and reflection of these propensities in proteins. *Proceedings of the National Academy of Sciences*, 105(34):12259–12264, 2008.

[170] Direct force field 7.0, 2011.

[171] Susana M. Tomasio and Tiffany R. Walsh. Modeling the binding affinity of peptides for graphitic surfaces. influences of aromatic content and interfacial shape. *Journal of Physical Chemistry C*, 113(20):8778–8785, 2009.

[172] R. B. Pandey, Zhifeng Kuang, B. L. Farmer, Steve S. Kim, and Rajesh R. Naik. Stability of peptide (P1 and P2) binding to a graphene sheet via an all-atom to all-residue coarse-grained approach. *Soft Matter*, 8(35):9101–9109, 2012.

[173] Koji Hukushima, Hajime Takayama, and Koji Nemoto. Application of an Extended Ensemble Method To Spin Glasses. *International Journal of Modern Physics C*, 07(03):337–344, 1996.

[174] Robert H. Swendsen and Jian Sheng Wang. Replica Monte Carlo simulation of spin-glasses. *Physical Review Letters*, 57(21):2607–2609, 1986.

[175] P. Liu, B. Kim, R. A. Friesner, and B. J. Berne. Replica exchange with solute tempering: A method for sampling biological systems in explicit water. *Proceedings of the National Academy of Sciences*, 102(39):13749–13754, 2005.

[176] R. B. Pandey, Hendrik Heinz, Jie Feng, Barry L. Farmer, Joseph M. Slocik, Lawrence F. Drummy, and Rajesh R. Naik. Adsorption of peptides (A3, Flg, Pd2, Pd4) on gold and palladium surfaces by a coarse-grained Monte Carlo simulation. *Physical Chemistry Chemical Physics*, 11(12):1989–2001, 2009.

[177] Yue Shi, Zhen Xia, Jiajing Zhang, Robert Best, Chuanjie Wu, Jay W. Ponder, and Pengyu Ren. Polarizable atomic multipole-based amoeba force field for proteins. *Journal of Chemical Theory and Computation*, 9(9):4046–4063, 2013. PMID: 24163642.

[178] Mads Brandbyge, José-Luis Mozos, Pablo Ordejón, Jeremy Taylor, and Kurt Stokbro. Density-functional method for nonequilibrium electron transport. *Phys. Rev. B*, 65:165401, Mar 2002.

[179] M. Elstner, D. Porezag, G. Jungnickel, J. Elsner, M. Haugk, and Th Frauenheim. Self-consistent-charge density-functional tight-binding method for simulations of complex materials properties. *Physical Review B - Condensed Matter and Materials Physics*, 58(11):7260–7268, 1998.

[180] Zhiting Li, Yongjin Wang, Andrew Kozbial, Ganesh Shenoy, Feng Zhou, Rebecca McGinley, Patrick Ireland, Brittni Morganstein, Alyssa Kunkel, Sumedh P. Surwade, Lei Li, and Haitao Liu. Effect of airborne contaminants on the wettability of supported graphene and graphite. *Nature Materials*, 12(10):925–931, 2013.

[181] James D. Harper, Stanislaus S. Wong, Charles M. Lieber, and Peter T. Lansbury. Assembly of Aβ amyloid protofibrils: An in vitro model for a possible early event in Alzheimer's disease. *Biochemistry*, 38(28):8972–8980, 1999.

[182] Peter T. Lansbury. A Reductionist View of Alzheimer's Disease. *Accounts of Chemical Research*, 29(7):317–321, 1996.

[183] James D. Harper, Stanislaus S. Wong, Charles M. Lieber, and Peter T. Lansbury. Observation of metastable Aβ amyloid protofibrils by atomic force microscopy. *Chemistry and Biology*, 4(2):119–125, 1997.

[184] Na Li, Hyunbum Jang, Ming Yuan, Wanrong Li, Xiaolin Yun, Joon Lee, Qiqige Du, Ruth Nussinov, Jiahua Hou, Ratnesh Lal, and Feng Zhang. Graphite-Templated Amyloid Nanostructures Formed by a Potential Pentapeptide Inhibitor for Alzheimer's Disease: A Combined Study of Real-Time Atomic Force Microscopy and Molecular Dynamics Simulations. *Langmuir*, 33(27):6647–6656, 2017.

[185] Guobao Zhang, Michael J. Leibowitz, Patrick J. Sinko, and Stanley Stein. Multiple-peptide conjugates for binding β-amyloid plaques of Alzheimer's disease. *Bioconjugate Chemistry*, 14(1):86–92, 2003.

[186] Qiqige Du, Bin Dai, Jiahua Hou, Jun Hu, Feng Zhang, and Yi Zhang. A comparative study on the self-assembly of an amyloid-like peptide at water-solid interfaces and in bulk solutions. *Microscopy Research and Technique*, 78(5):375–381, 2015.

[187] Tomasz Kowalewski and David M Holtzman. 10. In situ atomic force microscopy study of Alzheimer's β-amyloid peptide on different substrates. New insights into mechanism of β-sheet formation.pdf. Technical report, 1999.

[188] Árpád Karsai, László Grama, Ünige Murvai, Katalin Soós, Botond Penke, and Miklós S.Z. Kellermayer. Potassium-dependent oriented growth of amyloid β25-35 fibrils on mica. *Nanotechnology*, 18(34):7, 2007.

[189] M. S. Z. Kellermayer, A. Karsai, M. Benke, K. Soos, and B. Penke. Stepwise dynamics of epitaxially growing single amyloid fibrils. *Proceedings of the National Academy of Sciences*, 105(1):141–144, 2008.

[190] Eleanor K. Johnson, Lin Chen, Peter S. Kubiak, Shane F. McDonald, Dave J. Adams, and Petra J. Cameron. Surface nucleated growth of dipeptide fibres. *Chemical Communications*, 49(77):8698–8700, 2013.

[191] Yun Liu, Xiao Ding Xu, Jing Xiao Chen, Han Cheng, Xian Zheng Zhang, and Ren Xi Zhuo. Surface self-assembly of N-fluorenyl-9-methoxycarbonyl diphenylalanine on silica wafer. *Colloids and Surfaces B: Biointerfaces*, 87(1):192–197, 2011.

[192] Takakazu Seki, Christopher R. So, Tamon R. Page, David Starkebaum, Yuhei Hayamizu, and Mehmet Sarikaya. Electrochemical Control of Peptide Self-Organization on Atomically Flat Solid Surfaces: A Case Study with Graphite. *Langmuir*, 34(5):1819–1826, 2018.

[193] Lihi Adler-Abramovich, Daniel Aronov, Peter Beker, Maya Yevnin, Shiri Stempler, Ludmila Buzhansky, Gil Rosenman, and Ehud Gazit. Self-assembled arrays of peptide nanotubes by vapour deposition. *Nature Nanotechnology*, 4(12):849–854, 2009.

[194] Peter S. Kubiak, Salmah Awhida, Christopher Hotchen, Wentao Deng, Ben Alston, Tom O. McDonald, Dave J. Adams, and Petra J. Cameron. Polymerization of low molecular weight hydrogelators to form electrochromic polymers. *Chemical Communications*, 51(52):10427–10430, 2015.

[195] Lihi Adler-Abramovich and Ehud Gazit. Correction: The physical properties of supramolecular peptide assemblies: from building block association to technological applications. *Chemical Society reviews*, 43(20):7236, 2014.

[196] Jean Luc Ravanat. Measuring oxidized DNA lesions as biomarkers of oxidative stress: An analytical challenge. *Fabad Journal of Pharmaceutical Sciences*, 30(2):100–113, 2005.

[197] Kevin M. Eckes, Kiheon Baek, and Laura J. Suggs. Design and Evaluation of Short Self-Assembling Depsipeptides as Bioactive and Biodegradable Hydrogels. *ACS Omega*, 3(2):1635–1644, 2018.

[198] Assaf Mahler, Meital Reches, Meirav Rechter, Smadar Cohen, and Ehud Gazit. Rigid, self-assembled hydrogel composed of a modified aromatic dipeptide. *Advanced Materials*, 18(11):1365–1370, 2006.

[199] Ron Orbach, Iris Mironi-Harpaz, Lihi Adler-Abramovich, Estelle Mossou, Edward P. Mitchell, V. Trevor Forsyth, Ehud Gazit, and Dror Seliktar. The rheological and structural properties of Fmoc-peptide-based hydrogels: The effect of aromatic molecular architecture on self-assembly and physical characteristics. *Langmuir*, 28(4):2015–2022, 2012.

[200] Meital Reches and Ehud Gazit. Self-assembly of peptide nanotubes and amyloid-like structures by charged-termini-capped diphenylalanine peptide analogues. *Israel Journal of Chemistry*, 45(3):363–371, 2005.

[201] Yifei Zhang, Xiaojing Liu, Mengfan Wang, Yanan Zhao, Wei Qi, Rongxin Su, and Zhimin He. Co-assembly of Fmoc-tripeptide and gold nanoparticles as a facile approach to immobilize nanocatalysts. *RSC Advances*, 7(26):15736–15741, 2017.

[202] Ohad Carny, Deborah E. Shalev, and Ehud Gazit. Fabrication of coaxial metal nanocables using a self-assembled peptide nanotube scaffold. *Nano Letters*, 6(8):1594–1597, 2006.

[203] Sivoney F. Souza, Sergio Kogikoski, Emerson R. Silva, and Wendel A. Alves. Nanostructured antigen-responsive hydrogels based on peptides for leishmaniasis detection. *Journal of the Brazilian Chemical Society*, 28(9):1619–1629, 2017.

[204] Mi Zhou, Andrew M. Smith, Apurba K. Das, Nigel W. Hodson, Richard F. Collins, Rein V. Ulijn, and Julie E. Gough. Self-assembled peptide-based hydrogels as scaffolds for anchorage-dependent cells. *Biomaterials*, 30(13):2523–2530, 2009.

[205] Yung Li Wang, Shih Pei Lin, Srinivasa Rao Nelli, Fu Kai Zhan, Hsun Cheng, Tsung Sheng Lai, Mei Yu Yeh, Hsin Chieh Lin, and Shih Chieh Hung. Self-Assembled Peptide-Based Hydrogels as Scaffolds for Proliferation and Multi-Differentiation of Mesenchymal Stem Cells. *Macromolecular Bioscience*, 17(4):13, 2017.

[206] Amanda N. Moore and Jeffrey D. Hartgerink. Self-Assembling Multidomain Peptide Nanofibers for Delivery of Bioactive Molecules and Tissue Regeneration. *Accounts of Chemical Research*, 50(4):714–722, 2017.

[207] Ruirui Xing, Shukun Li, Ning Zhang, Guizhi Shen, Helmuth Möhwald, and Xuehai Yan. Self-Assembled Injectable Peptide Hydrogels Capable of Triggering Antitumor Immune Response. *Biomacromolecules*, 18(11):3514–3523, 2017.

[208] Helmut Cölfen and Stephen Mann. Higher-order organization by mesoscale self-assembly and transformation of hybrid nanostructures. *Angewandte Chemie - International Edition*, 42(21):2350–2365, 2003.

[209] Xiaohong An, Trevor Simmons, Rakesh Shah, Christopher Wolfe, Kim M. Lewis, Morris Washington, Saroj K. Nayak, Saikat Talapatra, and Swastik Kar. Stable aqueous dispersions of noncovalently functionalized graphene from graphite and their multifunctional high-performance applications. *Nano Letters*, 10(11):4295–4301, 2010.

A. CHAPTER 1 SUPPLEMENTARY INFORMATION

A version of this appendix was previously published as Supplementary Information in *Chemistry of Materials*.
DOI: 10.1021/acs.chemmater.7b04434

A.1 AFM images of lamellar and domain structure in PCDA samples prepared by drop-casting

While Chapter 1 largely discusses monolayers of PCDA prepared by Langmuir-Schaefer transfer, similar ordered structures can be prepared by assembly from organic solvents. Figure A.1 shows a representative SEM image of a PCDA monolayer assembled from organic solvent and a Langmuir-Schaefer film that presented a similar degree of coverage as visualized by SEM. Briefly, a clean CVD graphene on nickel substrate was suspended from a mechanical dip head and lowered to touch the surface of a 0.017 mg/mL solution of PCDA in 3:2 (v:v) hexane:isopropanol for ∼1 min. The substrate was then blown dry with N_2 and analyzed by PM-IRRAS and SEM.

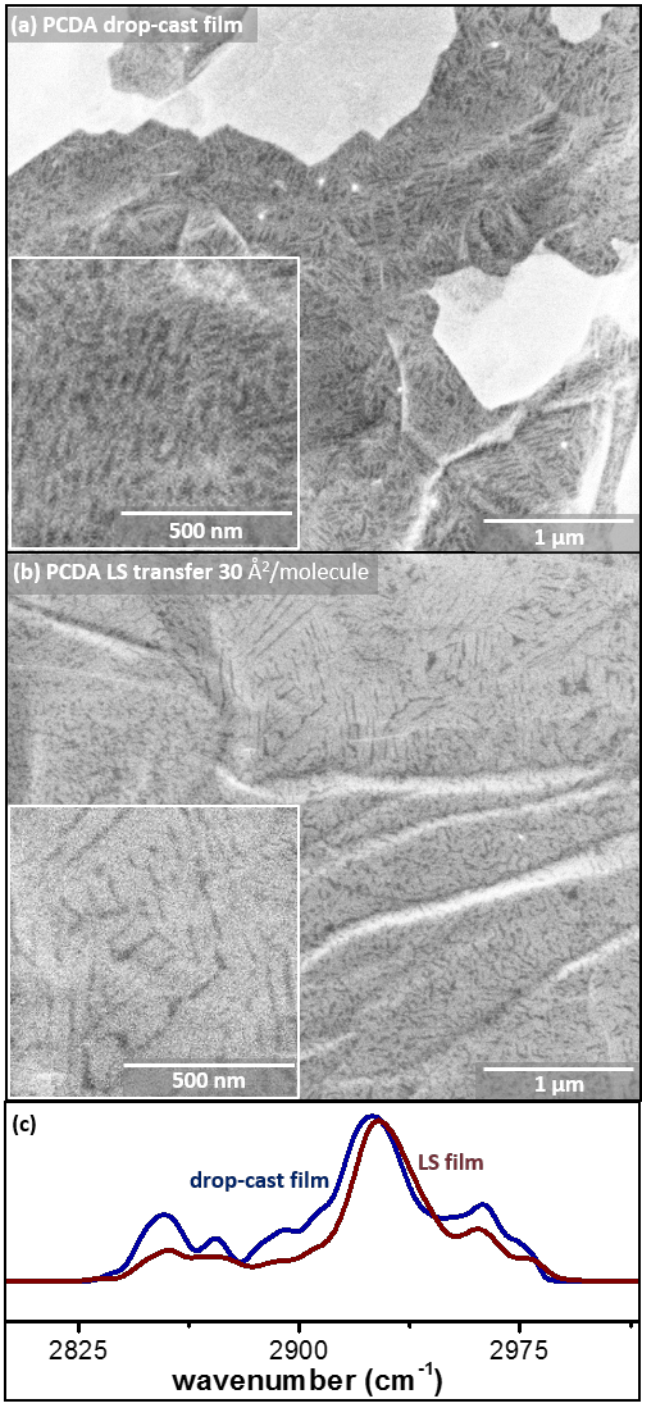

Figure A.1.: SEM images of PCDA assembled on graphene assembled (a) from solution in 3:2 hexane:isopropanol and (b) by LS transfer. (c) PM-IRRAS spectra for drop-cast and LS films

SEM images of monolayers produced by assembly from solution (Figure A.1a) are qualitatively similar to those produced via Langmuir-Schaefer transfer (see Figure A.1b and main manuscript), exhibiting large areas of monolayer coverage. Domains produced by the solution assembly procedure are quite small (visible in the SEM image), consistent with very rapid assembly, and exhibit small bright spots, which typically correspond to molecular aggregates or standing phase molecules. Although $I(CH_{2a})$ for the film shown (Figure A.1c, blue trace) is similar to that in a typical high-coverage film prepared through LS transfer (Figure A.2c, red trace), the ratio $I(CH_{2a})/I(CH_{3a})$ for the drop-cast film (2.67) is somewhat lower than that for the LS film (3.19). The CH_{2s} peak in the solution-assembled film spectrum is also somewhat higher relative to the CH_{2a} peak; increased alignment of CH_{2s} dipoles normal to the interface could be consistent with either a lying-down conformation in which the alkyl backbone zig-zags perpendicular to the surface, or to the formation of modest amounts of standing phase.

To illustrate why we typically utilize LS transfer for preparation of monolayers of this type, we show SEM images of a PCDA monolayer prepared by drop-casting from a 0.075 mg/mL solution of PCDA in 1:1 (v/v) hexane:isopropanol onto a heated HOPG substrate (Figure A.2). This procedure has been used previously by others and by us to prepare large ordered monolayer domains for scanning probe imaging. However, because heating results in solvent evaporation as the drop withdraws across the substrate, concentration changes can lead to substantial variations in PCDA domain size and assembled morphology across the substrate. At the top of the substrate, small domains and vacancies are observed (Figure A.2d), with increases in domain size and eventual formation of multilayers in the middle (Figure A.2e) and at the bottom of the substrate (Figure A.2f) as solute concentrations increase.

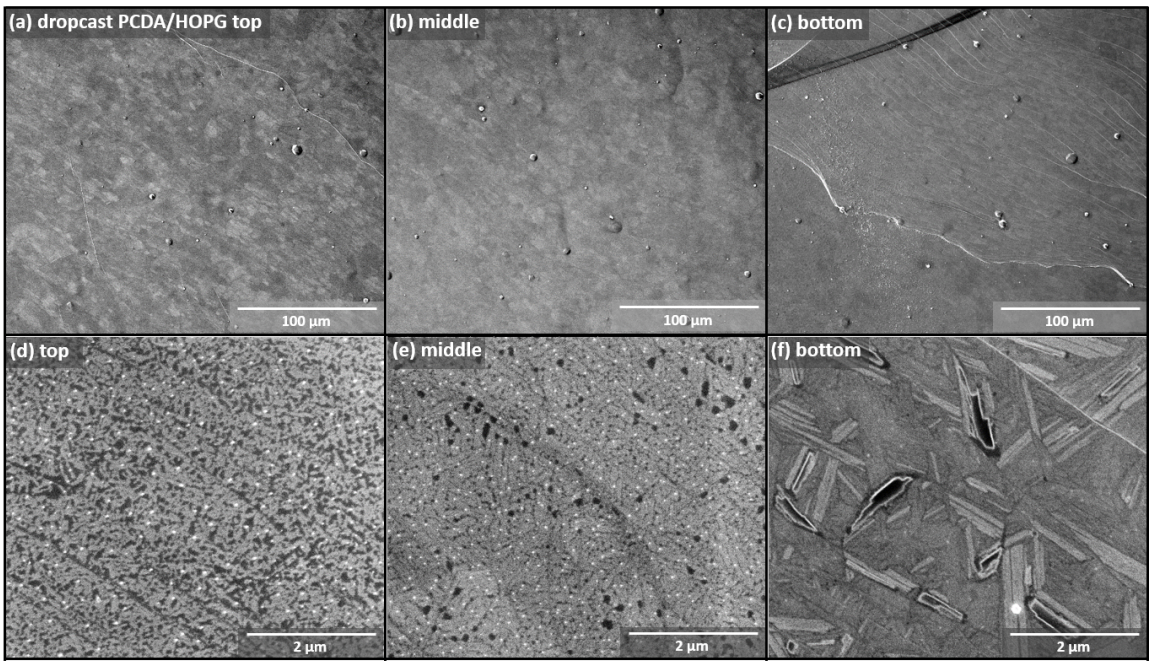

Figure A.2.: Large scale (a-c) and higher-resolution (d-f) SEM images of drop-cast PCDA at top (a,d), middle (b,e) and bottom (c,f) of the HOPG substrate.

A.2 Representative AFM image of PCDA on HOPG, quantifying domain heights

Figure A.3a shows a typical arrangement of PCDA domains corresponding to an ordered, lying down phase on HOPG. Line profiles (Figure A.3b) collected along the domain edges measure average height changes of 0.43 ± 0.02 nm, consistent with the expected height of a lying down monolayer of PCDA.

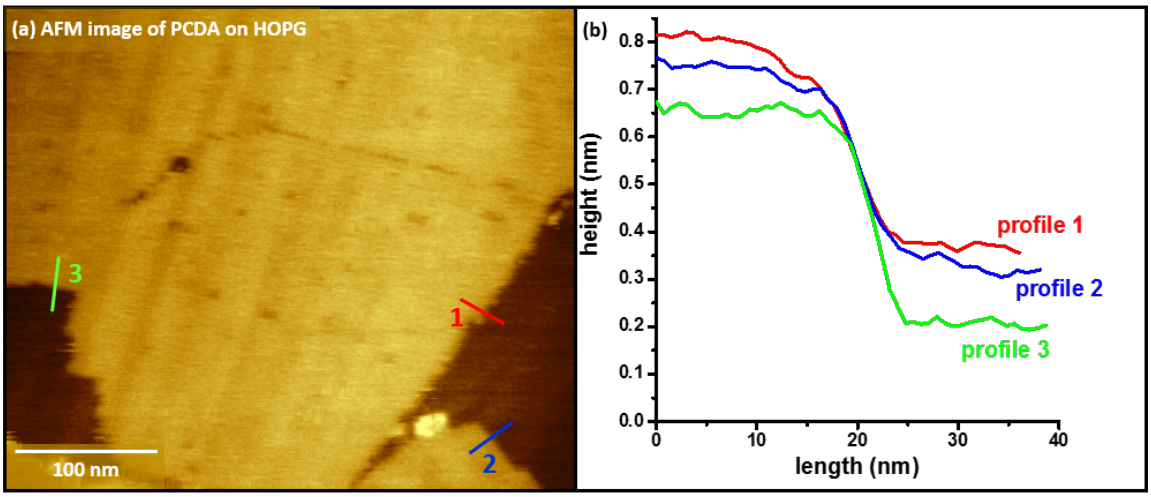

Figure A.3.: (a) AFM image of PCDA transferred to HOPG via LS conversion with three domain edges highlighted with colored lines. (b) Line profiles corresponding to the colored lines in (a).

A.3 Large-scale SEM images of PCDA on CVD graphene and HOPG

Figure A.4 compares surface topography of CVD graphene on nickel and HOPG substrates that have been utilized for transfer of PCDA films. Substantially rougher CVD graphene surfaces raise challenges for scanning probe characterization over large scales, as illustrated in the main text (Figure A.3).

Figure A.5 illustrates that although the topography of the CVD graphene is a significant contributor to image contrast (e.g. white features in the large scale image in the upper left corner), lying-down PCDA monolayer domain structure is also frequently visible in images acquired at this scale, when sufficiently enlarged. When the area highlighted in yellow is enlarged to full page width, polymerization-induced cracking defects in the monolayer (closely-spaced linear features in center of image) reveal the presence of large ordered molecular domains, as well as the directionality of the lamellar axis in each domain.

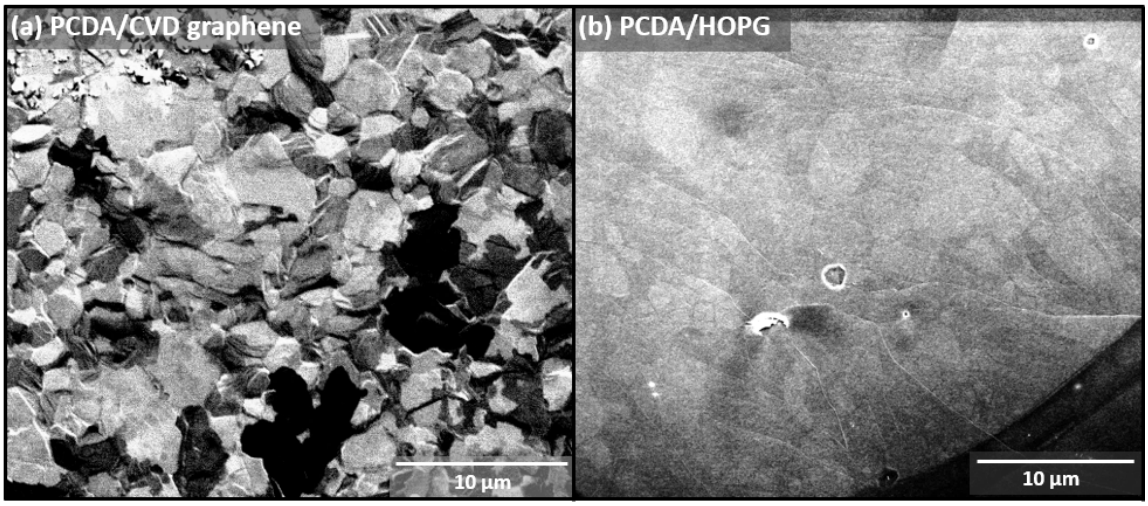

Figure A.4.: SEM images showing surface topography of (a) graphene and (b) HOPG substrates to illustrate difference in surface topography over large scales.

PCDA molecular ordering is typically assessed using images acquired at scales similar to those shown in Figure A.6. Evaluation of local domain structure is most accurate at scales similar to that shown in Figure A.6b; comparison with scales similar to that shown in Figure A.6a ensure representative areas are selected. In the images shown, the brightest features are topographically elevated areas of the graphene substrate. In Figure A.6b, mid and darker grey tones are graphene with partial coverage of PCDA, which exhibits a low degree of molecular order under the illustrated transfer conditions (50 $Å^2$/molecule, 20 °C), assessed both by the irregular domain shapes and lack of polymerization-induced cracking defects of the type visible in Figure A.5. Continuations of the amorphous domain structure are visible on the brighter terraces with close inspection.

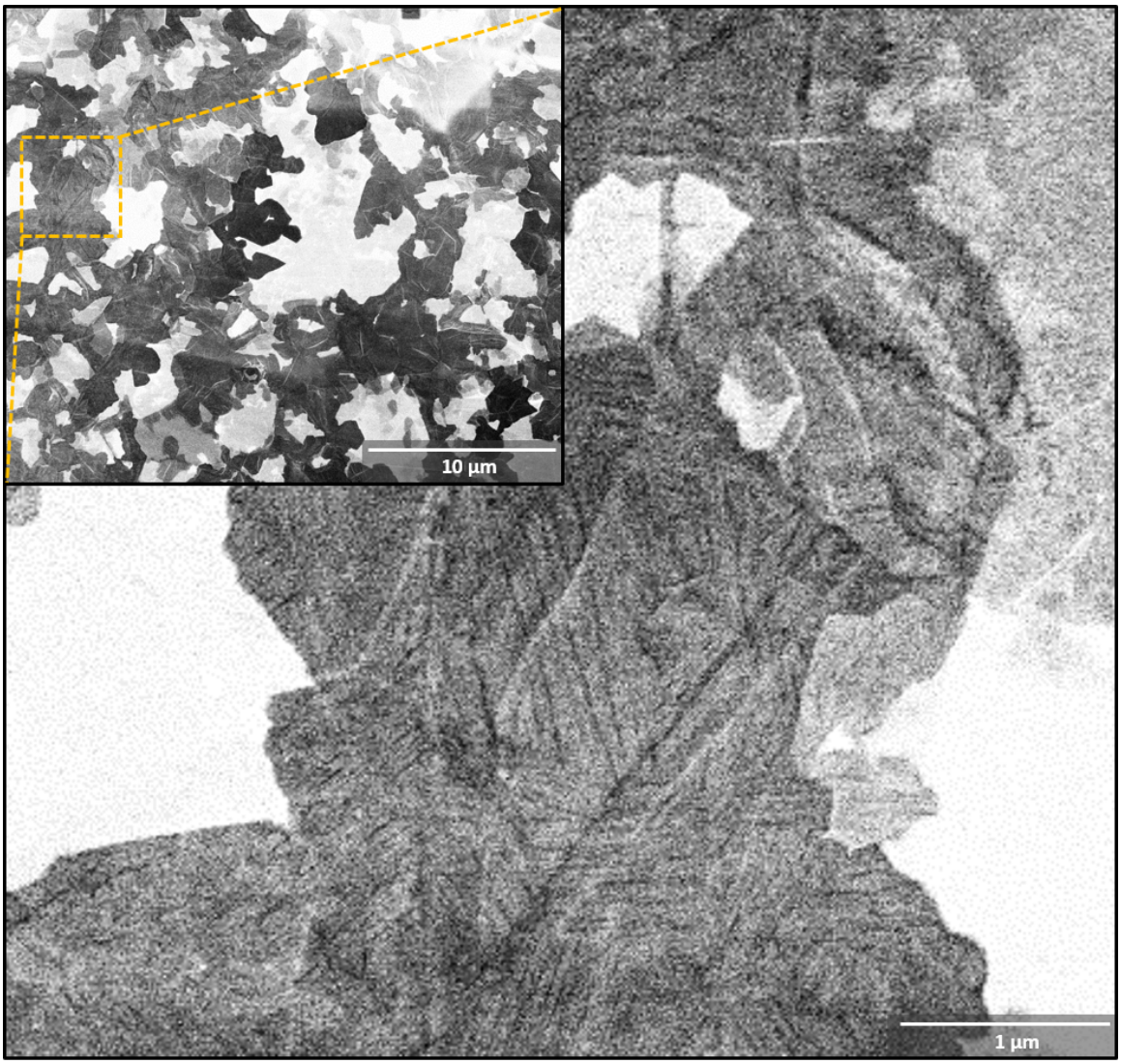

Figure A.5.: SEM image of PCDA domain structure on graphene. Image shown at full page width is area highlighted in yellow, cropped and enlarged to show detail.

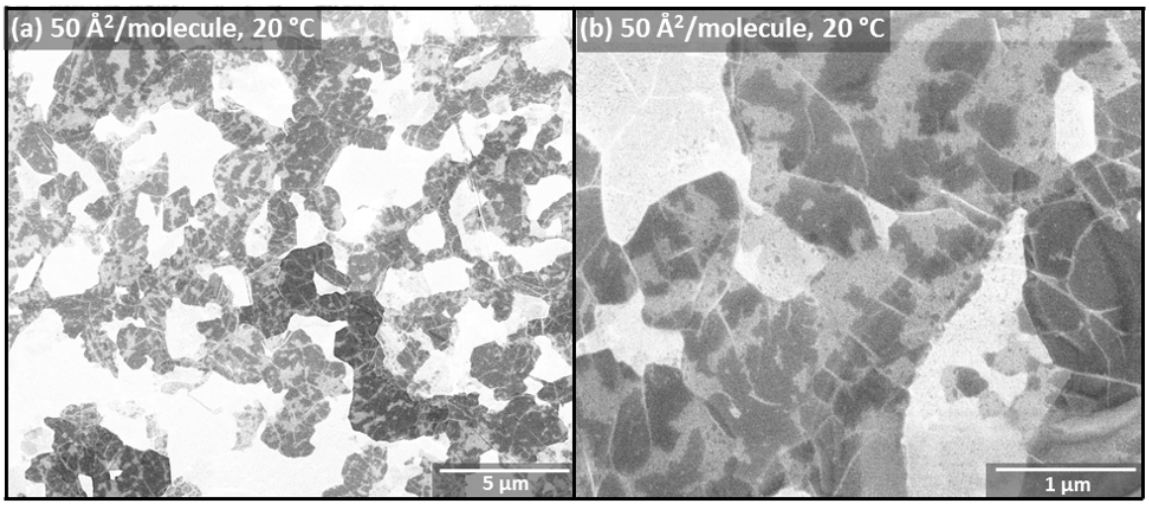

Figure A.6.: SEM images of PCDA domain structure on graphene, from a substrate illustrating partial, disordered coverage after transfer at 50 Å^2/molecule and 20 °C.

A.4 $\mathbf{I(CH_{2a})/I(CH_{2s})}$ vs. $\mathbf{I_{total}(CH)}$

Signal intensity in the C-H stretch region arises from a convolution of surface coverage and molecular ordering. To assess relative contributions from surface coverage and ordering, we compared the total intensity in the C-H stretch region with the intensity ratio $I(CH_{2a})/I(CH_{2s})$, which would be expected to increase with monolayer ordering, but not with (disordered) coverage (Figure A.7). Surface coverage was assessed based on SEM images. Surfaces with full monolayer coverage visible in SEM images typically exhibit total C-H stretch intensities ≥ 2.5. For transfer at $T_{sp} = 30$ °C, samples with greater values of total intensity exhibit increasing degrees of order, as measured by $I(CH_{2a})/I(CH_{2s})$, and the appearance of polymerization induced cracking in SEM images. For transfer at $T_{sp} = 20$ °C, one cluster of samples (transferred at mma > 25 Å^2/molecule) exhibited $I_{total} \leq 2$,with $I(CH_{2a})/I(CH_{2s}) < 4.5$. A second cluster of samples (transferred at mma ≤ 25 Å^2/molecule) contained 3D PCDA rods, and exhibited $I_{total} > 2.5$ and $I(CH_{2a})/I(CH_{2s}) > 5$.

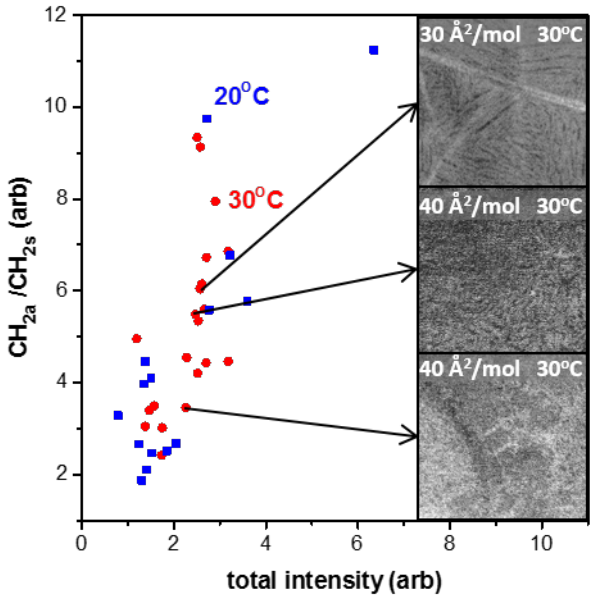

Figure A.7.: CH_{2a}/CH_{2s} ratio versus the total intensity of the C-H stretch region. SEM images are representative of samples at indicated points.

A.5 SEM images used to show correlation between PM-IRRAS signal intensity and monolayer ordering

In the manuscript, small SEM images are used to illustrate ordered amorphous domains and vacancies in disordered PCDA monolayers; here, images are shown at large scale in Figure A.8 for comparison.

Rod-like features in Figure A.8a appear to be small 3D crystals of PCDA. Saturated (white pixel values) visible in most images are terraces with different numbers of graphene layers.

Figure A.9 shows SEM images acquired from PCDA films transferred at larger values of mma, in which molecular domains exhibit a lower degree of order, as indicated by irregular domain shapes and the lack of polymerization-induced cracking defects.

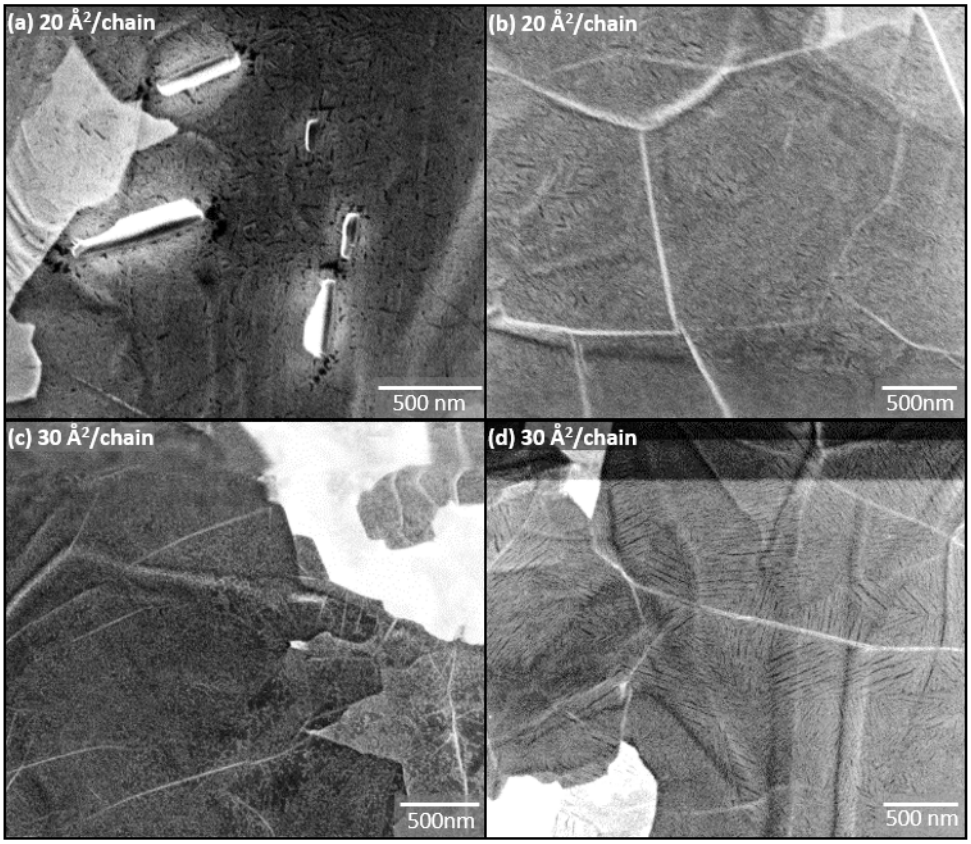

Figure A.8.: SEM images showing domain structures for PCDA monolayers transferred at: (a) 20 $Å^2$/molecule, 20 °C, (b) 20 $Å^2$/molecule, 30 °C, (c) 30 $Å^2$/molecule, 20 °C, and (d) 30 $Å^2$/molecule, 30 °C.

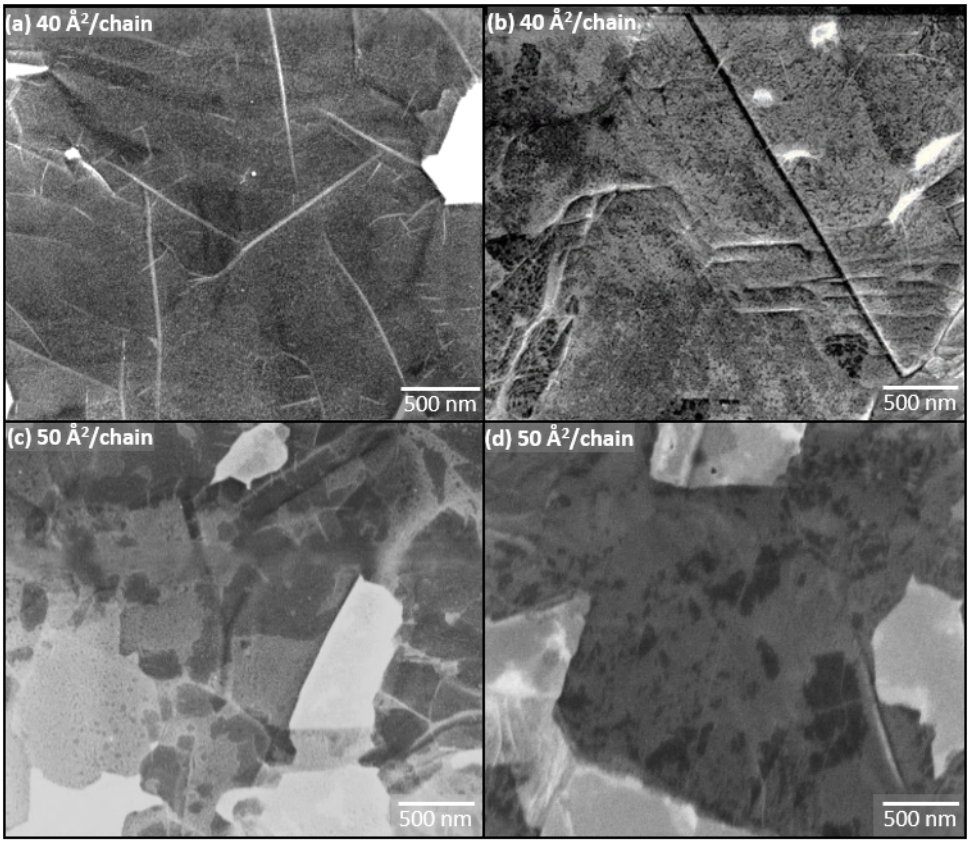

Figure A.9.: SEM images showing domain structures for PCDA monolayers transferred at: (a) 40 Å^2/molecule, 20 °C, (b) 40 Å^2/molecule, 30 °C, (c) 50 Å^2/molecule, 20 °C, and (d) 50 Å^2/molecule, 30 °C.

A.6 CH_{2a} peak frequencies as a function of $I(CH_{2a})/I(CH_{3a})$

To determine whether frequency maxima of CH_{2a} peaks shifted based on increasing monolayer order, these values were plotted against the ordering parameter $I(CH_{2a})/I(CH_{3a})$ for all of the substrates investigated. Figure A.10 illustrates that there is not a clear relationship between the CH_{2a} peak frequency and the degree of ordering in the PCDA monolayer.

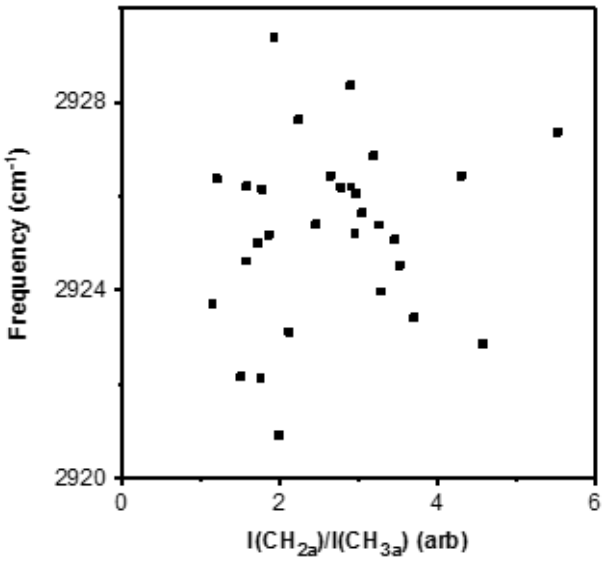

Figure A.10.: Frequency of the CH_{2a} peak plotted against $I(CH_{2a})/I(CH_{3a})$.

A.7 Larger versions of SEM images presented in Figure A.10cf

SEM images shown as insets in Figure A.10cf are reproduced here at larger size (Figure A.11ad) to show detail present in original image.

A.8 SEM images of transferred noncovalent film without diyne

SEM images of transferred molecular layers that lack the polymerizable diyne can be used to assess coverage on 2D materials. The images below (Figure A.12a-d) were acquired from a molecular film of pentacosanoic acid (PCA), which has the same chain length and headgroup structure as the 10,12-PCDA used throughout the manuscript, but lacks the internal diyne. Here, a series of insets reveal the edge of a transferred island structure, showing multiple levels of contrast, which could potentially be quantified as part of a molecular ordering assessment similar to those carried out in the manuscript.

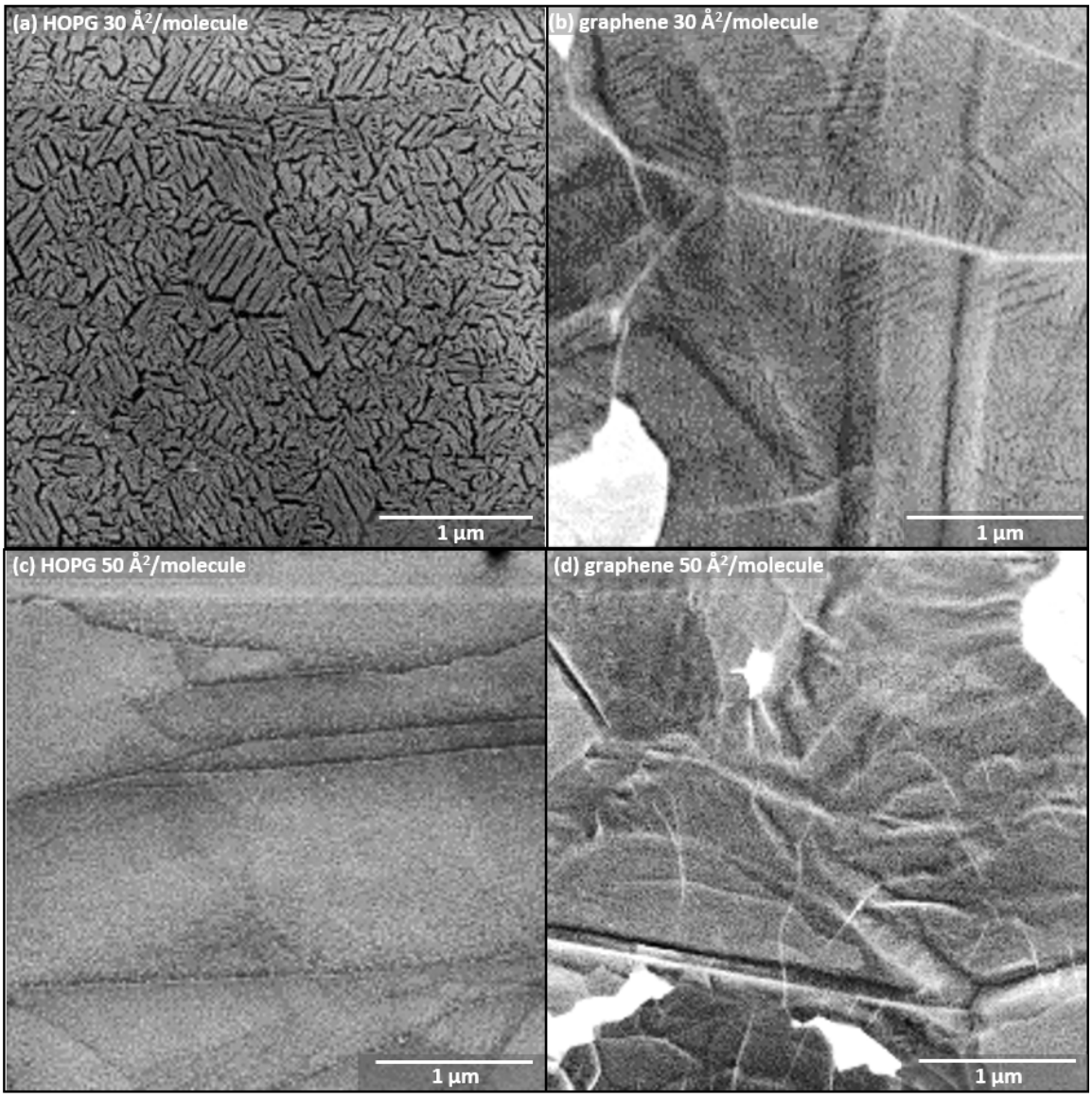

Figure A.11.: SEM images showing ordered domain structure on (a) HOPG and (b) graphene, as well as disordered structure on (c) HOPG and (d) graphene.

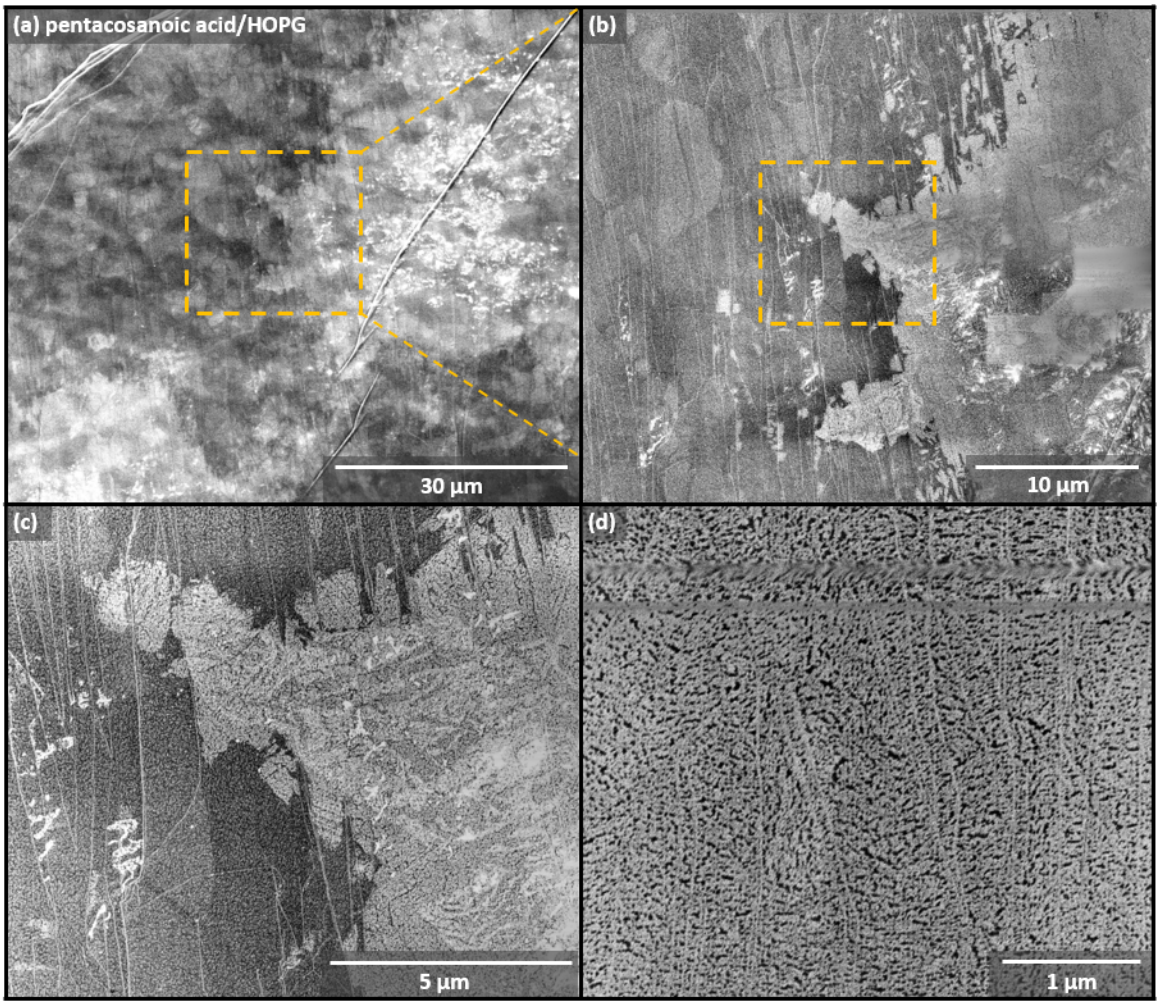

Figure A.12.: SEM images of non-polymerizable long-chain carboxylic acid PCA, with scale bars of (a) 30 μm, (b) 10 μm, (c) 5 μm, and (d) 1 μm.

A.9 Quantitative comparison of I(CH_{2a})/I(CH_{3a}) with lamellar surface coverage in SEM images

Spectral metrics were assessed by comparing the PM-IRRAS data (red) for PCDA assembled on HOPG substrates with monolayer coverage and ordering data for films transferred from Langmuir films with the same mean molecular areas (mma) and the same subphase temperature (30 °C) in a previous study [38] (blue) (Figure A.13). At a given mean molecular area, the fractional coverage of ordered lamellar phases ($\chi_{lamellar}$), amorphous phases ($\chi_{amorphous}$), vacancies ($\chi_{vacancy}$), and standing phases ($\chi_{standing}$) was tabulated based on digital segmentation of large SEM images. Spectral data in Figure A.13 are normalized to 100% for the highest measured ratio.

Figure A.13a plots the total percent surface coverage ($\chi_{total} = \chi_{lamellar} + \chi_{amorphous}$, for samples that lack standing phases) of PCDA on HOPG in blue. I(CH_{2a}), plotted in red on the same graph, varies similarly. This is reasonable given the relatively high values of $\chi_{lamellar}$, and the fact that even areas of the monolayer that are not ordered enough to polymerize are likely to express a net preference for the CH_{2a} dipole to orient normal or nearly normal to the substrate as illustrated in Figure 1.5b.

Figure A.13b compares the fraction of ordered surface coverage ($\chi_{ordered} = \chi_{lamellar}/(\chi_{lamellar} + \chi_{amorphous})$) measured from SEM images (blue trace) with the spectral metric I(CH_{2a})/I(CH_{3a}) (red trace), which is also intended to normalize ordered surface coverage against total surface coverage. Again the measurements are in reasonable agreement, except for films transferred at 90 and 100 Å^2/molecule. We note that in the previous SEM image analysis, we also quantified polymerization-induced cracking in ordered domains, and found only half as much cracking in polymerizable domains transferred at large mma values in comparison with high mma value. This suggests the likelihood of slightly lower levels of ordering in such domains. Thus, it is possible that the lower values of I(CH_{2a})/I(CH_{3a}) at high mma at least in part reflects this difference. Overall, these findings point to the quantitative

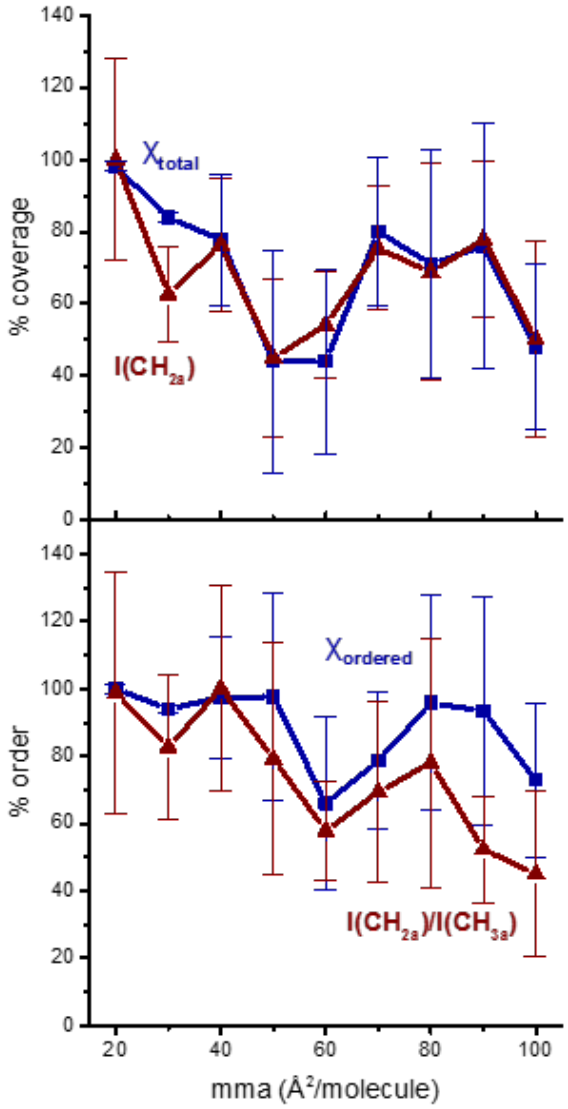

Figure A.13.: (a) Comparison of $I(CH_{2a})$ and SEM image analysis of monolayer coverage and (b) comparison of $I(CH_{2a})/I(CH_{3a})$ and SEM image analysis of monolayer order.

relationship between $I(CH_{2a})$, $I(CH_{2a})/I(CH_{3a})$, and PCDA coverage and ordering on graphitic interfaces.

PUBLICATION

CHEMISTRY OF MATERIALS
Cite This: *Chem. Mater.* 2018, 30, 2506−2514
Article
pubs.acs.org/cm

Spectroscopic Metrics for Alkyl Chain Ordering in Lying-Down Noncovalent Monolayers of Diynoic Acids on Graphene

Shane R. Russell,[†] Tyson C. Davis,[†] Jae Jin Bang,[†] and Shelley A. Claridge*[,†,‡]

[†]Department of Chemistry, Purdue University, West Lafayette, Indiana 47907, United States
[‡]Weldon School of Biomedical Engineering, Purdue University, West Lafayette, Indiana 47907, United States

Supporting Information

ABSTRACT: Noncovalent monolayer chemistries are widely used to control physical properties of 2D materials. For many applications (e.g., energy conversion, sensing), molecular ordering across a range of length scales is important in determining the physical properties of the interface. Scanning probe microscopy can resolve details of molecular packing and orientation over nanoscopic areas of graphene, graphite, and other 2D materials; however, evaluating molecular ordering over larger scales is also key. Such ordering is especially challenging to characterize at large scales for lying-down phases (thickness <0.5 nm) on topographically rougher materials such as graphene (vs flatter graphite). Here, we combine scanning electron microscopy and polarization-modulated IR reflection absorption spectroscopy to evaluate alkyl chain ordering in lying-down monolayers of diynoic acids on few-layer graphene and graphite substrates with areas ∼1 cm^2. The ability to assess ordering in this widely used class of molecules reinforces the potential utility of spectroscopic metrics for evaluating structure in noncovalently functionalized 2D materials at micro- and macroscopic scales.

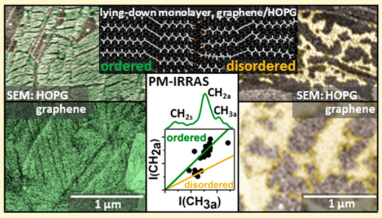

As 2D materials are integrated into hybrid architectures,[1−10] controlling their surface chemistry at large scales and throughout solution and thermal processing becomes increasingly important.[8,11−13] Layered materials such as graphene are frequently functionalized noncovalently (e.g., with lying-down phases of long-chain alkanes or polycyclic aromatic molecules) to preserve electronic conjugation within the basal plane.[1,2,14,15] However, relatively weak noncovalent interactions within the monolayer[1,2,4] increase the probability of molecular disorder, during either assembly or subsequent processing. Noncovalent monolayers have been imaged down to sub-nanometer scales using scanning probe microscopy;[16−21] however, heterogeneity is also common at micrometer and larger scales, necessitating appropriate characterization methods. Spectroscopic metrics have been developed to assess large-scale ordering in standing phase monolayers (e.g., alkanethiols on coinage metals).[22−24] Equivalent metrics for 2D materials noncovalently functionalized with lying-down phases would have potentially broad utility, but must account for differences in molecular orientation and in some cases substrate selection rules. Here, we develop spectroscopic metrics for ordering in noncovalent monolayers of diynoic acids on graphene and graphite, using polarization-modulated IR reflection adsorption spectroscopy (PM-IRRAS) correlated with scanning electron microscopy (SEM).

Diynoic amphiphiles, including long-chain carboxylic acids (e.g., 10,12-pentacosadiynoic acid, PCDA, Figure 1a), are prevalent in noncovalent functionalization of graphene,[16,25,26] highly ordered pyrolytic graphite (HOPG),[2,17,18,27,28] and other 2D materials.[29] Lying-down lamellar phases assemble due to epitaxy between the zigzag carbon skeleton of the alkyl chain and the <11$\underline{2}$0> axis of the basal plane,[17,30,31] ordering domains

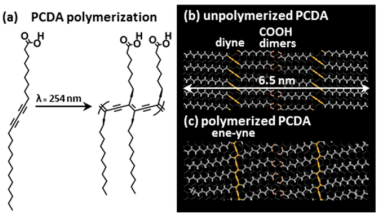

Figure 1. (a) Chemical structure of unpolymerized (left) and polymerized (right) PCDA. Molecular models of (b) unpolymerized PCDA and (c) polymerized PCDA on HOPG, illustrating lamellar width, H-bonded COOH dimers along lamellar median, and polymerization of diyne to form ene−yne.

Received: October 22, 2017
Revised: March 21, 2018
Published: April 2, 2018

DOI: 10.1021/acs.chemmater.7b04434
Chem. Mater. 2018, 30, 2506−2514

at ∼120° angles.[2,32] Molecules orient head-to-head, forming carboxylic acid dimers that stabilize the lamellar median (Figure 1b). Topochemical photopolymerization of aligned diynes produces an ene−yne polymer backbone (Figure 1a,c), which has been examined for molecular electronics applications.[16,32] Polymerization also increases monolayer robustness toward solvent exchanges or other processing.[8]

The degree of alkyl chain ordering governs many chemical properties of the assembled interface. For example, topochemical polymerization efficiency for diynes varies strongly with the distance between bond-forming carbons,[18,29] in addition to details of chain structure and packing.[33−36] We have also found that long-range ordering of diyne monolayers impacts interfacial stability after polymerization in the context of solution processing,[37] and that structure-specific headgroup dynamics (a form of controlled disordering) modulate interfacial wettability.[38] Conversely, monolayer defects can promote undesirable interfacial processes such as nonspecific adsorption and charge carrier trapping.[25,39−41] Thus, evaluating molecular ordering is central in screening for interfaces that will exhibit desired physical properties in subsequent use.

In principle, atomic force microscopy (AFM) can be used to characterize surface structure at lateral scales up to 100 μm. However, our experience suggests the upper limit for useful AFM topographic imaging of noncovalent lying-down monolayers of diynoic acids on HOPG is ∼10 μm; beyond this scale, contributions from the substrate itself typically dominate contrast.[8,12] Characterization of monolayers on more technologically interesting 2D materials such as chemical vapor deposited (CVD) graphene is further complicated by increased surface roughness (e.g., wrinkling) and the topography of the underlying support. Together, these factors make high-resolution AFM imaging of PCDA monolayers on CVD graphene at scales significantly >1 μm challenging.

We have recently observed that SEM mitigates these issues, enabling noncovalent monolayer structure on HOPG to be characterized at scales as large as millimeters and as small as tens of nanometers.[42] In the present work, we find that domain structures can be imaged on rougher CVD graphene, at scales up to 30−50 μm, enabling correlation of interfacial structure with functionalization conditions and spectral features. We have also observed previously that the SEM electron beam induces cracking in ordered, but not disordered, PCDA domains, due to conformational changes that occur when rows of ordered molecules polymerize under the electron beam. Polymerization-induced cracking can thus be used to distinguish between ordered and disordered areas in molecular films (discussed in more detail below), with implications for film quality in electronic or other applications. Repeated imaging of the same area shows that, during high-resolution SEM imaging, the electron beam also degrades the monolayers, impeding subsequent use of areas of the surface screened in this way.

Addressing this issue, we also develop a nondestructive spectroscopic probe for alkyl chain ordering in noncovalently adsorbed lying-down monolayers on graphene and HOPG. Correlating PM-IRRAS data with subsequently acquired SEM images of the same samples enables us to establish the relationship between spectral characteristics and surface structure. Surface selection rules for metallic substrates emphasize dipole components oriented in the plane of incidence (the plane defined by the surface normal and the incoming beam path);[43,44] this provides a basis for analyzing the average degree of alkyl chain ordering in monolayers of PCDA on CVD graphene on nickel substrates. Applicable to broad classes of functional molecules used in noncovalent modification of 2D materials, this approach enables nondestructive screening of interfacial ordering at scales relevant for many applications.

■ RESULTS AND DISCUSSION

Monolayer Preparation by Langmuir−Schaefer Conversion. To create surfaces with varying degrees of order, PCDA monolayers on graphene were prepared by Langmuir−Schaefer (LS) conversion of standing phase Langmuir films on an aqueous subphase (Figure 2a). Although this approach levies additional requirements on sample preparation in comparison with the more expedient drop-casting approach, we find that LS transfer improves uniformity across the entire 1 cm × 1 cm substrate (see the Supporting Information, Figure S2).

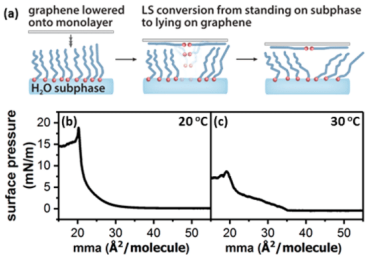

Figure 2. (a) Schematic of LS conversion of PCDA to form lying-down phase monolayers on CVD graphene or HOPG. (b, c) Surface pressure isotherms for PCDA with subphase temperatures (T_{sp}'s) of (b) 20 and (c) 30 °C.

Moving barriers compress the Langmuir film to a desired mean area available per molecule (mma). Changes in surface pressure during compression (Figure 2b,c) reveal phase transitions in the Langmuir film with increasing order, which impact molecular transfer to the graphene or HOPG. Controlling the temperature of the subphase (T_{sp}) also provides a means of modulating ordering of the Langmuir film (Figure 2b vs Figure 2c). Here, performing transfers at 20 and 30 °C facilitated comparisons with SEM data we have collected previously for transfers to HOPG under similar conditions (see the Supporting Information).

AFM and SEM Evaluation of Monolayer Ordering. AFM imaging is frequently used to evaluate ordering and domain structure in lying-down monolayers. AFM images of ordered regions of unpolymerized monolayers on HOPG and CVD graphene prepared at T_{sp} = 30 °C and mma = 30 Å^2/molecule are shown in Figure 3. For comparison, similar images from samples prepared by drop-casting are included in the Supporting Information. Larger flat terraces in an HOPG substrate (Figure 3a) contribute to clearer molecular rows than in monolayers on CVD graphene (Figure 3b). In both cases, however, lamellar domains with edge lengths >100 nm are visible, assembled in epitaxy with the graphitic basal plane with domains oriented at ∼120° angles. Already at sub-μm scales, heterogeneities in the graphene surface reduce scanning probe image quality in comparison with HOPG.

In order to examine monolayer structure over larger areas to make useful comparisons with spectroscopic data, we utilized

DOI: 10.1021/acs.chemmater.7b04434
Chem. Mater. 2018, 30, 2506−2514

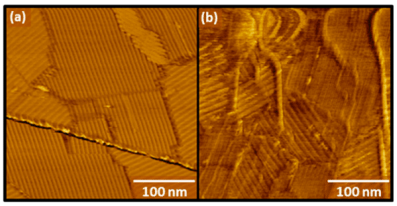

Figure 3. AFM images of PCDA assembled on (a) HOPG and (b) CVD graphene.

SEM (Figures 4 and 5). Figure 4 compares SEM images of ordered PCDA monolayers on CVD graphene (Figure 4a,b) and HOPG (Figure 4c,d). In each pair of images, the inset is the original image, and the larger image is the highlighted region, cropped and enlarged to show detail. Monolayers exhibit cracking defects characteristic of Ångstrom-scale decreases in lamellar width as the diyne rehybridizes to form the ene−yne. This behavior is consistent with previous results indicating that ordered regions of such monolayers can be polymerized by electrons in an SEM[42] or STM.[45] AFM imaging of domains of this type next to vacancies on the substrate indicate topographic protrusions of ∼0.5 nm, consistent with lying-down monolayers (see the Supporting Information).

In contrast, disordered molecular domains transferred from Langmuir films at larger mma values (Figure 5) exhibit fewer geometric edges, and instead of cracks evolve rounded vacancies under the electron beam; ordered and disordered domains may coexist, as shown in Figure 5d. SEM imaging is also possible for monolayers of nondiyne molecules (see the Supporting Information, Figure S12), though evaluating order is more challenging, suggesting broader applications of this approach.

Evaluation of Monolayer Ordering via PM-IRRAS. PM-IRRAS can detect differences in monolayer ordering that impact alignment of alkyl C−H stretch dipoles.[22] Figure 6 illustrates the relationship between molecular ordering and PM-IRRAS signal strength in the C−H stretching region. For previous studies of 2D and 3D crystals of long-chain alkanes, the CH_2 asymmetric stretch (Figure 6a right inset, $\nu(CH_{2a}) \sim 2925\ cm^{-1}$) and the orthogonal CH_2 symmetric stretch ($\nu(CH_{2s}) \sim 2850\ cm^{-1}$) have been used to assess alkyl chain orientation and ordering.[22,46,47] At the bottom of each panel in Figure 6a,b, CH_{2a} dipoles are highlighted in red in a side view. In a highly ordered PCDA monolayer, the dipoles are aligned predominantly parallel to the plane of incidence (defined by the surface normal and the beam path, 70° relative to the surface normal for the experiments presented here).

The vector diagram in Figure 6a illustrates the distribution of CH_2 asymmetric stretch dipoles for the well-ordered model; vectors deviate from the surface normal by 4° ± 4°. Conversely, dipoles in disordered monolayers have a low degree of alignment in the plane of incidence. For the disordered model shown in Figure 6b, vectors deviate from the surface normal by 42° ± 29°. PM-IRRAS peak intensities can be approximated as proportional to the cosine squared of the average dipole angle relative to the p-polarized component of the IR beam. For a beam with an angle of incidence of 70° (i.e., p-polarized component 20° relative to surface normal), this suggests an approximately 2 fold difference in peak intensities

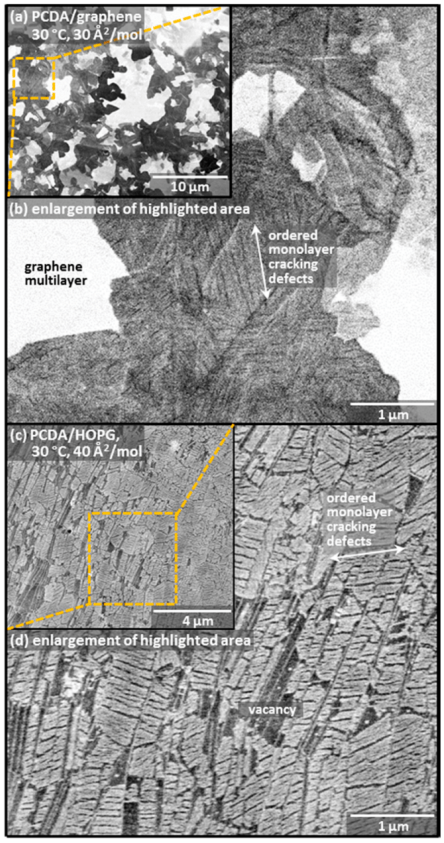

Figure 4. (a) SEM image of ordered PCDA on CVD graphene. (b) Enlargement of highlighted region of part a showing detail in original image with 30 μm edge length. (c) SEM image of PCDA on HOPG, showing ordered regions of lying-down monolayers. (d) Enlargement of highlighted region of part c.

for the highly ordered and disordered cases shown in the models. Overall, greater integrated CH_{2a} peak intensities, $I(CH_{2a})$, should be correlated with local alkyl chain order. Figure 6c,d shows representative spectra acquired from monolayers under conditions that lead to high and low degrees of molecular ordering, similar to the SEM images in Figures 4 and 5.

Figure 7 compares molecular domain structure observed in SEM images (Figure 7e−l, see the Supporting Information, Figures S8 and S9, for larger-scale original images) with $I(CH_{2a})$. Spectral trace colors match dashed lines in the isotherm that indicate the mma at transfer. Domain structure in films transferred to CVD graphene varies with transfer conditions, similar to our previous observations for transfer to HOPG.[42]

DOI: 10.1021/acs.chemmater.7b04434
Chem. Mater. 2018, 30, 2506−2514

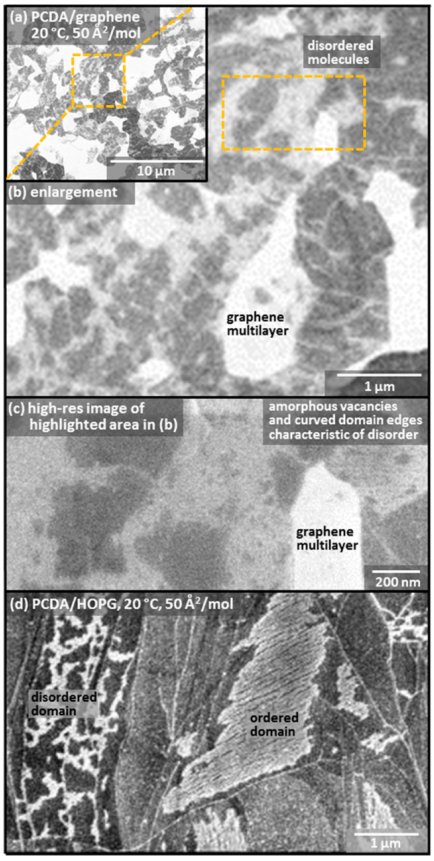

Figure 5. (a) SEM image of disordered PCDA on CVD graphene. (b) Enlargement of highlighted region in part a showing detail. (c) Higher-resolution image of region labeled "disordered molecules" in part b. (d) SEM image of PCDA on HOPG, illustrating coexistence of ordered and disordered regions.

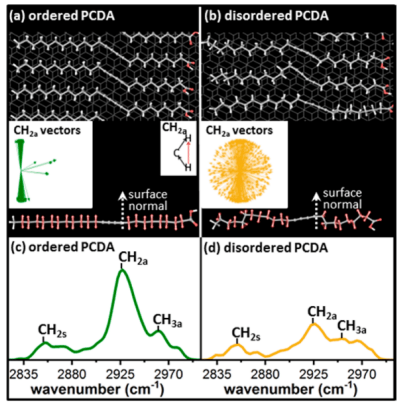

Figure 6. Molecular models for (a) ordered and (b) disordered PCDA (top), and side view of a PCDA monomer with CH_{2a} dipoles highlighted with red arrows (bottom). Insets illustrate CH_{2a} dipole vector distributions. PM-IRRAS spectra for (c) ordered and (d) disordered PCDA.

Interestingly, we find that *intermediate* values of $I(CH_{2a})$ correspond to transferred film structures consisting of lying-down lamellar domains (Figure 7i,j). Amorphous domains transferred at large mma (40–50 Å^2/molecule) exhibit low PM-IRRAS signal intensities (Figure 7c,d, orange and red traces). At 20 °C, transferred films remain poorly ordered at mma values as low as 30 Å^2/molecule, and $I(CH_{2a})$ remains low (Figure 7c, green trace).

In contrast, at 30 °C, surface pressure begins to increase prior to 30 Å^2/molecule; transferred monolayers then exhibit higher coverage and order (Figure 7j), producing intermediate values of $I(CH_{2a})$ (Figure 7d, green trace). Ordered domains also transfer from highly compressed Langmuir films (20 Å^2/molecule, Figure 7e,i). However, rodlike structures (presumably small 3D crystals of PCDA) appear in SEM images (Figure 7e) for T_{sp} = 20 °C. The presence of these structures is correlated with much larger values of $I(CH_{2a})$ (Figure 7c, blue trace) and would be undesirable for many applications. Thus, it is not feasible to screen for noncovalent monolayer ordering solely by maximizing $I(CH_{2a})$.

$I(CH_{2a})/I(CH_{3a})$ as a Metric of Monolayer Ordering. Ideally, spectral metrics should distinguish between increases in signal intensity due to increased surface coverage and increased monolayer ordering. The total intensity (I_{total}) of peaks in the C–H stretching region is a convolution of molecular coverage and interfacial order. However, CH_{2a} and CH_{2s} are orthogonal stretches; CH_{2a} aligns strongly in the plane of incidence for ordered monolayers (Figure 6a). Thus, for lying-down phases of PCDA, ordering of the zigzag alkyl backbone parallel to the substrate should increase $I(CH_{2a})$ and decrease $I(CH_{2s})$. In contrast, the CH_3 asymmetric stretch ($\nu(CH_{3a}) \sim 2960$ cm^{-1}) is less sensitive to monolayer ordering.[48]

To distinguish between surface coverage and the degree of alkyl chain ordering, we examined ratios of $I(CH_{2a})$, $I(CH_{2s})$, and $I(CH_{3a})$. I_{total} and $I(CH_{2a})/I(CH_{2s})$ (Figure 8) have been employed previously to assess coverage and degree of ordering, respectively, of standing phase monolayers and bulk crystals.[22,47] Both I_{total} (Figure 8c,d) and $I(CH_{2a})/I(CH_{2s})$ (Figure 8e,f) increase for transfers at smaller mma, consistent with increased coverage of ordered domains (SEM images, Figure 7). However, I_{total} and $I(CH_{2a})/I(CH_{2s})$ both vary strongly with coverage of 3D PCDA rods at 20 Å^2/molecule, leading to much larger mean values at 20 °C than 30 °C, even though samples prepared at 30 °C exhibit similar fractions of desirable ordered lamellar coverage. Further, lamellar coverage varies significantly for transfers at T_{sp} = 30 °C and mma >30 Å^2/molecule (discussed in more detail below); this variability is not captured by either metric.

Peak frequency shifts are also used to assess ordering in standing phase monolayers of alkanethiols;[49] however, we have not found strong correlations between peak frequencies and

DOI: 10.1021/acs.chemmater.7b04434
Chem. Mater. 2018, 30, 2506–2514

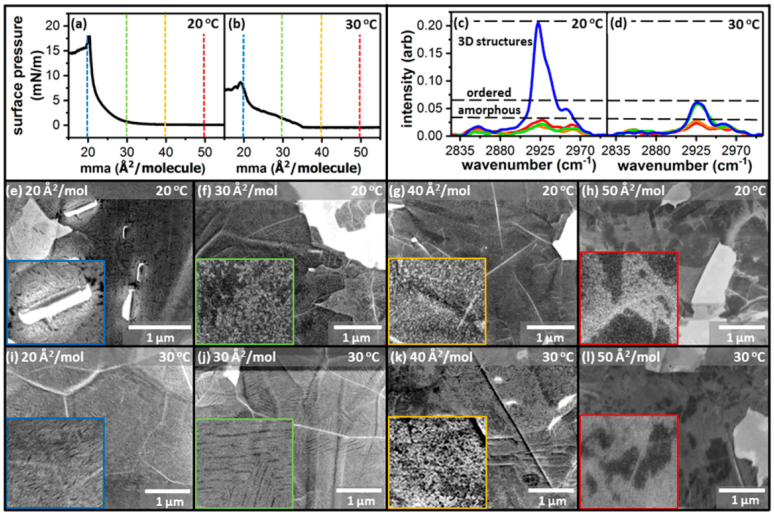

Figure 7. (a, b) Surface pressure isotherms for PCDA with subphase temperatures of (a) 20 and (b) 30 °C; dotted lines indicate mma values at which films were transferred. Representative PM-IRRAS spectra for PCDA transferred to graphene at (c) 20 and (d) 30 °C, showing increased signal intensity for samples transferred at lower values of mma. (e–l) Representative SEM images of samples transferred at the indicated temperature and mma. (See Figures S8 and S9 for larger-scale original images.)

degree of ordering observed in SEM and AFM images for the monolayers examined here (see the Supporting Information, Figure S10). Likely, this is because greater steric freedom afforded to alkyl chains in lying-down monolayers broadens peaks and results in Fermi resonances[47] in the C–H stretching region due to coupling with C–H rocking and wagging motions.

In contrast, transferred films with similar values of $I(CH_{2a})/I(CH_{3a})$ exhibit similar interfacial structure in SEM images, enabling ordering to be screened independent from surface coverage. Plots of $I(CH_{2a})/I(CH_{3a})$ vs mma (Figure 8g,h) are qualitatively similar to plots of I_{total} (Figure 8c,d).

However, $I(CH_{2a})/I(CH_{3a})$ better accounts for the large variation in signal metrics at 40 and 50 Å^2/molecule at 30 °C (due to large variations in ordered surface coverage under these conditions). Additionally, $I(CH_{2a})/I(CH_{3a})$ exhibits a large standard deviation at 25 Å^2/molecule and 20 °C, coinciding with the variable populations of PCDA rods that contribute to signal intensity for transfers under these conditions.

Interpreting $I(CH_{3a})$ as a metric of surface coverage that is approximately independent of monolayer ordering, the ratio $I(CH_{2a})/I(CH_{3a})$ measures the degree of monolayer ordering normalized against surface coverage. Therefore, it would be reasonable to expect substrates with high values of $I(CH_{2a})/I(CH_{3a})$ to exhibit a high degree of ordering. Figure 9a plots $I(CH_{2a})$ vs $I(CH_{3a})$ for a representative distribution of substrates prepared under the range of tested transfer conditions; substrates with values of $I(CH_{2a})$ near the green fit line (high ratio, 3.2 ± 0.1) are characterized by a high degree of order (SEM images in Figure 9c–e), with domains exhibiting polymerization-induced cracks visible across large areas of the substrate. In contrast, samples with values of $I(CH_{2a})$ near the gold line (low ratio, 1.6 ± 0.1) exhibit primarily amorphous domains (SEM images in Figure 9f–h). The percentage of lamellar surface coverage for PCDA on HOPG was quantified across a range of transfer parameters by SEM and also correlates well with $I(CH_{2a})/I(CH_{3a})$ (Figure S13). Thus, PM-IRRAS can be used to rapidly and nondestructively screen for order in lying-down monolayers on 2D materials.

Although the CH_{2s} peak intensity could also, in principle, serve as a metric of ordering, in practice, the symmetric stretch intensity does not appear to vary systematically with molecular ordering (Figure 9b). As described above, $I(CH_{2a})/I(CH_{3a})$ increases linearly with spectral response per molecule, $I_{total}/I(CH_{3a})$; this relationship is graphed in Figure 9b as red and blue circles, with a value of $R^2 = 0.96$ for the linear fit. In contrast, there is not an equivalent increase in $I(CH_{2s})/I(CH_{3a})$ (Figure 9b, red and blue diamonds, $R^2 = 0.04$).

Comparison of PCDA Ordering on Graphene and HOPG. PM-IRRAS can also be used to screen noncovalent molecular ordering on HOPG. Raw signal intensities are overall lower for monolayers on HOPG than for those on CVD graphene. However, the selection rules for semimetallic HOPG are similar to those of nickel, with peak asymmetry introduced by dielectric properties.[50] Figure 10 shows PM-IRRAS peak ratios (Figure 10a,b) and SEM images (Figure 10c–f) comparing molecular transfer on HOPG and CVD graphene at 30 and 50 Å^2/molecule with T_{sp} = 30 °C. HOPG and CVD graphene exhibit a nearly identical ordering/coverage relationship (Figure 10a). For both substrates, ordered films transferred at 30 Å^2/molecule have high values of $I(CH_{2a})/I(CH_{3a})$ (Figure 10b, upper oval; SEM images in Figure 10c,d); less-ordered films (Figure 10e,f; for larger versions of images, see the Supporting Information) transferred at 50 Å^2/molecule

DOI: 10.1021/acs.chemmater.7b04434
Chem. Mater. 2018, 30, 2506–2514

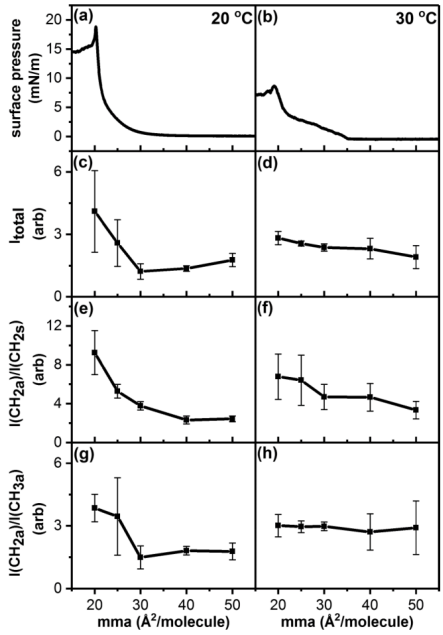

Figure 8. Surface pressure isotherms for PCDA at (a) T_{sp} = 20 °C and (b) T_{sp} = 30 °C. (c, d) Total intensity (I_{total}), (e, f) $I(CH_{2a})/I(CH_{2s})$, and (g, h) $I(CH_{2a})/I(CH_{3a})$ of the C−H stretching region for films transferred at given values of T_{sp} and mma.

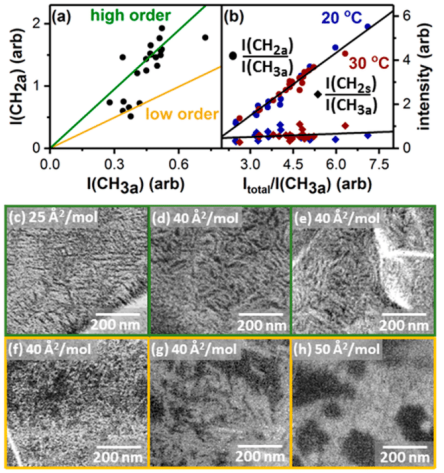

Figure 9. (a) $I(CH_{2a})$ vs $I(CH_{3a})$. (b) Peak intensity vs inverse CH_{3a} intensity fraction. Circles represent $I(CH_{2a})/I(CH_{3a})$ while diamonds represent $I(CH_{2s})/I(CH_{3a})$, with T_{sp} = 20 °C (blue) and T_{sp} = 30 °C (red). (c–e, green frames; f–h, yellow frames) Representative SEM images from samples with values of $I(CH_{2a})$ near green and yellow fit lines.

have low values (Figure 10b, lower oval). HOPG substrates typically exhibit higher values of $I(CH_{3a})$, likely due to a combination of the flatter surface resulting in greater extent of transfer during LS conversion and the asymmetric PM-IRRAS peak shapes.

■ CONCLUSIONS

We utilized a combination of PM-IRRAS spectra and SEM imaging to assess the degree of ordering in noncovalently adsorbed PCDA monolayers assembled on graphene and HOPG. Monolayers that exhibit a high degree of order in SEM images (e.g., large areas with polymerization-induced cracking) exhibit larger values of $I(CH_{2a})/I(CH_{3a})$ than less ordered monolayers. In contrast, spectral metrics commonly used to assess ordering in standing phase monolayers and bulk crystals are less straightforward to correlate with ordering in the lying-down monolayers probed here.

Broadly, PM-IRRAS provides a nondestructive means for examining the degree of local alkyl chain ordering over large areas in 2D materials noncovalently modified with lying-down phases of functional molecules. Other technologically relevant 2D materials exhibit different surface selection rules[51−53] that may ultimately enable more detailed assessment of monolayer structure. Analogous metrics can also be developed for other classes of molecules utilized for noncovalent functionalization of 2D materials by connecting PM-IRRAS spectra with imaging techniques such as SEM and AFM. For applications in which large domain sizes or specific geometries are desirable, SEM also provides a straightforward method to develop relationships between surface preparation conditions and long-range ordering.

■ EXPERIMENTAL METHODS

Materials. The 10,12-pentacosadiynoic acid (≥97.0% purity) was purchased from Sigma-Aldrich (St. Louis, MO), and used as received. Chloroform (ChromAR grade) was purchased from Macron Fine Chemicals (Center Valley, PA) and used as received. Self-assembled monolayers of diynoic acids were deposited on either 1 cm × 1 cm CVD graphene on nickel substrates (Graphene Supermarket, Calverton, NY) or highly oriented pyrolytic graphite (HOPG, SPI Supplies, West Chester, PA) substrates; HOPG was freshly cleaved immediately prior to sample deposition. All initial steps in the deposition process were carried out under UV-filtered light to prevent premature polymerization.

Langmuir−Schaefer Conversion. LS conversion was performed using a KSV-NIMA Langmuir−Blodgett trough (Biolin Scientific, Stockholm, Sweden). In a typical transfer, 12 μL of a 0.75 mg/mL solution of PCDA in chloroform was deposited on a subphase of deionized water (~18 MΩ cm). After the small amount of chloroform used for amphiphile transfer was allowed to evaporate, trough barriers were slowly moved inward to adjust the mean molecular area.

During trough equilibration and compression, the CVD graphene substrates were heated on a hot plate at ~300 °C for 10 min to drive off surface contaminants, as the surface cannot be cleaved. The hot plate temperature was subsequently lowered to 120 °C; following removal from the hot plate, substrates underwent additional cooling as they were loaded on the dipper and lowered to the subphase. Typical final substrate temperatures prior to contact with the subphase were ~30 °C. HOPG substrates were subjected to the same treatment for consistency, but were cleaved immediately prior to being loaded on the dipper.

DOI: 10.1021/acs.chemmater.7b04434
Chem. Mater. 2018, 30, 2506−2514

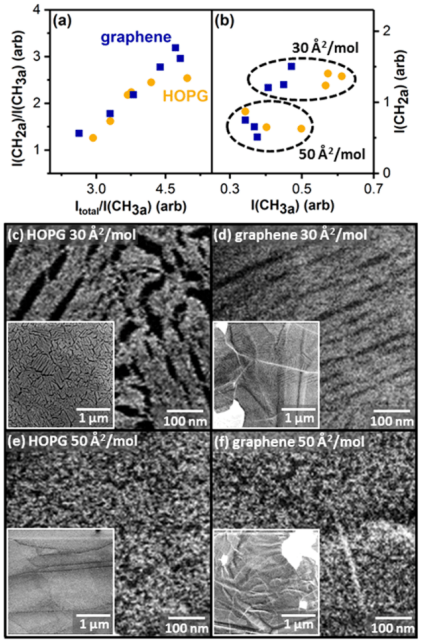

Figure 10. (a) $I(CH_{2a})/I(CH_{3a})$ vs inverse CH_{3a} intensity fraction for HOPG and graphene. (b) $I(CH_{2a})$ vs $I(CH_{3a})$ for the same substrates. (c–f) Representative SEM images of samples from part b with insets illustrating overall surface topography.

When the Langmuir film was compressed to the desired mean molecular area (e.g., 30 Å^2/molecule), the CVD graphene or HOPG substrate was slowly lowered onto the subphase with the cleaved surface facing down, nearly parallel to the liquid interface. Sample translation was performed using an automated dipper that suspends the sample on a hanging wire, to maximize stability of the substrate–subphase contact. After 4 min in contact with the liquid interface, the substrate was gently lifted out of contact with the liquid using the automated dipper. Samples prepared in this manner were immediately blown dry with N_2 and scanned in the PM-IRRAS. Three substrates were spectroscopically analyzed for each temperature/mma data point, except for values of mma that produced a large variation of monolayer order in transferred films (i.e., at 40 and 50 Å^2/molecule for 30 °C). In these cases, either six or nine substrates were analyzed.

PM-IRRAS. Spectra were acquired using a custom-built PM-IRRAS spectrophotometer. The infrared light source, interferometer, data collection, and processing were provided by a Nicolet iS50R spectrometer (Thermo, Waltham, MA). All optical components were purchased from Thorlabs (Newton, NJ) unless otherwise specified. The infrared beam was passed from the spectrometer exit port into a polycarbonate enclosure and directed through an f/8 BaF_2 lens (Infrared Optical Products, Farmingdale, NY) at a 70° incidence angle using gold mirrors with a protective coating. The beam then passed through a holographic BaF_2 linear polarizer set at an angle of 45° relative to the optical axis of a Hinds Series II ZNS50 photoelastic modulator (Hinds Instruments, Portland, OR), which modulated the beam at a 50 kHz frequency and a half wave retardation of 2500 cm^{-1}. The beam was then focused onto the sample and reflected through a second BaF_2 linear polarizer which was adjusted to minimize the polarization effects of the substrate. Finally, the light was focused through a BaF_2 lens onto a HgCdTe high D* detector (Thermo, Waltham, MA). Spectra were acquired at 8 cm^{-1} resolution and 1024 scans (CVD graphene) or 4096 scans (HOPG).

Spectral Analysis. All PM-IRRAS spectra were processed using Origin Pro software. Baseline subtraction was performed using a least-squares asymmetric smoothing fit, and peak areas were calculated using the ProFit package to solve for the individual peak areas.

SEM Imaging. All SEM images were acquired using a Nova NanoSEM instrument in immersion imaging mode with a Through-the-Lens detector. Imaging was performed with dwell times of 48 μs under a 5 kV electron beam and working distance of 3 mm, with magnifications ranging from 16 000× to 70 000×.

AFM Imaging. All AFM measurements were performed in tapping mode under ambient conditions (in air) using a Bruker (Bruker Instruments, Billerica, MA) MultiMode AFM instrument equipped with an E scanner with 0.01–0.025 Ohm cm antimony (n)-doped Si Bruker RFESP-75 tips (nominal force constant 3 N/m and radius of curvature <12 nm).

Image Analysis. Images were processed using Gwyddion[54] scanning probe microscopy data visualization and analysis software to perform median line corrections, plane flattening, scar artifact removal, and contrast adjustment.

Energy Minimization. Software packages Maestro[55] and Macromodel[56] were used, respectively, to visualize molecular structures and to perform force field minimizations. Models were minimized using the OPLS_2005 force field,[57] with normal cutoffs for van der Waals, electrostatic, and hydrogen bonding interactions. PCDA monolayers were assembled by organizing 32 molecules on top of a bilayer of graphene. The PCDA monomers were arranged into 2 columns of 16 molecules each, forming hydrogen-bonded dimers between each pair of molecules. To simulate a randomly disordered monolayer, the PCDA monolayer was subjected to molecular dynamics for 1 ns at 300 °C. All calculations were executed in the presence of explicit water molecules and with the graphene bilayer frozen. Minimizations were performed using the Polak–Ribiere conjugate gradient (PRCG) algorithm and gradient method with 50 000 runs and a convergence threshold of 0.05 kJ/(mol Å). Dynamics were run with 10 ps of pre-equilibration time and a 1.5 fs step time, using SHAKE for bonded hydrogens. The distribution of CH_{2a} dipole stretch vectors was determined by exporting the atom coordinates and calculating their angles with respect to the graphene surface normal vector.

■ ASSOCIATED CONTENT

Supporting Information

The Supporting Information is available free of charge on the ACS Publications website at DOI: 10.1021/acs.chemmater.7b04434.

SEM images of PCDA monolayers prepared by drop-casting, original SEM images, CH_{2a} peak frequencies, AFM PCDA height profiles, $I(CH_{2a})/I(CH_{2s})$ ratio data, SEM images of PCA, and $I(CH_{2a})/I(CH_{2s})$ quantification data (PDF)

■ AUTHOR INFORMATION

Corresponding Author

*E-mail: claridge@purdue.edu. Phone: 765-494-6070.

ORCID

Shelley A. Claridge: 0000-0002-8599-0589

Notes

The authors declare no competing financial interest.

■ ACKNOWLEDGMENTS

S.A.C. acknowledges support through an NSF CAREER award, NSF-CHE 1555173, a DuPont Young Professor Award, and a 3M Non-Tenured Faculty Award. S.R.R. acknowledges support

DOI: 10.1021/acs.chemmater.7b04434
Chem. Mater. 2018, 30, 2506–2514

through a W. Brooks Fortune Predoctoral Fellowship and a Frederick N. Andrews Predoctoral Fellowship.

■ REFERENCES

(1) Mann, J. A.; Dichtel, W. R. Noncovalent Functionalization of Graphene by Molecular and Polymeric Adsorbates. *J. Phys. Chem. Lett.* **2013**, *4*, 2649−2657.

(2) MacLeod, J. M.; Rosei, F. Molecular Self-Assembly on Graphene. *Small* **2014**, *10*, 1038−1049.

(3) Huang, X.; Qi, X. Y.; Boey, F.; Zhang, H. Graphene-Based Composites. *Chem. Soc. Rev.* **2012**, *41*, 666−686.

(4) Russell, S. R.; Claridge, S. A. Peptide Interfaces with Graphene: An Emerging Intersection of Analytical Chemistry, Theory, and Materials. *Anal. Bioanal. Chem.* **2016**, *408*, 2649−2658.

(5) Tahara, K.; Katayama, K.; Blunt, M. O.; Iritani, K.; De Feyter, S.; Tobe, Y. Functionalized Surface-Confined Pores: Guest Binding Directed by Lateral Noncovalent Interactions at the Solid-Liquid Interface. *ACS Nano* **2014**, *8*, 8683−8694.

(6) Li, B.; Klekachev, A. V.; Cantoro, M.; Huyghebaert, C.; Stesmans, A.; Asselberghs, I.; De Gendt, S.; De Feyter, S. Toward Tunable Doping in Graphene FETs by Molecular Self-Assembled Monolayers. *Nanoscale* **2013**, *5*, 9640−9644.

(7) Cui, D.; MacLeod, J. M.; Ebrahimi, M.; Perepichka, D. F.; Rosei, F. Solution and Air Stable Host/Guest Architectures from a Single Layer Covalent Organic Framework. *Chem. Commun.* **2015**, *51*, 16510−16513.

(8) Bang, J. J.; Rupp, K. K.; Russell, S. R.; Choong, S. W.; Claridge, S. A. Sitting Phases of Polymerizable Amphiphiles for Controlled Functionalization of Layered Materials. *J. Am. Chem. Soc.* **2016**, *138*, 4448−4457.

(9) Loh, K. P.; Tong, S. W.; Wu, J. S. Graphene and Graphene-Like Molecules: Prospects in Solar Cells. *J. Am. Chem. Soc.* **2016**, *138*, 1095−1102.

(10) Zhong, S.; Zhong, J. Q.; Mao, H. Y.; Wang, R.; Wang, Y.; Qi, D. C.; Loh, K. P.; Wee, A. T. S.; Chen, Z. K.; Chen, W. CVD Graphene as Interfacial Layer to Engineer the Organic Donor Acceptor Heterojunction Interface Properties. *ACS Appl. Mater. Interfaces* **2012**, *4*, 3134−3140.

(11) Bang, J. J.; Russell, S. R.; Rupp, K. K.; Claridge, S. A. Multimodal Scanning Probe Imaging: Nanoscale Chemical Analysis from Biology to Renewable Energy. *Anal. Methods* **2015**, *7*, 7106−7127.

(12) Choong, S. W.; Russell, S. R.; Bang, J. J.; Patterson, J. K.; Claridge, S. A. Sitting Phase Monolayers of Polymerizable Phospholipids Create Dimensional, Molecular-Scale Wetting Control for Scalable Solution Based Patterning of Layered Materials. *ACS Appl. Mater. Interfaces* **2017**, *9*, 19326−19334.

(13) Wang, S.; Ang, P. K.; Wang, Z. Q.; Tang, A. L. L.; Thong, J. T. L.; Loh, K. P. High Mobility, Printable, and Solution-Processed Graphene Electronics. *Nano Lett.* **2010**, *10*, 92−98.

(14) Castro Neto, A. H.; Guinea, F.; Peres, N. M. R.; Novoselov, K. S.; Geim, A. K. The Electronic Properties of Graphene. *Rev. Mod. Phys.* **2009**, *81*, 109−162.

(15) Zhang, Y. B.; Tan, Y. W.; Stormer, H. L.; Kim, P. Experimental Observation of the Quantum Hall Effect and Berry's Phase in Graphene. *Nature* **2005**, *438*, 201−204.

(16) Deshpande, A.; Sham, C. H.; Alaboson, J. M. P.; Mullin, J. M.; Schatz, G. C.; Hersam, M. C. Self-Assembly and Photopolymerization of Sub-2 nm One-Dimensional Organic Nanostructures on Graphene. *J. Am. Chem. Soc.* **2012**, *134*, 16759−16764.

(17) Okawa, Y.; Aono, M. Linear Chain Polymerization Initiated by a Scanning Tunneling Microscope Tip at Designated Positions. *J. Chem. Phys.* **2001**, *115*, 2317−2322.

(18) Okawa, Y.; Akai-Kasaya, M.; Kuwahara, Y.; Mandal, S. K.; Aono, M. Controlled Chain Polymerisation and Chemical Soldering for Single-Molecule Electronics. *Nanoscale* **2012**, *4*, 3013−3028.

(19) Wang, Q. H.; Hersam, M. C. Room-Temperature Molecular-Resolution Characterization of Self-Assembled Organic Monolayers on Epitaxial Graphene. *Nat. Chem.* **2009**, *1*, 206−211.

(20) Ma, H. F.; Lee, L.; Brooksby, P. A.; Brown, S. A.; Fraser, S. J.; Gordon, K. C.; Leroux, Y. R.; Hapiot, P.; Downard, A. J. Scanning Tunneling and Atomic Force Microscopy Evidence for Covalent and Noncovalent Interactions between Aryl Films and Highly Ordered Pyrolytic Graphite. *J. Phys. Chem. C* **2014**, *118*, 5820−5826.

(21) Yang, Y.; Zimmt, M. B. Shape Amphiphiles in 2-D: Assembly of 1-D Stripes and Control of Their Surface Density. *J. Phys. Chem. B* **2015**, *119*, 7740−7748.

(22) Elzein, T.; Fahs, A.; Brogly, M.; Elhiri, A.; Lepoittevin, B.; Roger, P.; Planchot, V. Adsorption of Alkanethiols on Gold Surfaces: PM-IRRAS Study of the Influence of Terminal Functionality on Alkyl Chain Orientation. *J. Adhes.* **2013**, *89*, 416−432.

(23) Duevel, R. V.; Corn, R. M. Amide and Ester Surface Attachment Reactions for Alkanethiol Monolayers at Gold Surfaces as Studied by Polarization Modulation Fourier-Transform Infrared-Spectroscopy. *Anal. Chem.* **1992**, *64*, 337−342.

(24) Barner, B. J.; Green, M. J.; Saez, E. I.; Corn, R. M. Polarization Modulation Fourier-Transform Infrared Reflectance Measurements of Thin-Films and Monolayers at Metal-Surfaces Utilizing Real-Time Sampling Electronics. *Anal. Chem.* **1991**, *63*, 55−60.

(25) Alaboson, J. M. P.; Sham, C. H.; Kewalramani, S.; Emery, J. D.; Johns, J. E.; Deshpande, A.; Chien, T. Y.; Bedzyk, M. J.; Elam, J. W.; Pellin, M. J.; Hersam, M. C. Templating Sub-10 nm Atomic Layer Deposited Oxide Nanostructures on Graphene Via One-Dimensional Organic Self-Assembled Monolayers. *Nano Lett.* **2013**, *13*, 5763−5770.

(26) Wickenburg, S.; Lu, J.; Lischner, J.; Tsai, H. Z.; Omrani, A. A.; Riss, A.; Karrasch, C.; Bradley, A.; Jung, H. S.; Khajeh, R.; Wong, D.; Watanabe, K.; Taniguchi, T.; Zettl, A.; Neto, A. H. C.; Louie, S. G.; Crommie, M. F. Tuning Charge and Correlation Effects for a Single Molecule on a Graphene Device. *Nat. Commun.* **2016**, *7*, 13553.

(27) Mali, K. S.; Pearce, N.; De Feyter, S.; Champness, N. R. Frontiers of Supramolecular Chemistry at Solid Surfaces. *Chem. Soc. Rev.* **2017**, *46*, 2520−2542.

(28) Phillipson, R.; de la Rosa, C. J. L.; Teyssandier, J.; Walke, P.; Waghray, D.; Fujita, Y.; Adisoejoso, J.; Mali, K. S.; Asselierghs, I.; Huyghebaert, C.; Uji-i, H.; De Gendt, S.; Feyter, S. Tunable Doping of Graphene by Using Physisorbed Self-Assembled Networks. *Nanoscale* **2016**, *8*, 20017−20026.

(29) Giridharagopal, R.; Kelly, K. F. Substrate-Dependent Properties of Polydiacetylene Nanowires on Graphite and MoS2. *ACS Nano* **2008**, *2*, 1571−1580.

(30) McGonigal, G. C.; Bernhardt, R. H.; Thomson, D. J. Imaging Alkane Layers at the Liquid Graphite Interface with the Scanning Tunneling Microscope. *Appl. Phys. Lett.* **1990**, *57*, 28−30.

(31) Groszek, A. J. Selective Adsorption at Graphite/Hydrocarbon Interfaces. *Proc. R. Soc. London, Ser. A* **1970**, *314*, 473−498.

(32) Rabe, J. P.; Buchholz, S. Molecular-Structure and Dynamics in Monolayers of Long-Chain Alkanes and Alkyl-Derivatives. *Makromol. Chem., Macromol. Symp.* **1991**, *50*, 261−268.

(33) Tieke, B.; Graf, H. J.; Wegner, G.; Naegele, B.; Ringsdorf, H.; Banerjie, A.; Day, D.; Lando, J. B. Polymerization of Monolayer and Multilayer Forming Diacetylenes. *Colloid Polym. Sci.* **1977**, *255*, 521−531.

(34) Lieser, G.; Tieke, B.; Wegner, G. Structure, Phase-Transitions and Polymerizability of Multilayers of Some Diacetylene Monocarboxylic Acids. *Thin Solid Films* **1980**, *68*, 77−90.

(35) Yin, S.; Wang, C.; Qiu, X.; Xu, B.; Bai, C. Theoretical Study of the Effects of Intermolecular Interactions in Self-Assembled Long-Chain Alkanes Adsorbed on Graphite Surface. *Surf. Interface Anal.* **2001**, *32*, 248−252.

(36) Okawa, Y.; Takajo, D.; Tsukamoto, S.; Hasegawa, T.; Aono, M. Atomic Force Microscopy and Theoretical Investigation of the Lifted-up Conformation of Polydiacetylene on a Graphite Substrate. *Soft Matter* **2008**, *4*, 1041−1047.

(37) Hayes, T. R.; Bang, J. J.; Davis, T. C.; Peterson, C. F.; McMillan, D. G.; Claridge, S. A. Multimicrometer Noncovalent Monolayer Domains on Layered Materials through Thermally Controlled Langmuir-Schaefer Conversion for Noncovalent 2D Functionalization. *ACS Appl. Mater. Interfaces* **2017**, *9*, 36409−36416.

DOI: 10.1021/acs.chemmater.7b04434
Chem. Mater. 2018, 30, 2506−2514

(38) Villarreal, T. A.; Russell, S. R.; Bang, J. J.; Patterson, J. K.; Claridge, S. A. Modulating Wettability of Layered Materials by Controlling Ligand Polar Headgroup Dynamics. *J. Am. Chem. Soc.* **2017**, *139*, 11973−11979.
(39) Asenov, A.; Kaya, S.; Brown, A. R. Intrinsic Parameter Fluctuations in Decananometer MOSFETs Introduced by Gate Line Edge Roughness. *IEEE Trans. Electron Devices* **2003**, *50*, 1254−1260.
(40) Pease, R. F.; Chou, S. Y. Lithography and Other Patterning Techniques for Future Electronics. *Proc. IEEE* **2008**, *96*, 248−270.
(41) Mali, K. S.; Greenwood, J.; Adisoejoso, J.; Phillipson, R.; De Feyter, S. Nanostructuring Graphene for Controlled and Reproducible Functionalization. *Nanoscale* **2015**, *7*, 1566−1585.
(42) Davis, T. C.; Bang, J. J.; Brooks, J. T.; McMillan, D. G.; Claridge, S. A. Hierarchically Patterned Noncovalent Functionalization of 2D Materials by Controlled Langmuir-Schaefer Conversion. *Langmuir* **2018**, *34*, 1353−1362.
(43) Rabolt, J. F.; Burns, F. C.; Schlotter, N. E.; Swalen, J. D. Anisotropic Orientation in Molecular Monolayers by Infrared-Spectroscopy. *J. Chem. Phys.* **1983**, *78*, 946−952.
(44) Naselli, C.; Rabolt, J. F.; Swalen, J. D. Order-Disorder Transitions in Langmuir-Blodgett Monolayers 0.1. Studies of Two-Dimensional Melting by Infrared-Spectroscopy. *J. Chem. Phys.* **1985**, *82*, 2136−2140.
(45) Takajo, D.; Okawa, Y.; Hasegawa, T.; Aono, M. Chain Polymerization of Diacetylene Compound Multilayer Films on the Topmost Surface Initiated by a Scanning Tunneling Microscope Tip. *Langmuir* **2007**, *23*, 5247−5250.
(46) Macphail, R. A.; Strauss, H. L.; Snyder, R. G.; Elliger, C. A. C-H Stretching Modes and the Structure of Normal-Alkyl Chains 0.2. Long, All-Trans Chains. *J. Phys. Chem.* **1984**, *88*, 334−341.
(47) Snyder, R. G.; Strauss, H. L.; Elliger, C. A. C-H Stretching Modes and the Structure of Normal-Alkyl Chains 0.1. Long, Disordered Chains. *J. Phys. Chem.* **1982**, *86*, 5145−5150.
(48) Pensa, E.; Vericat, C.; Grumelli, D.; Salvarezza, R. C.; Park, S. H.; Longo, G. S.; Szleifer, I.; De Leo, L. P. M. New Insight into the Electrochemical Desorption of Alkanethiol SAMs on Gold. *Phys. Chem. Chem. Phys.* **2012**, *14*, 12355−12367.
(49) Badia, A.; Cuccia, L.; Demers, L.; Morin, F.; Lennox, R. B. Structure and Dynamics in Alkanethiolate Monolayers Self-Assembled on Gold Nanoparticles: A DSC, FT-IR, and Deuterium NMR Study. *J. Am. Chem. Soc.* **1997**, *119*, 2682−2692.
(50) Leitner, T.; Kattner, J.; Hoffmann, H. Infrared Reflection Spectroscopy of Thin Films on Highly Oriented Pyrolytic Graphite. *Appl. Spectrosc.* **2003**, *57*, 1502−1509.
(51) Ramin, M. A.; Le Bourdon, G.; Heuzé, K.; Degueil, M.; Belin, C.; Buffeteau, T.; Bennetau, B.; Vellutini, L. Functionalized Hydrogen-Bonding Self-Assembled Monolayers Grafted onto SiO_2 Substrates. *Langmuir* **2012**, *28*, 17672−17680.
(52) Saccani, J.; Buffeteau, T.; Desbat, B.; Blaudez, D. Increasing Detectivity of Polarization Modulation Infrared Reflection-Absorption Spectroscopy for the Study of Ultrathin Films Deposited on Various Substrates. *Appl. Spectrosc.* **2003**, *57*, 1260−1265.
(53) Sang, L.; Mudalige, A.; Sigdel, A. K.; Giordano, A. J.; Marder, S. R.; Berry, J. J.; Pemberton, J. E. PM-IRRAS Determination of Molecular Orientation of Phosphonic Acid Self-Assembled Monolayers on Indium Zinc Oxide. *Langmuir* **2015**, *31*, 5603.
(54) Nečas, D.; Klapetek, P. Gwyddion: An Open-Source Software for SPM Data Analysis. *Cent. Eur. J. Phys.* **2012**, *10*, 181−188.
(55) *Maestro*, 10.1; Schrödinger, LLC: New York, 2015.
(56) *Macromodel*, 10.7; Schrödinger, LLC: New York, 2015.
(57) Banks, J. L.; Beard, H. S.; Cao, Y. X.; Cho, A. E.; Damm, W.; Farid, R.; Felts, A. K.; Halgren, T. A.; Mainz, D. T.; Maple, J. R.; Murphy, R.; Philipp, D. M.; Repasky, M. P.; Zhang, L. Y.; Berne, B. J.; Friesner, R. A.; Gallicchio, E.; Levy, R. M. Integrated Modeling Program, Applied Chemical Theory (Impact). *J. Comput. Chem.* **2005**, *26*, 1752−1780.

DOI: 10.1021/acs.chemmater.7b04434
Chem. Mater. 2018, 30, 2506−2514